CONTROLLING THERMAL EFFECTS ON CHEMICAL SYSTEMS

by

Raymond Patrick Welch

APPROVED BY SUPERVISORY COMMITTEE:

Jeremiah J. Gassensmith, Chair

Julia Chan

Gabriele Meloni

Walter Voit

To my family and friends who stuck with me through this journey,

and to myself, who I put on the back burner for far too long

CONTROLLING THERMAL EFFECTS ON CHEMICAL SYSTEMS

by

RAYMOND PATRICK WELCH, BS

DISSERTATION

Presented to the Faculty of

The University of Texas at Dallas

in Partial Fulfillment

of the Requirements

for the Degree of

DOCTOR OF PHILOSOPHY IN

CHEMISTRY

THE UNIVERSITY OF TEXAS AT DALLAS

August 2019

ACKNOWLEDGMENTS

I would like to thank my advisor, Dr. Jeremiah Gassensmith, for taking me into his lab despite my completely different research background. I appreciate his being patient with me learning almost everything about his research from scratch, and helping me develop my research, management, and presentation skills. His mentorship has helped me improve myself in many ways I would not have had the opportunity to improve otherwise. I would also like to thank my committee members, Dr. Julia Chan, Dr. Gabriele Meloni, and Dr. Walter Voit, for their help and advice through my qualifying exam and committee meetings to help me improve as a scientist, critical thinker, and communicator. I am thankful to have been a part of a wonderful lab group and it is these people who have kept me sane, lent support during hard times, and provided opportunities for personal and professional growth and friendship: Dr. Madushani Dharmarwardana, Dr. Shaobo Li, Dr. Zhuo Chen, Anna Schlimme, Hamilton Lee, Candace Benjamin, Michael Luzuriaga, Olivia Brohlin, Arezoo Shahrivarkevishahi, Fabian Castro, Jenica Lumata, Tahmid Faisal, and Nima Firouzi. I would also like to thank my undergraduate assistants throughout the years, Nazim Parupia, Victoria Nguyen, and Lakeisha Dent for putting up with my long-winded explanations and roundabout teaching.

Finally, I wish to thank my family and friends, for their love and support throughout this incredible journey of mine.

May 2019

CONTROLLING THERMAL EFFECTS ON CHEMICAL SYSTEMS

Raymond Patrick Welch, PhD
The University of Texas at Dallas, 2019

Supervising Professor: Jeremiah J. Gassensmith

Thermal energy is present everywhere and is a common cause of failure in many sensitive chemical, biological, and mechanical systems. Many methods of controlling thermal effects by protecting against its harmful effects or by harnessing it for conversion to another form of energy to do useful work have been developed. In particular, protection of thermally sensitive proteinaceous therapeutics such as vaccines requires protection against thermal energy in order to retain their therapeutic relevance. The current "cold chain" infrastructure in place that keeps them refrigerated throughout their journey from factory to clinic are expensive and prone to failure, costing billions of dollars annually and a large amount of wasted drugs. Herein, methods of encapsulating proteinaceous materials within the metal-organic framework ZIF-8 are developed and explored in their encapsulation ability, thermal and chemical protection ability, in vivo therapeutic effectiveness, and general protein affinity.

Another mode of controlling thermal energy is by using it to fuel crystallographic phase transitions to produce thermosalient effects. These dynamic crystals form a class of molecular solids capable of converting thermal energy into mechanical motion. Herein, metallized single crystals of decoxyphenyl N-substituted naphthalenediimide are used to take advantage of a

reversible large negative change in length upon heating past its phase transition to form a reusable thermally triggered crystal switch. These methods of controlling thermal effects show promising potential to positively affect the fields of chemistry, biology, electronics, and materials science.

TABLE OF CONTENTS

LIST OF FIGURES

LIST OF TABLES

CHAPTER 1

MODES OF THERMAL ENERGY CONTROL: PROTECTION AND HARNESSING

INTRODUCTION

Thermal energy transfer is the spontaneous flow of energy from a warmer system to a cooler system. This heat energy increases the internal energy of a system and is then either converted to other forms of energy or is dissipated as waste into the cooler surroundings. It could also be absorbed from warmer surroundings into a cooler system. This energy increase of a system, if not harnessed or used for useful work, can be detrimental to the system's components. This dissertation focuses on two modes of dealing with thermal energy: protecting a delicate protein system from it and using it to drive dynamic crystal phase transformations to do useful work.

PROTECTION OF PROTEINACEOUS SYSTEMS FROM THEMAL ENERGY

Drug delivery ultimately begins upon manufacture in a laboratory or factory. There is a significant journey between that point and administration into a patient. Proteinaceous drugs and vaccines are, by nature, less stable at elevated temperatures.[1] The bioactivity of vaccines and therapeutic biomolecules is maintained by their shape, which comes from the way the proteinaceous material is folded. As such, changes in temperature outside the stable region can lead to unfolding and subsequent reduction in bioactivity as well as loss of vaccine effectiveness.[2] Therapeutic proteins such as insulin,[3] therapeutic antibodies,[4] growth hormones,[5]

erythropoietin,[6] and virus capsids used as vaccines[7] require stabilization to survive outside the thermal window, and high-throughput screening[8] must be carried out to identify vaccine candidates. Researchers have been investigating this issue for over 90 years.[9] Polymers have been shown to be promising components in ambient temperature methods for delivering drugs from point of creation to point of administration. There are various strategies pursued by researchers to tackle protein stability using polymers. One of the reasons for temperature-based unfolding is the effect of solvent molecules in transferring thermal energy from the bulk solution to the protein peptide units, disrupting hydrogen bonding, and imparting enough energy to overcome the energy barrier keeping the protein conformation in a local minimum energy state along the energy landscape.[1-2]

Cold Chain Drug Delivery

The World Health Organization (WHO) recommends that vaccines be stored from 2–8 °C.[10] Currently, in order to keep vaccines within the stable temperature window, a "cold chain" infrastructure is required. This is a system of continuous refrigeration from manufacture to storage to transportation to the clinic to administration into the patient. This includes interim warehouse storage, intermediate hospitals or clinical centers, even the patient's home, and all the transportation steps in between. This sort of infrastructure is also used in food preservation, storage, and distribution.[11] Such a cold chain system requires a large number of refrigerated vehicles, including cars, trucks, aircraft, boats, trains, and even heat-protective packaging. This requires immense costs to set up, maintain, regulate, and administer in order to remain effective, including significant governmental input. As such, geographically remote places, developing nations, impoverished regions, areas struck by disaster, warzones, and locations lacking

government generally have a diminished capability, if any, to support such a system. Even in regions where the cold chain is already established, significant loss of vaccine occurs owing to malfunctions or breakdowns in the refrigeration systems.[12] Total cold chain costs are highly dependent on maintaining temperature in individual components; small temperature perturbations have a large impact on the overall costs.[13]

Several methods have been described recently that improve protein and vaccine stability under

Table 1.1. Thermostability in the macroscale

Category	Ref.	Biomolecule	Polymer System	Thermostability
Solvent Removal	14	LaSota vaccine	Trehalose, PVP[a]	40 °C, 21 days
	15	AdHu5[b], VSV[c]	Mannitol/Dextran, Trehalose, Eudragit®	Improved T_g
	16	Cholera vaccine	Eudragit®, Carbopol®, Alginate	25 °C, 1 year 40 °C, 6 months
Immobilization	17	G-CSF[d]	Poly(caprolactone)	60 °C, 30 minutes
	18	Goat anti-Rabbit IgG, anti-cTnI[e]	Silk fibroin	40 °C, 1 week
	19	β-Galactosidase, Alkaline Phosphatase, T4 DNA Ligase	Photodegradable Hydrogel	60 °C, 4 weeks
	20	TMV[f]	ZIF-8	Boiling water
	21	NGAL[g], CA-125	ZIF-8	60 °C, 4 weeks
Bioconjugation	22	Amelogenin	PNIPAM[h]	40 °C
	23	β-Glucosidase	PNIPAM[h]	70 °C
	24	GFP[i]	POEGMA[j]	90 °C
	25	Catalase	PAA[k]	50 °C

[a]Poly(vinylpyrrolidone); [b]Adenovirus human serotype 5; [c]Vesicular stomatitis virus; [d]Granulocyte Colony-Stimulating Factor; [e]anti-cardiac troponin I antibody; [f]Tobacco mosaic virus; [g]Neutrophil gelatinase-associated lipocalin; [h]Poly(*N*-isopropylacrylamide); [i]Green fluorescent protein; [j]Poly(oligo(ethylene glycol) methyl ether methacrylate); [k]Poly(acrylic acid)

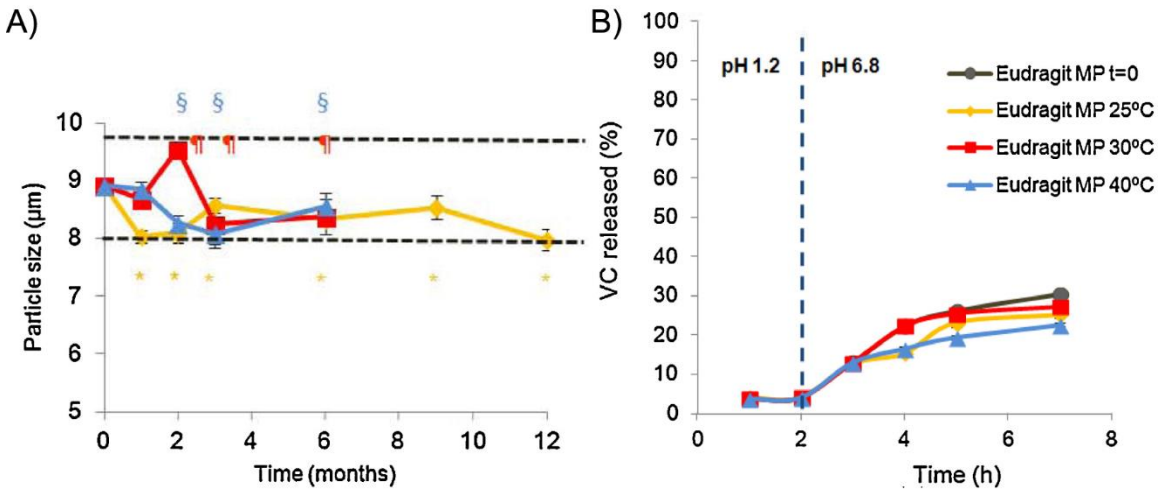

Figure 1.1. A) Particle size during storage of Eudragit® microparticles and B) gastro-resistance assay of Eudragit® microparticles. Adapted from reference [16], with permission from Elsevier.

shipping and storage temperature conditions (**Table 1.1**). These improvements allow less overhead in maintaining refrigeration—the temperatures don't have to be lowered as much—or bypassing the need for a cold chain entirely, allowing traditional ambient-temperature transportation and storage methods. While this doesn't directly address the problems of vaccine distribution in hard-to-access areas, it allows reallocation of resources away from cold chain management towards addressing those needs. We will focus on three areas: solvent removal, protein immobilization, and bioconjugation.

Solvent Removal

One method to preserve or enhance thermal stability is to remove the solvent from the formulation. This can be accomplished by lyophilization (freeze-drying), spray-drying, or vacuum foam drying to create solid products suitable for shipping without liquid handling or refrigeration. These formulations require stabilizers while drying; often, saccharides such as sucrose or trehalose[26-28] have been used to great effect. Polymers have also been used to stabilize the formulation during solvent removal. Pisal et al.[14] used poly(ethylene glycol) (PEG) and

poly(vinyl pyrrolidone) (PVP) as a stabilizer of LaSota virus while vacuum foam drying to increase the virus titer after incubation at 40 °C for 21 days. They found that PEG and PVP as stabilizers also improved the foam characteristics, allowing for a better formulation suitable for shipping. Eudragit®, an anionic copolymer of poly(methacrylic acid-*co*-methyl methacrylate), was used by LeClair et al.[15] and Pastor et al.[16] in spray-dried oral vaccine formulations to avoid degradation in the stomach. LeClair maintained thermostability of human adenovirus type 5 and vesicular stomatitis virus stabilized by saccharides and coated in gastro-resistant polymer. Pastor protected cholera vaccine for six months at 40 °C and one year at 25 °C, as determined by particle size (**Figure 1.1A**) and vaccine release (**Figure 1.1B**). While the primary focus of these two studies is preventing premature release and subsequent protein degradation in the stomach, they both also show improved thermostability and potential for cold-chain-free transport. These formulations highlight a synergy of drug delivery on macro and micro scales, as the polymer used to confer increased thermostability also allows the vaccine to survive the low pH stomach conditions, permitting oral administration and extending the vaccine's journey.

Protein Immobilization

In addition to solvent removal, immobilization is an important method of protein protection. Encapsulation in various materials has shown to be effective in creating a barrier between the protein and the external environment, providing increased stability against unfolding or solvent effects. This immobilization can be done by entangling the protein within polymer chains, crosslinking polymer chains around the protein to form a gel or holding the protein in place within rigid crystalline materials, such as metal-organic frameworks (MOFs).

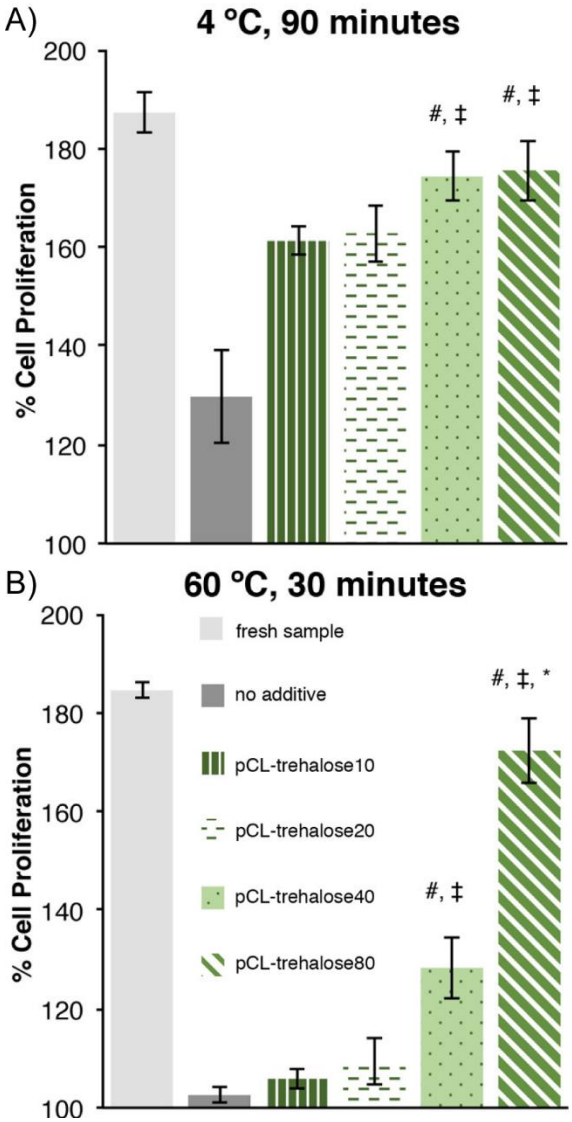

Figure 1.2. Improvement of thermal stability by immobilization in pCL with trehalose sidechains of different lengths at A) 4 °C for 90 minutes and B) 60 °C for 30 minutes. Adapted with permission from reference [17]. Copyright 2017 American Chemical Society.

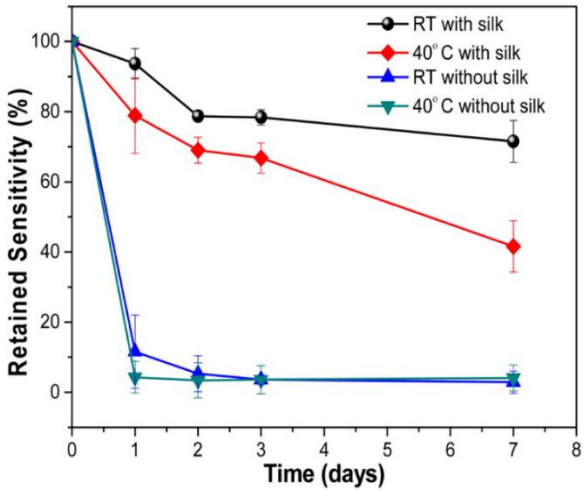

Figure 1.3. Improved thermal stability through silk film immobilization of gold nanorod plasmonic biochips conjugated with rabbit IgG. Adapted with permission from reference [18]. Copyright 2016 American Chemical Society.

Immobilization by polymer chain entanglement[29] or within hydrogels[30] allows the protein to be held in place and resist conformational changes. The polymers can be designed with functional groups along the backbone to allow post-polymerization reactions for installing side chains or cross-linking. These side chain modifications may include common stabilizers like trehalose, as used by Pelegri-O'Day et al.[17] to improve stability of granulocyte colony stimulating factor against shipping temperatures of 60 °C (**Figure 1.2**). They used degradable poly(caprolactone) (pCL) as the backbone, modified with thiol-ene chemistry to develop a library of sidechains. The use of trehalose here is no surprise, given its success as a stabilizer on its own. In addition to synthetic polymers, the immobilizing polymer could even be a protein itself. Silk fibroin has been used[31] to coat or encapsulate biologics and improve stability. Wang et al.[18] coated plasmonic biochips on gold nanorods with silk fibroin film to preserve antibody activity at 40 °C for one week (**Figure 1.3**). The thermostability of the silk is not in question because it acts as a sacrificial layer, immobilizing the antibodies with hydrogen bonds and hydrophobic interactions,

and is easily removable with a simple water rinse to restore antibody binding capability. Such reconstitution of bioactivity is an important facet of the drug delivery journey; the drugs need to be successfully administered into the body to be of use. For example, Sridhar et al. encapsulated[19] various enzymes in a photodegradable hydrogel that preserved bioactivity at 60 °C for up to four weeks. This gel keeps the protein stable during transport and reconstitution upon arrival for patient administration is performed with UV light to trigger degradation of the gel and recovery of the drugs.

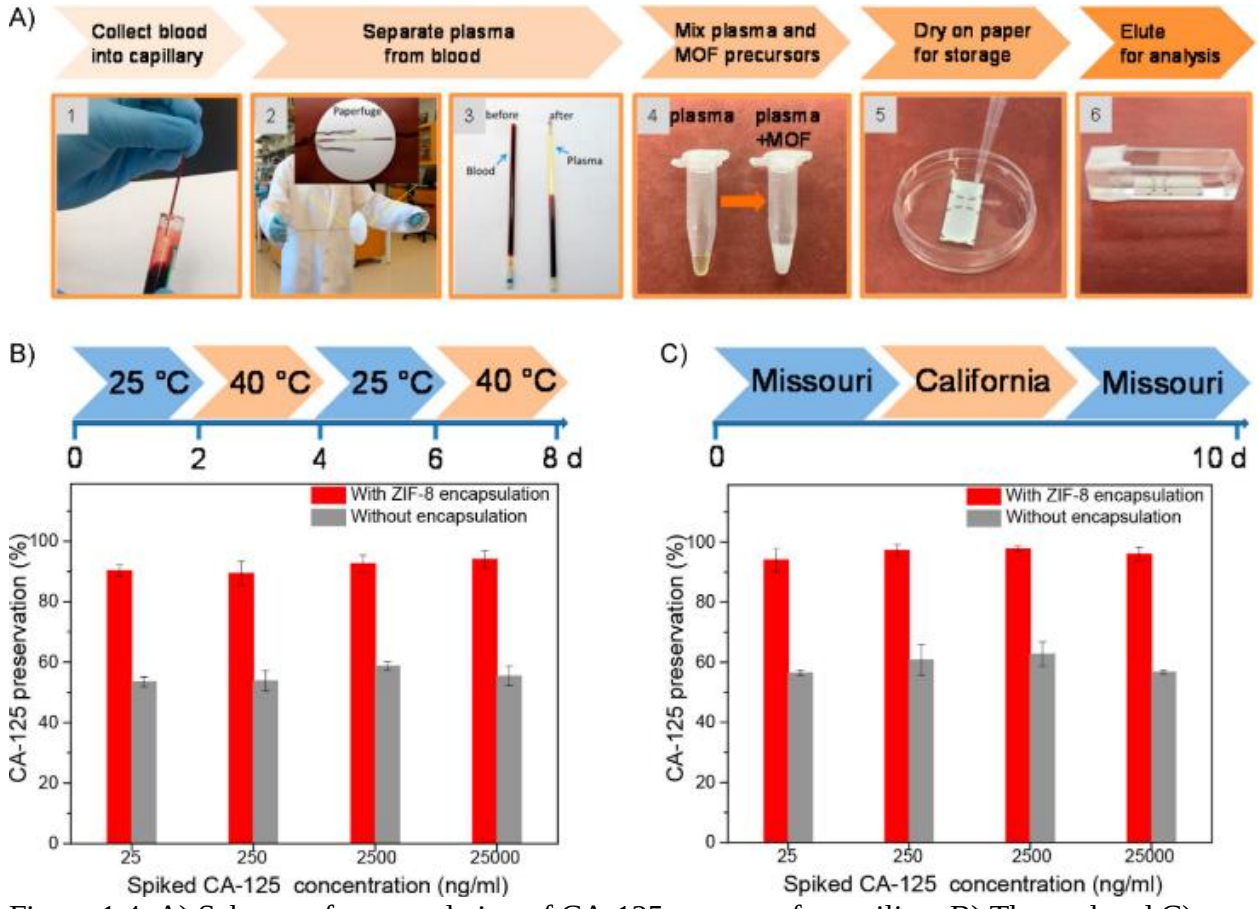

Figure 1.4. A) Scheme of encapsulation of CA-125 on paper for mailing. B) Thermal and C) shipping stability with ZIF-8 encapsulation. Reprinted with permission from reference [21]. Copyright 2018 American Chemical Society.

In contrast to flexible polymer chains, another method is to use MOFs as immobilizers to provide a rigid structural support.[32] These metal ion clusters and organic linker struts form coordination polymers that hold the protein in place and prevent changes in global conformation, thereby improving stability. These rigid crystalline porous materials have been shown to stabilize biomolecules against temperatures as high as 180 °C.[33] Here, we highlight a few studies utilizing zeolitic imidazolate framework 8 (ZIF-8), a MOF able to form in aqueous conditions. Our own group has shown[20] that ZIF-8 protection can be applied to tobacco mosaic virus (TMV) particles with a tunable shell thickness. The ZIF-8-encapsulated TMV particles show stability against harsh solvents and boiling water. We also show[34] that morphological configurations are dependent on precursor concentrations. Singamaneni's lab[21] encapsulated CA-125, a serum/plasma biomarker for ovarian cancer, in ZIF-8 crystals by drop-drying on paper with the ZIF-8 precursors (**Figure 1.4A**), tested the thermal stability (**Figure 1.4B**), and mailed it from Missouri to California and back for later extraction and analysis (**Figure 1.4C**). This study demonstrates a practical ability to ignore the cold chain and ship sensitive biological samples without refrigeration through the use of ZIF-8 encapsulation.

These immobilization methods improve thermostability by physically holding the protein higher order structure in place while not being covalently attached. This allows the proteins to be potentially released in their native state, should the drug be designed with that in mind.

Bioconjugation

Another method of protecting proteins is bioconjugation of polymers directly to the protein. Attachment of the polymer directly allows the polymer to stay with the protein longer through its journey, instead of separating upon reconstitution or administration. This may be

desired if the polymer is also intended to interact with the immune system in addition to protecting the protein through transport. This provides another synergy between different scales of the drug delivery journey. Covalent attachment also keeps the polymer with the protein even if the solution is diluted.

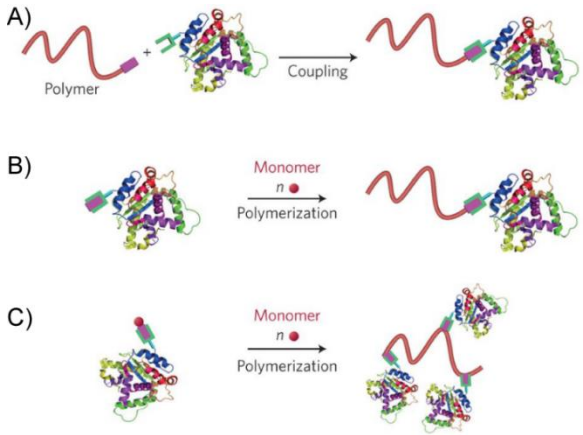

Figure 1.5. Polymerization methods of bioconjugation: A) "graft to," B) "graft from," and C) "graft through." Reproduced from. Reprinted by permission from Springer Nature: Nature Materials, reference [35]. Copyright 2014.

Polymer conjugation techniques can be generally categorized into three groups: "graft to," "graft from," and "graft through."[35] "Graft to" conjugation is where the polymerization occurs first, then the full polymer chain is attached to the protein (**Figure 1.5A**). This method allows the polymerization to occur separately in conditions harmful to the protein, but generally has lower conjugation yields, because the now larger polymer chains are more sterically hindered from conjugation sites. Also, it is more problematic to purify the conjugates because unconjugated polymer chains are closer in size to the protein. In contrast, "graft from" methods involve conjugation of small molecule initiators directly to the protein followed by *in situ* polymerization growing polymer chains outward from the protein (**Figure 1.5B**). This method allows for higher density of the smaller initiator molecules on the protein, leading to higher polymer conjugation

yields. Purification is also easier, as free monomers and other small molecules present are easily removed via dialysis or size exclusion media. There is also another method, "graft through," that involves copolymerization of biomacromolecules that act as monomers themselves with polymerization that cross-links multiple proteins (**Figure 1.5C**). Controlled radical polymerizations such as atom transfer radical polymerization (ATRP) and reversible addition-fragmentation chain transfer (RAFT) are frequently used in bioconjugations to control chain growth and introduce new functional groups.[36] Examples of ring-opening metathesis polymerization (ROMP) have also been appearing in the literature for these applications.[37]

The choice of polymer and method of attachment depend on the desired property it will add to the protein. For example, poly(N-isopropylacrylamide) (PNIPAM) is a thermoresponsive polymer that drastically changes solubility in water as a function of temperature, allowing for a stimuli-responsive bioconjugate. PNIPAM was used by Jiang et al.[22] grafted from amelognin with ATRP, enhancing the thermal self-assembly properties of the protein to create potential drug carrier nanospheres. PNIPAM was also used by Mukherjee et al.,[23] grafting from β-glucosidase using RAFT polymerization, retaining up to 70% of its enzymatic activity at 70 °C compared to native enzyme. In both of these studies, the hydrodynamic diameter of the bioconjugates drastically increased with temperatures greater than the PNIPAM lower critical solution temperature of 33 °C, highlighting the thermoresponsive nature the PNIPAM polymer confers to the conjugates.

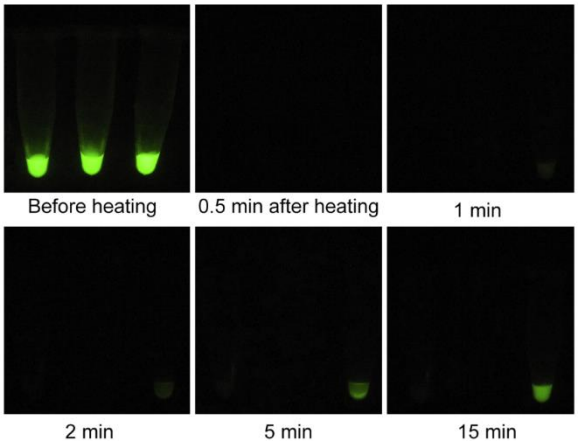

Figure 1.6. A) Visual recovery of GFP fluorescence after denaturing at 90 °C of *l*-GFP (left tube), *l*-GFP-POEGMA (middle tube), and *c*-GFP-POEGMA (right tube) and B) fluorescence recovery percent. Adapted from reference [24], with permission from Elsevier.

The polymer itself does not have to be thermoresponsive, however. Poly(oligo(ethylene glycol) methyl ether methacrylate) (POEGMA) is used to enhance circulation and retention times in the body, and poly(acrylic acid) (PAA) is used as a polyelectrolyte, but both can still confer thermostability to the protein. For example, Hu et al.[24] used circularized green fluorescent protein (GFP), which was linked via the C- and N-termini, and grafted POEGMA from it using ATRP. After thermal denaturation, the conjugated GFP recovered its fluorescence after just a few minutes compared to no recovery for linear GFP or linear GFP-POEGMA (**Figure 1.6**). The bioconjugations hold the protein structure together enough that refolding of the fluorophore is possible. The POEGMA also enhanced tumor retention, a synergy between the macro and nano scales. Riccardi et al.[25] used EDC coupling to graft PAA to catalase. The bioconjugates showed retention of enzymatic activity and thermal stability up to 80 minutes at 50 °C, in addition to lowered rates of trypsin and chymotrypsin digestion and increased activity rate in the presence of inhibitors compared to native enzyme. It is worth noting that often a systematic approach is

required to test various formulations to see which polymers enhance and which polymers hinder the desired effects.[38-40]

Looking Ahead

All of these methods can lead to enhanced thermal stability of proteins that can be used to protect potential drugs and carriers throughout the long journey from factory to clinic. As cold-chain bypass methods have begun to proliferate, the Controlled Temperature Chain Working Group of the WHO recently expanded[41] their guidelines for temperature storage for certain vaccines stable up to 40 °C. Increased vaccine, protein, and biomolecule stability at ambient or above ambient temperatures can drastically reduce costs and greatly improve public health. These reduced costs will provide a large incentive to adopt these techniques and secure government and private sector support. There is room for further improvements, however. More research is required regarding reconstitution of vaccine solutions for delivery after formulation for cold-chain free transport. Some of the researchers highlighted here have begun to do so, but most have focused primarily on maintaining stability through transport and storage, an important hurdle to overcome first. As improvements in stability continue, development could be done furthering our fundamental understanding of general protein stabilization methods that could be applicable to a broad range of proteins, instead of protein- or vaccine-specific formulations. Such development would allow more general logistic protocols to be adopted by administrating agencies, further lowering costs.

HARNESSING THERMAL ENERGY FOR CRYSTAL SYSTEMS

Smart materials are materials that show properties such as adaptivity to their environment, dynamic shifting between material states, and self -healing behavior.[42] Many of

these properties are achievable with soft materials such as polymers,[43] gels,[44] and liquid crystals.[45] Development of solid crystalline and single crystalline smart materials has lagged behind their soft material cousins. There are a large number of stimuli that smart materials respond to such as heat,[46] light,[47-48] pH,[49] mechanical stress,[50] and magnetic fields.[51] Responses to these stimuli vary and can include changes in color,[52] structure,[53] opacity,[45] thermal conductivity,[54] and conductance.[55] Thermal energy in particular is an attractive stimuli because it is present everywhere—a lack of thermal energy indicated by 0 K is literally impossible to achieve—and is frequently released as waste energy from other systems. Thermoresponsive materials are a rapidly developing research area and many systems have been developed to take advantage of thermally-induced responses such as color change (thermochromism),[56] mechanical output (thermosalience),[57] and electronic state (thermoelectric).[58]

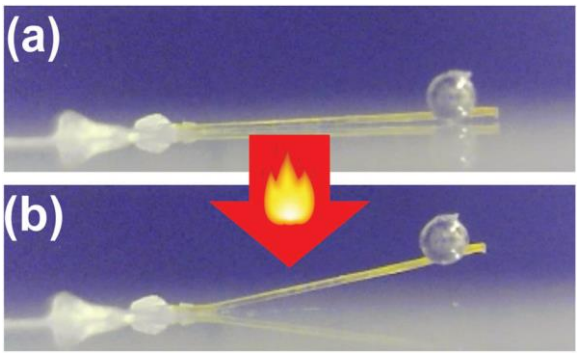

Figure 1.7. Thermo-mechanical work of a BNDI cantilever. (a) Before the phase transition. (b) After the phase transition. The crystal was heated on a glass slide on the heating stage of a polarized optical microscope. The mass of the crystal and a 0.5 mm diameter tungsten carbide ball is 0.0100 mg and 0.8320 mg, respectively. Reprinted from reference [46] with permission from The Royal Society of Chemistry.

One promising area of interest is in thermal actuators, materials that change shape or dimension based on temperature. Actuators are an integral component of any mechanical system, as they are the force producers that produce physical work from other forms of energy. In order for a thermally actuating material to be practical, its actuation properties need to be rapid,

reversible, and fatigueless.[59] Soft polymer, gel, and liquid crystal materials have been made with reversible[60] and self-healing[61] actuation, but tend to lack the speed and mechanical strength required for practical applications. Solid crystals have been brittle and disintegrate easily with repeated actuation (if the actuation is even a reversible process) but tend to have greater mechanical strength and faster actuation speeds than the soft materials do.

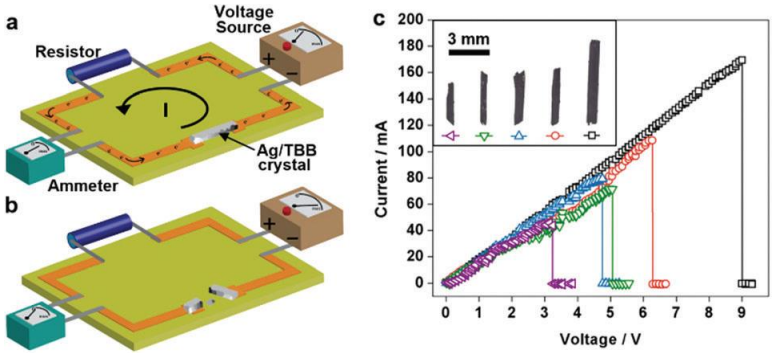

Figure 1.8. (a and b) Schematic of the circuit used for electrical characterization of the Ag/TBB crystal. The crystal conducts electricity (a) to the point where the resistive heating of the metal induces the TS effect causing the crystal to detach from the circuit (b). (c) I–V characteristics of five Ag/TBB crystals with varying lengths. The inset shows optical micrographs of the crystals used to record the I–V curves. Reprinted from reference [62] with permission from The Royal Society of Chemistry.

Thermosalient crystals are a class of solid crystalline materials that exhibit jumping, splitting, cracking, and bending from externally applied stimuli such as light or heat. Thermosalience was first reported in 1983 by Etter and Siedle,[63] and has since been studied by a few groups, namely Naumov. These thermosalient crystals have found use as actuators[46] and fuses[62] (**Figure 1.7** and **Figure 1.8**). A majority of the crystal systems studied show irreversible thermosalience that accompany phase transitions. These systems typically actuate by a buildup of mechanical stress within the crystal lattice that is released with a phase transition that induces molecular rearrangement within the crystal lattice. This release of energy often is terminal to the integrity of the bulk crystal. Reversible thermosalience is a desirable material property in an

actuator. Such actuation needs to be repeatable in the same mechanical dimensions over a number of cycles without significant degradation of the crystal (**Figure 1.9**). There have been a few such crystal systems studied,[64-71] but none of them have been adapted to a practical use. In Chapter 4, I present work toward a reversibly thermosalient system repeatable over 200 cycles with no loss of dimension change.

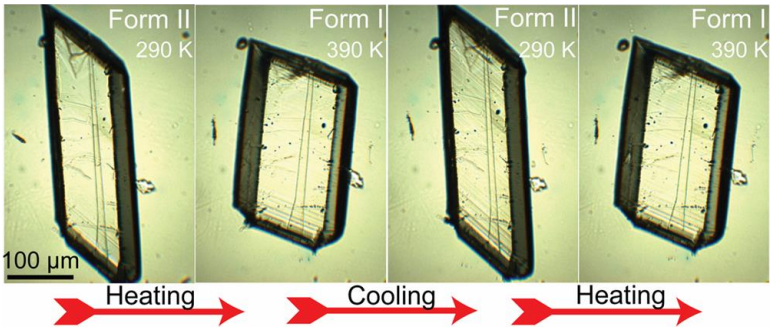

Figure 1.9. A single crystal of form II terephthalic acid, consecutively taken twice over the phase transition to form I. The crystal does not show any visible deterioration. Reprinted with permission from reference [53]. Copyright 2016 American Chemical Society.

CONCLUSIONS

As technology and materials design become more complex with increasing development and research, finer, more deliberate control over the fundamental forces that act upon smart material systems is required. Thermal energy in particular can have significant detrimental effects if not controlled for when designing material systems. These thermal effects can be mitigated against or harnessed for conversion to other energy forms or useful work. Delicate biological systems dependent on relatively narrow thermal windows to properly function are particularly susceptible to uncontrolled thermal fluctuations and must be designed with these controls in mind to extend their usefulness to clinical and widespread adoption. Since a large amount of waste energy is released as heat, this source of thermal energy can be tapped and

converted to more useable forms, improving efficiency of dynamic systems and increasing work output, reducing the overall amount of resources needed to operate the system at a given level.

In order to deliver drugs and vaccines from factory to clinic an extensive and expensive cold chain is in place to preserve the integrity of the drugs. Failures at any point in the cold chain can result in destruction of the vaccines. By bypassing the need for a cold chain, the cost and availability of vaccines can be improved. Polymers have been utilized by many research groups to devise strategies to increase the temperature stability of vaccines and proteinaceous drugs. Three prominent methods of stabilization involving polymers have emerged—solvent removal, protein immobilization, and bioconjugation. These methods work to protect the vaccines from the environment and ultimately preserve the structure and function of the proteinaceous drugs. These methods have proven successful under laboratory conditions in preserving vaccines during transportation and storage at elevated temperatures. A next step for researchers in this field is to study the recovery of the drugs at the clinic.

Development of smart materials has led to advances in soft materials such as polymers, gels, and liquid crystals, but less focus has been put on solid crystalline stimuli-responsive materials. Dynamic thermally responsive crystals have been investigated for their potential uses as actuators and fuses. While a lot of attention has been placed on thermosalient crystals, not a lot of practical applications have been found for them as of yet, as this is a relatively new and small field.

Controlling thermal effects on chemical systems is an important requirement to develop smart materials capable of improving the quality of life either directly through their applications and everyday interactions, or indirectly by allowing reallocation of existing resources to other

areas that need them. This dissertation provides insight and work towards a deeper understanding and practical application of both mitigation and harnessing of thermal energy.

CHAPTER 2

TEMPLATE DIRECTED SYNTHESIS OF POROUS AND PROTECTIVE CORE-SHELL BIONANOPARTICLES[1]

Authors – Shaobo Li, Madushani Dharmarwardana, Raymond P. Welch, Yixin Ren, Christina M. Thompson, Ronald A. Smaldone, Jeremiah J. Gassensmith*

The Department of Chemistry and Biochemistry, BSB13.102

The University of Texas at Dallas

800 West Campbell Road

Richardson, Texas 75080-3021

[1]Adapted with permission from Li, S.; Dharmarwardana, M.; Welch, R. P.; Ren, Y.; Thompson, C. M.; Smaldone, R. A.; Gassensmith, J. J., Template-Directed Synthesis of Porous and Protective Core–Shell Bionanoparticles. *Angew. Chem. Int. Ed.* **2016,** *55* (36), 10691-10696.

INTRODUCTION

Metal organic frameworks (MOFs) represent a family of microporous crystalline materials with high specific surface areas and extended porosity and have attained a level of preeminence owing to their synthetic tunability. A MOF is constructed by coordinating rigid organic "struts" to a metal ion or cluster "node" to form a crystalline material with defined pore structure, pore size, and chemical composition.[72-73] This seemingly infinite combination of metal nodes and organic struts has enabled highly tunable design strategies for specific needs[74-78] like gas storage,[79-81] sensing,[82-83] catalysis,[84-87] energy,[88-90] and in bio-medical applications.[91-93] An issue arising in many of these applications, however, has been difficulty in controlling the crystallite morphology, which typically yields bulk MOF powders with relatively large crystal size, random shape, and poor monodispersity. There is an articulated[94] interest in controlling the morphology of MOF crystallites owing to the need for nanometer scale uniformity in biomedical and optoelectronics applications. The synthetic strategies so far employed to regulate the size and morphology of MOF crystals have generally been achieved by addition of metal-binding reagents such as ligands, surfactants, or polymers with chelating functional moieties.[95-99] Although these strategies afford regulation of size, the as-obtained MOF particles are typically several hundred nanometers in size. More recently, MOF core-shell nanoparticles in the 100 nm range with good monodispersity have emerged,[83, 100-105] though control over shape is not always high, resulting in irregular spheres or cubes.

Virus nanoparticles offer a level of control unavailable in synthetic systems as the surface chemistry can be altered by either chemical or genetic manipulation.[106-110] We selected tobacco mosaic virus (TMV), a tubular viral particle that contains 2,130 identical coat proteins self-

Scheme 2.1. Synthesis and formation of TMV@ZIF-8 rod-shaped nanocomposites.

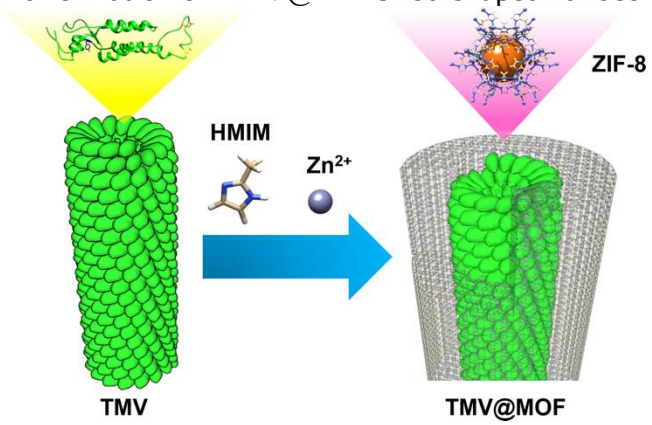

assembled around a single strand of RNA. Being 300 nm long and only 18 nm wide, the anisotropy of the virus has made it an attractive target for applications in photonics,[111] light harvesting solar arrays,[112-113] and MRI contrast agents.[114-115] TMV is also attractive as it can be isolated in gram quantities from a kilogram of tobacco leaves. Each coat protein possesses solvent-accessible amino acid residues—tyrosine on the exterior and glutamates on the interior—and these anionic residues have proven that they are available for chemical conjugation.[116] Furthermore, the robustness of TMV has allowed it to play a versatile role as a bio-template for fabrication of organic or inorganic materials[117-122] and we reasoned that these qualities would make it useful in the production of core-shell bionanoparticle (CSBN) MOF frameworks with tightly regulated shell thickness, width, and length. To obtain aqueous solution-stable CSBNs using MOFs, we turned to hydrolytically stable ZIF-8,[123] which is formed from the coordination of methyl imidazole ligands (HMIM) and Zn, and has recently been shown to nucleate and grow on enzymes (naked[33, 124-127] or polymer-coated[128-129]) in aqueous solution. Unlike enzymes, viruses are comparatively massive and are formed from highly symmetric quaternary structure; thus, we hypothesized they would give rise to regular nanoscopic shapes (**Scheme 2.1**).

In this communication we show that, using TMV as a template, the as–fabricated TMV@ZIF-8 retained the highly anisotropic rod shape of the parent virus. We were able to tune the thickness of the MOF shell by modifying the synthetic conditions. The as-obtained TMV@ZIF-8 composite demonstrates good stability in organic solvents and at high temperature. The surface exposed tyrosine groups of the TMV are still reactive while inside the MOF shell and coupling reactions performed through the MOF do not undermine the integrity of rod–shaped hybrids. Most incredibly, even after soaking the TMV@ZIF-8 in pure methanol overnight, we were able to remove the ZIF-8 shell and show the virus itself could be reclaimed without damage under these highly denaturing conditions.

RESULTS AND DISCUSSION

For our initial experiments, a desalted virus solution was first mixed with an aqueous solution of HMIM. Upon addition of an aliquot of $Zn(OAc)_2$ the reaction mixture immediately became turbid followed by flocculate formation. After sitting on the bench for 16 hours, the centrifuged solid was washed with ultrapure water twice to obtain an off-white suspension in water. We were initially pleased to find the anticipated rod structures by SEM but frustrated to discover that the rods were very unstable—when removed from the mother liquor solution containing Zn and HMIM and placed in deionized (DI) water they collapsed into flaky cubes overnight (**Figure 2.1b**). From powder X-ray diffraction (PXRD) analysis of the as-synthesized rods, we observed that the shells contained the expected ZIF-8 but also reflections corresponding to a significant amount of crystalline $Zn(OAc)_2$ (**Figure 2.2**). This led us to conduct an investigation into the optimization of our synthetic conditions to reduce unwanted $Zn(OAc)_2$ growth and improve the stability of our rod composites. As a result of this investigation, we not

only found that we could greatly affect the physical stability of the composites but also the shell thickness. A key observation was that when the HMIM:Zn molar ratio was low, the TMV@ZIF-8 core-shell composites had thinner shells and, conversely, at higher HMIM:Zn ratios, the shells thickened.

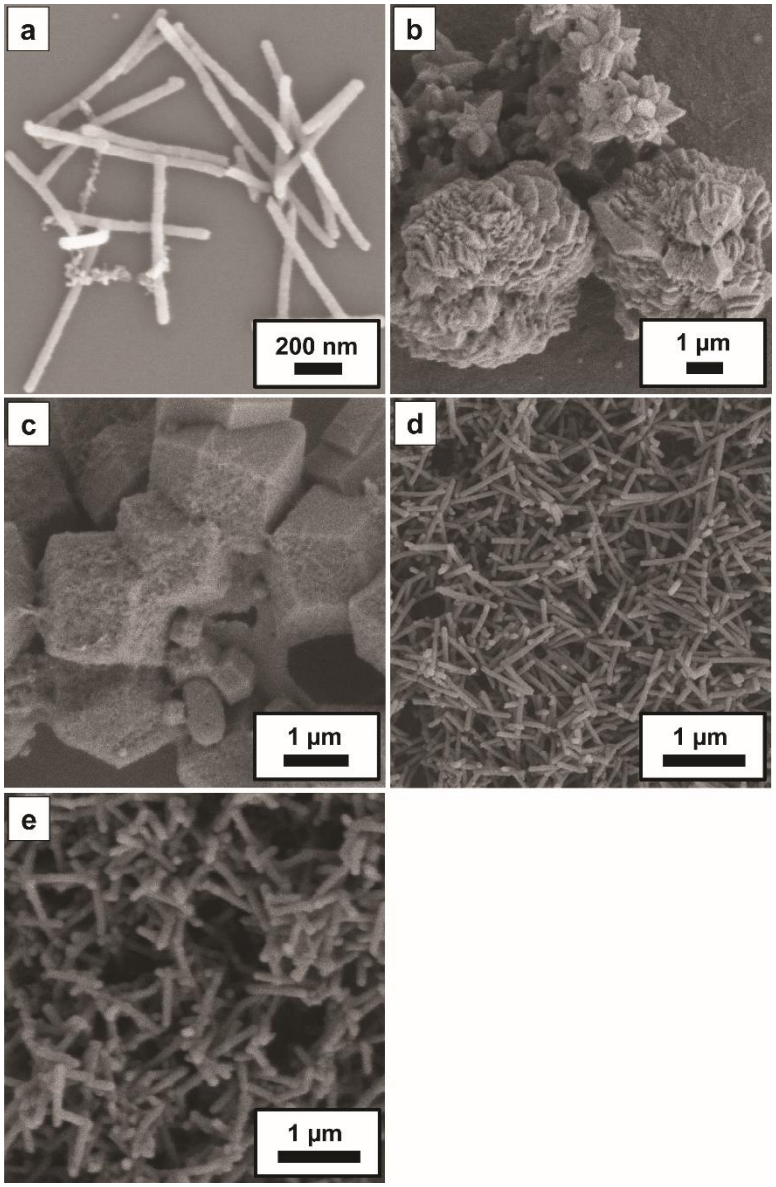

Figure 2.1. SEM micrographs of the first and unstable products we made. Shown are the (a) as-prepared TZ-P1 rod composite; (b) TZ-P1 after soaking in 18.2 MΩ DI H2O for 16 h; (c) TZ-P1 after soaking in pure methanol for 16 h; These unstable materials are compared to (d) TZ-thin and (e) TZ-thick after soaking in 18.2 MΩ DI H_2O for 16 h.

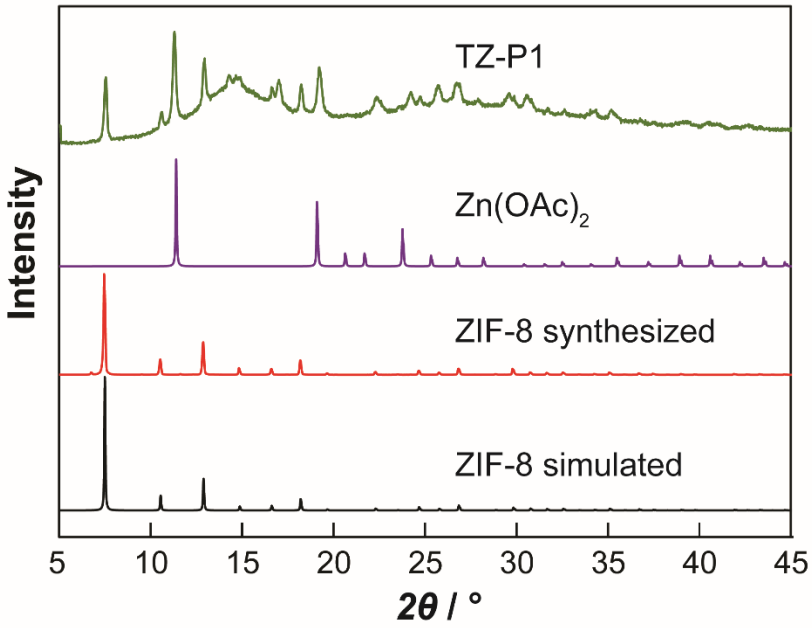

Figure 2.2. PXRD pattern of simulated ZIF-8, as-synthesized ZIF-8, zinc acetate and unstable prototype TZ-P1. From these data it appears that the initial TZ-P1 contained crystalline $Zn(OAc)_2$, making it unstable in solutions that did not contain the metal precursor salt.

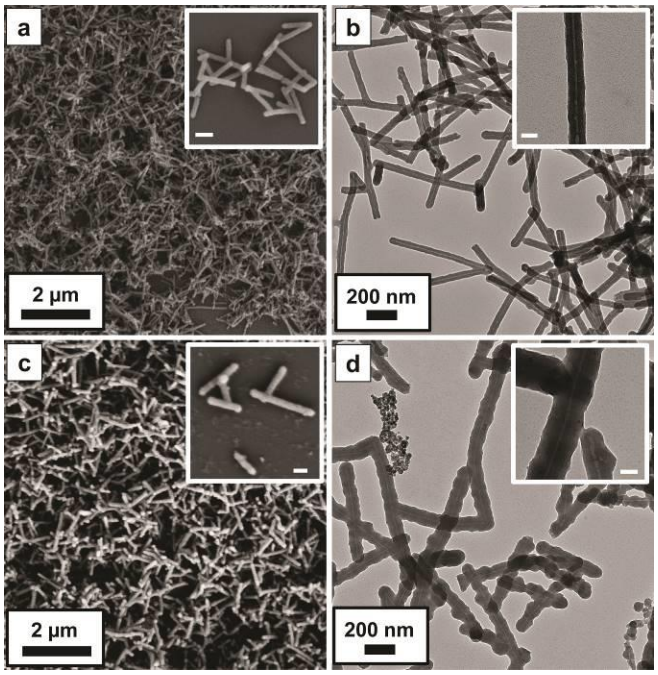

Figure 2.3. a) SEM and b) TEM of as-synthesized TZ-thin. c) SEM and d) TEM of as-synthesized TZ-thick. Inset scale bar: a), c) 200 nm; b), d) 50 nm.

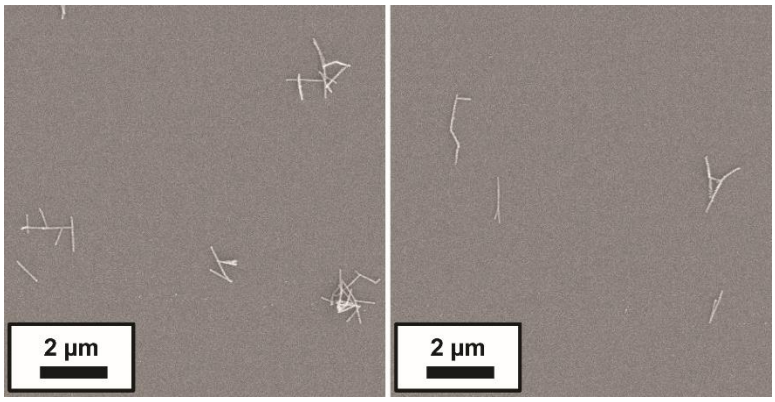

Figure 2.4. SEM micrographs of as-prepared TZ-thin composites drop cast from a low concentration suspension onto a Si wafer. This shows that at low concentration, the TMV@ZIF-8 are more discrete structures and not large aggregates.

Two representative products of this investigation are presented in **Figure 2.3**, denoted as TZ-thin (micrographs shown in **Figure 2.3a and 2.3b**) and TZ-thick (**Figure 2.3c and 2.3d**). Synthetically, these two composites are differentiated by the HMIM:Zn molar ratio used in their preparation. Specifically, the TZ-thin composite was prepared from a 20:1 ratio and the thicker wall of TZ-thick was obtained when that ratio was increased to 40:1. SEM analysis shows that both composites form regular and homogenous rods with very tightly controlled thickness. TZ-thin, for instance, is 70 nm in diameter and TZ-thick is 100 nm. We found we could control the surface coating of the TMV@ZIF-8 as well by changing the concentration used in drop casting. The dense forest shown in the SEM micrographs are a result of drop casting at high concentrations. We found we could isolate more discrete rods, even single rods, at lower concentrations (see **Figure 2.4** and **Figure 2.3** high magnification inserts). TEM shows the viral interior, which arises from the low-contrast TMV rod residing within the shell (**Figure 2.3b and 2.3d**). This provides direct evidence of successful ZIF-8 encapsulation of the tubular virus particle. We also observed rods much longer than 300 nm by SEM and TEM. This arises from TMV's propensity to align head-to-tail.[117, 120] This phenomenon is illustrated in the insert of

Figure 2.3d, which shows clearly one of these supramolecular junctions where the virus particles line up in a head-to-tail fashion.

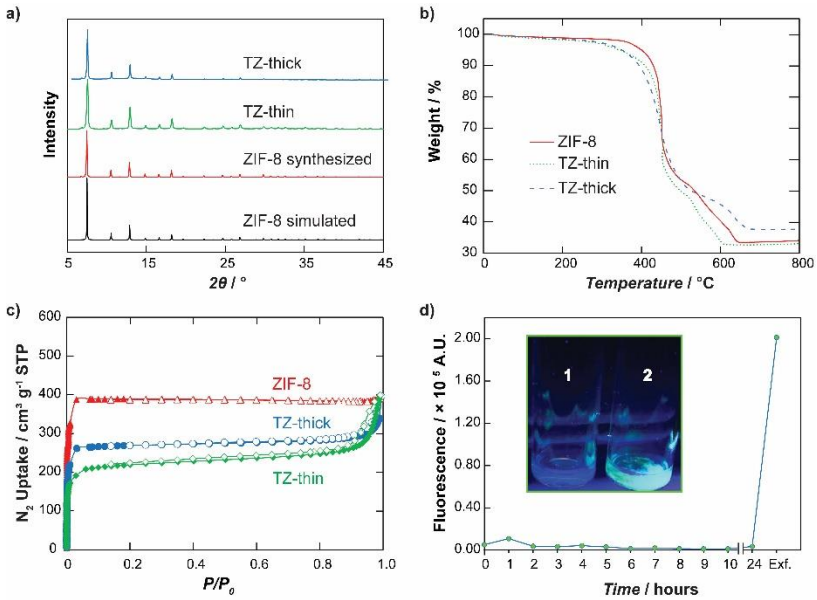

Figure 2.5. a) PXRD of simulated ZIF-8, synthesized ZIF-8, TZ-thin and TZ-thick. b) TGA curves of ZIF-8, TZ-thin and TZ-thick obtained in air atmosphere. c) N_2 sorption isotherm of ZIF-8, TZ-thin and TZ-thick. The calculated BET surface area of ZIF-8, TZ-thick and TZ-thin is 1537, 1053 and 847 m^2/g, respectively. d) Fluorescence measurement of solution after centrifugation at each time point and after exfoliation of ZIF-8 (Exf.); inset: 1) growth solution and 2) fTMV@ZIF-8 under UV light.

Crystallinity was confirmed by PXRD analysis showing reflections in excellent agreement with the simulated ZIF-8 pattern (**Figure 2.5a**). Thermogravimetric analysis (**Figure 2.5b**) under air atmosphere shows a two-stage weight loss in both TZ-thin and TZ-thick, starting from 250 to 350 °C, which we attributed to the decomposition of the proteins, then a sharp decrease at 450 °C consistent with decomposition of pure ZIF-8. Permanent porosity of the resulting shell was confirmed by nitrogen absorption analysis at 77 K (**Figure 2.5c**). The final BET surface area values of the separate composites show an expected decrease in available surface area associated with the incorporation of the virus. Solution stability and synthetic yield

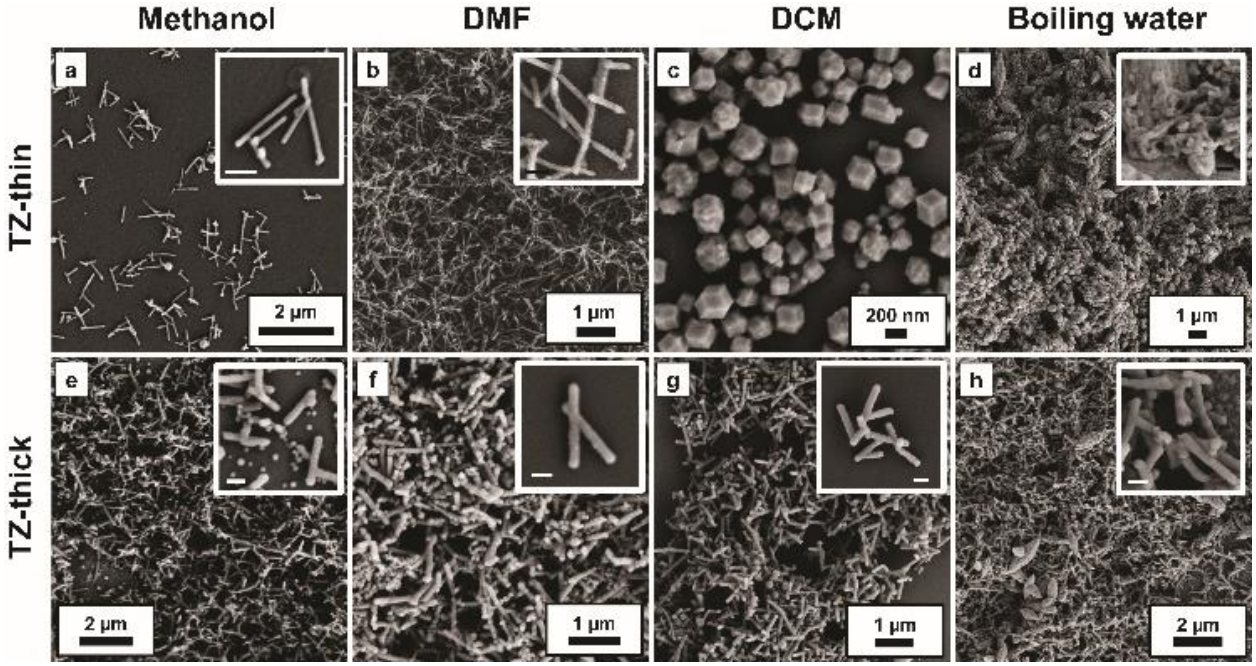

Figure 2.6. SEM of TZ-thin after soaking in a) methanol, b) DMF, c) DCM for 16 h, and in d) boiling water for 20 min. TZ-thick after soaking in e) methanol, f) DMF, g) DCM for 16 h, and in h) boiling water for 20 min. Inset scale bar: a) 300 nm; b, d, e, f, g and h) 200 nm.

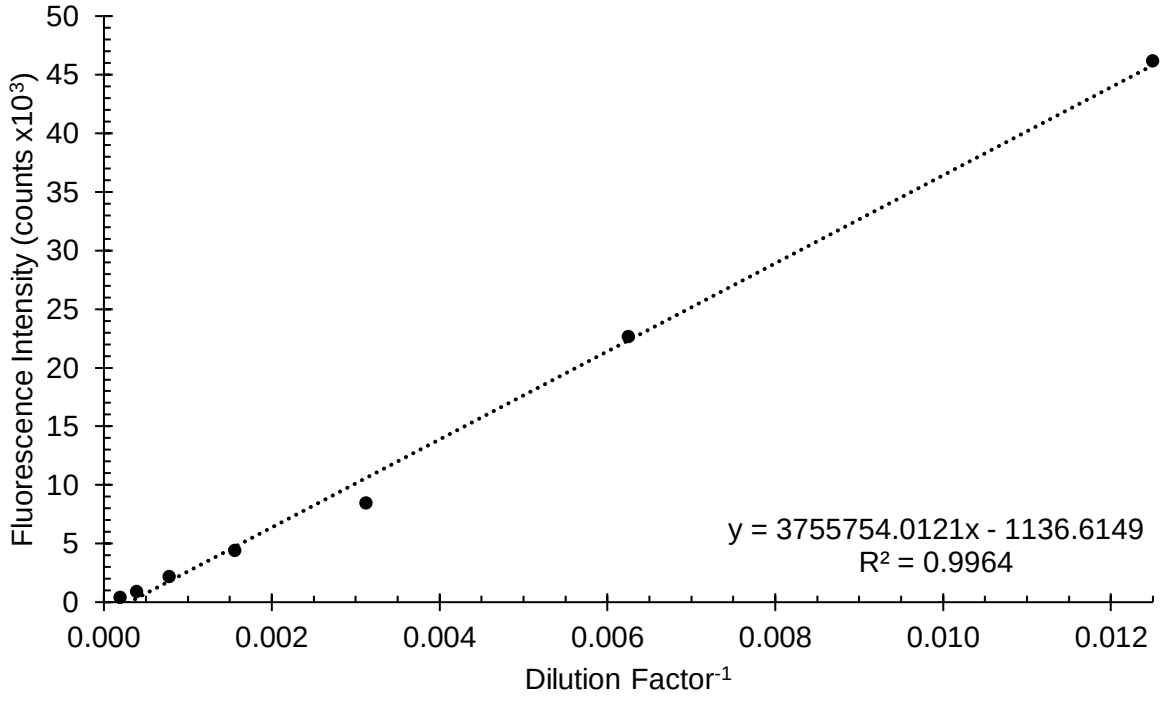

Figure 2.7. Calibration curve for fTMV. The dilutions of 1×, 10×, 20×, and 40× were not included on the line because the detector was saturated at these points.

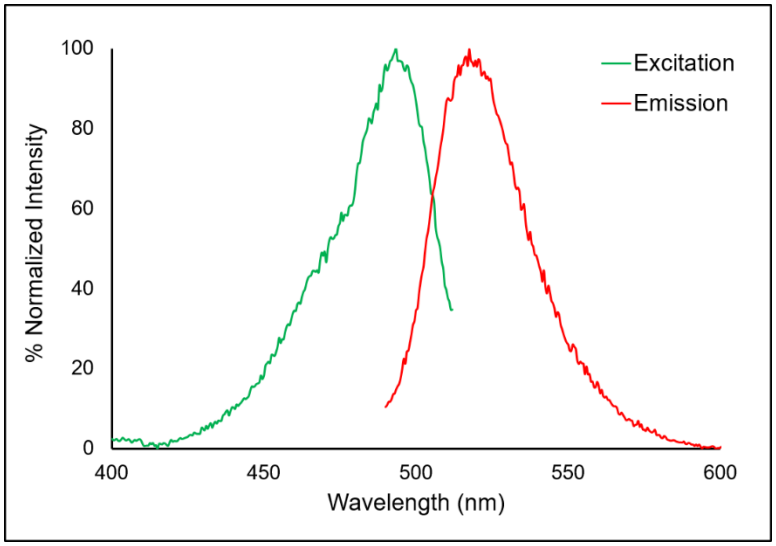

Figure 2.8. Excitation/Emission spectra of fTMV

were analyzed by functionalizing the inner channel of the TMV with a fluorescent FITC tag (fTMV, see **Figure 2.7 and Figure 2.8**) and then growing the ZIF-8 shell around the resulting virus. Following growth and centrifugation of the composite, we found nearly undetectable levels of fluorescence remaining in the growth solution (**Figure 2.5d, inset 1**), indicating a near quantitative capture of fTMV. To determine if TMV could escape from the ZIF-8 and re-enter the solution, we tested the fluorescence of a fTMV@ZIF-8 solution (**Figure 2.5d insert 2**) over a 24 h period. As shown in **Figure 2.5d** the fluorescence never increased until the shell was removed by treatment with EDTA, indicating that the TMV was unable to leave the ZIF-8 shell and enter into the solution. These data clearly indicate that ZIF-8 shell growth is both high yielding and robust.

An advantage to emerge from encapsulating biomaterials has been stability[33] against environmental stressors such as organic solvents and high temperature, which would typically denature a protein. The stability of the resultant TZ-thin and TZ-thick composites were thus

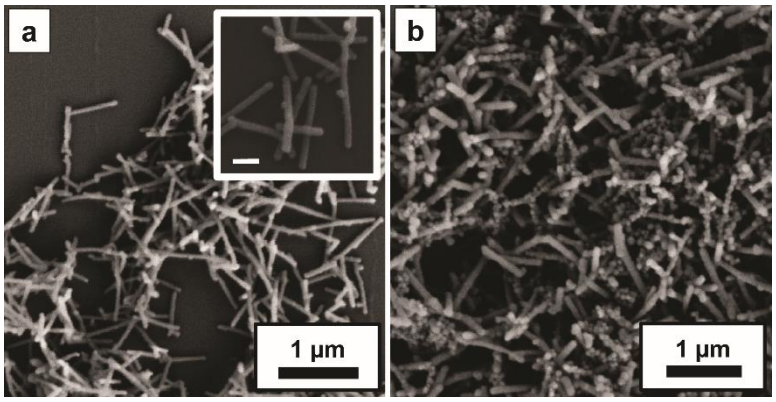

Figure 2.9. SEM micrographs of (a) TZ-thin (inset scale bar= 200 nm) and (b) TZ-thick after soaking in acetonitrile for 16 h.

tested by soaking them in organic solvents of varying polarity. After soaking, we looked at the resulting rods by SEM to confirm the composites retained their distinctive morphology following a 16 h soak (**Figure 2.6 and Figure 2.9**). Both composites fared well in polar solvents (methanol and DMF) and, quite remarkably, TZ-thick was able to soak in DCM[130] without structural degradation while TZ-thin recrystallized into cuboid particles of ZIF-8 (**Figure 2.6c and g**). We were able to further demonstrate the structural stability of TZ-thick by showing the rod-shape of the composite was largely retained even after boiling in water for 20 min (**Figure 2.6h**). We were even able to recover the intact virus after soaking the composite in methanol overnight for 16 h by exfoliating the MOF shell using an aqueous solution of EDTA (**Figure 2.10**). Without the ZIF-8 shell, methanol rapidly turns TMV into a slimy gel (**Figure 2.11**). These results demonstrate that a thick MOF shell serves as robust chainmail for the viral template against a denaturing solvent.[131]

A key benefit to MOFs is their permanent porosity and hitherto, strategies used to create biomimetically mineralized shells on TMV essentially use the protein core as a sacrificial template. This means that the functional group rich surface under the shell is no longer

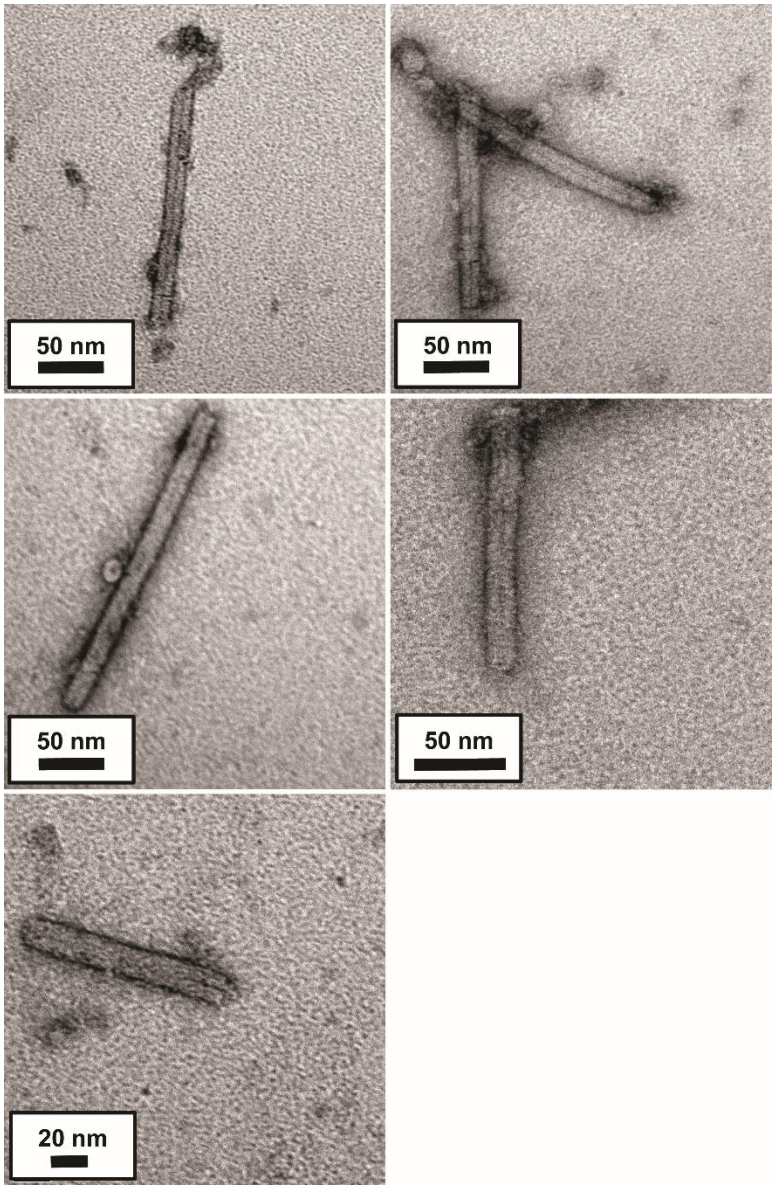

Figure 2.10. Representative TEM micrographs of TMV virus particle obtained following exfoliation of the ZIF-8 shell in a sample of TZ-thick that had been soaked for 16 h in methanol. TZ-thick was immersed in exfoliation solution to remove the ZIF-8 shell.

accessible. Since ZIF-8 contains pores that allow for the diffusion of small molecules,[132-138] we wondered if we could still perform bioconjugation reactions on the TMV surface in TMV@ZIF-8. To demonstrate this, we attempted a classic diazonium coupling reaction[139] to ascertain if the viral core is capable of post-functionalization after formation of the crystalline MOF shell. The

Figure 2.11. TMV functionalized with diazonium dye after soaking in methanol for 16 h. The TMV denatured and formed a gel within 30 min. The TMV is functionalized with a *p*-nitrodiazo dye to better visualize the denaturing.

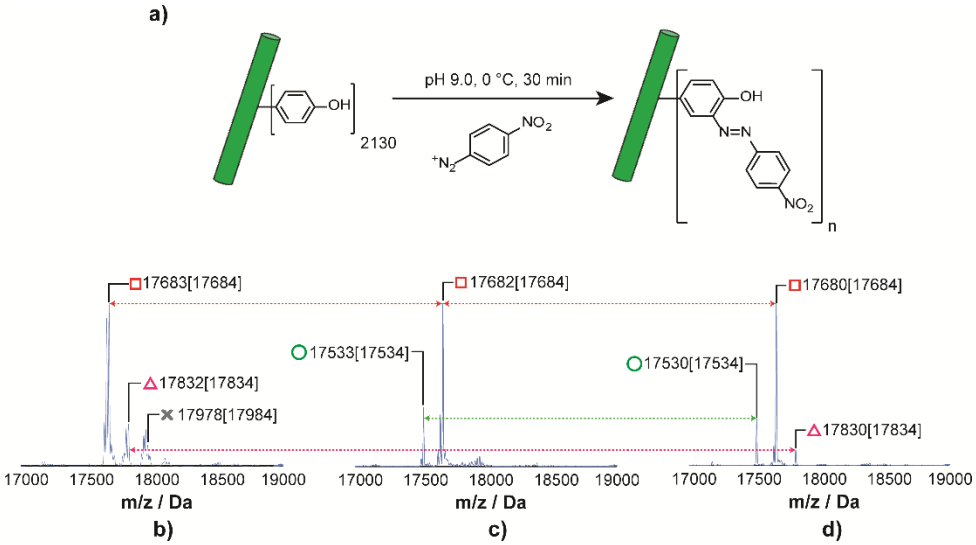

Figure 2.12. a) Diazonium coupling reaction on tyrosine group on TMV. ESI-MS spectrum of TMV coat protein obtained from b) native TMV, c) TZ-thin and d) TZ-thick after diazonium coupling reaction; theoretical mass is quoted for unmodified coat protein (circle), coat protein with one (square), two (triangle), and three (**X**) functionalized residues.

reaction procedure is illustrated in **Figure 2.12a**. A solution of *p*-nitrobenzene diazonium salt was mixed with TZ-thin solution at 0 °C. The whitish starting material quickly turned orange, indicating the formation of a nitrobenzyl diazo dye on the surface of the virus. After 30 min, the reaction mixture was centrifuged, and the mother liquor was decanted. The solid was thoroughly washed with DI water and then suspended in glacial acetic acid to dissolve ZIF-8 and precipitate

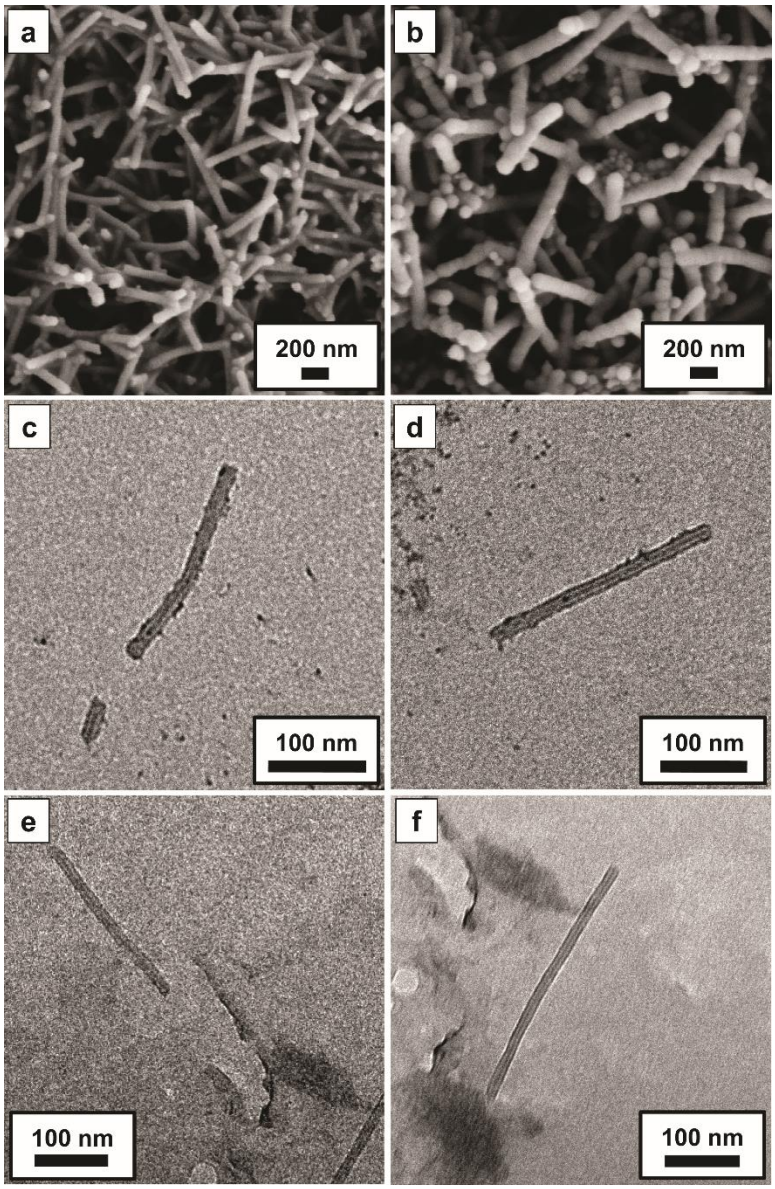

Figure 2.13. SEM micrographs of (a) TZ-thin and (b) TZ-thick after the diazonium coupling reaction. Notably, there has been no change in morphology; (c-f) TEM micrographs of TMV virus particle obtained from TZ-thick after the diazonium reaction and exfoliation of the ZIF-8 shell.

the RNA for analysis by ESI-MS. The deconvoluted mass spectrum, shown in **Figure 2.12c**, shows two intense peaks at 17533 Da and 17682 Da corresponding to unfunctionalized native coat protein and coat protein functionalized with the diazo dye, respectively. Curiously, when the reaction was repeated on TZ-thick,[140] the yield increased (**Figure 2.12d**). This was a slightly

surprising result considering that the shell is thicker. Following removal of the ZIF-8 shell with EDTA, we confirmed by TEM that TZ-thick retained its quaternary structure after the bioconjugation reaction. As shown in **Figure 2.13 c-f**, viral particles stay intact after reaction and exfoliation with EDTA.

CONCLUSIONS

In conclusion, we have successfully prepared TMV@ZIF-8 rod-shaped CSBNs with tunable shell thickness. Morphological (shell thickness) control is possible by tuning the ligand:metal ratio during the shell growth phase. The rod-like core-shell composites are stable in polar organic solvents for 16 h. The core-shell particles with thicker shells show extended stability in low polarity organic solvents and at higher temperature. Post-functionalization on the viral exterior via diazonium coupling reaction is possible, demonstrating that these materials will likely have value to a broad audience. Our synthetic strategy not only provides a novel method for size and morphological control of MOF core-shell systems, but also improves the stability of TMV without losing functionalizability of surface-exposed tyrosine residues. We envision that this synthetic strategy will allow design and fabrication of one-dimensional high aspect ratio nanoparticles with more sophisticated functionalities accompanied with mass storage or transfer. This novel prototype may benefit applications such as drug delivery, imaging, sensing, and catalysis.

Materials, instrumentation, and experimental methods can be found in **Appendix A**.

CHAPTER 3

ENHANCED STABILITY AND CONTROLLED DELIVERY OF MOF ENCAPSULATED VACCINES AND THEIR IMMUNOGENIC RESPONSE IN VIVO[1]

Authors – Michael A. Luzuriaga[†], Raymond P. Welch[†], Madushani Dharmarwardana, Candace E. Benjamin, Shaobo Li, Arezoo Shahrivarkevishahi, Sarah Popal, Lana H. Tuong, Chayton T. Creswell, Jeremiah J. Gassensmith*

The Department of Chemistry and Biochemistry, BSB13.102

The University of Texas at Dallas

800 West Campbell Road

Richardson, Texas 75080-3021

[1]Adapted with permission from Luzuriaga, M. A.; Welch, R. P.; Dharmarwardana, M.; Benjamin, C. E.; Li, S.; Shahrivarkevishahi, A.; Popal, S.; Tuong, L. H.; Creswell, C. T.; Gassensmith, J. J., Enhanced Stability and Controlled Delivery of MOF-Encapsulated Vaccines and Their Immunogenic Response In Vivo. *ACS Applied Materials & Interfaces* **2019,** *11* (10), 9740-9746. [†]These authors contributed equally to this manuscript.

INTRODUCTION

Proteinaceous therapeutics are moving to the forefront of medicine for their specificity in treatments, favorable side effect profiles, and their potential in personalized medicine.[110, 141] Unfortunately, many of these proteins are structurally metastable[142] and they can undergo drastic conformational changes at elevated temperatures, in organic solvents, and at pHs different from physiological conditions.[1-2] These problems limit proteins to short-term low-temperature storage that require costly infrastructure in place to keep them stable throughout shipping. Researchers have been motivated by these limitations and have begun to develop new methods that can enhance protein stability.[14-15, 19, 143-146]

Metal organic framework (MOF) encapsulation has been shown[147] to stabilize enzymes,[33, 148] viruses,[20, 34] and antibodies[18] while providing structural and chemical protection. MOFs are highly porous crystalline materials made of metal ion clusters linked by organic ligand struts[149-150] that have shown promise for use in gas storage[151] and separation,[152-153] catalysis,[154-155] sensing,[156] and small molecules drug delivery.[157-160] Recently, researchers have been shown that MOFs can immobilize[161-162] and stabilize[163-164] biomacromolecules. In particular, coating proteins in zeolitic imidazolate framework-8 (ZIF-8) is proving to be a promising method for protection against conditions normally adverse to proteins, and there have been many promising advancements in this area.[21, 163, 165-167] In particular, biomimetic mineralized growth[20, 33, 162] of ZIF-8 directly on to the surface of a protein has emerged as a means to encapsulate enzymes and insulin using only protein, zinc salts, and methylimidazole directly in water.[168-169] Because ZIF-8 can grow on protein surfaces of different sizes, charge states, and morphologies, this process is quite “agnostic” to the biomolecule host inside the ZIF.[34, 166] This differs from other equally

elegant methods that use bespoke MOFs with tuned[170-172] pore sizes to encapsulate specific biomolecules or polymer encapsulated proteins coated with ZIF and formed in organic protic solvents.[128, 173] For instance, our lab biomimetically encapsulated Tobacco Mosaic Virus (TMV) within a ZIF-8 shell (TMV@ZIF) and found the encapsulation process to be high yielding and promoted by a modest affinity for zinc ions toward the proteinaceous surface.[34] This affinity leads to high local concentrations of zinc, which promotes a mineralization process that results in either core-shell or monolithic crystals of bionanoparticles.[33, 174] It is unclear, however, how—or if—the nucleation and growth affects the secondary or tertiary structure at the protein surface. If the protein surface of a therapeutic protein is altered as a result of the nucleation process, unwanted immunological reactions may occur as human proteins wouldn't be recognized as "self" and antigens for encapsulated vaccines would raise antibodies against a misfolded protein rendering this strategy moot.[175-177] Because an articulated aim[162] of thermally stabilizing proteins is to improve the global distribution of vaccines, which depend upon the fidelity of their folded structure, we were drawn to determine if changes in the immunogenicity of a viral nanoparticle would emerge following encapsulation and administration.

We chose TMV, a 300 nm × 18 nm tubular RNA plant virus, as a model vaccine biomacromolecule owing to extensive data on its *in vivo* performance as a carrier for engineered and chemically conjugated[178-180] epitopes in vaccine development (**Scheme 3.1**). This chemical modifiability, which can occur on both interior and exterior surfaces independently, has given TMV a unique appeal beyond vaccine development as the structure tolerates attachment of dyes,[181] sensors,[182-183] contrast agents,[184] and bioactive molecules.[185-186] The multivalent nature of TMV comes from its 2130 identical coat proteins arranged helically around a 4 nm central

Scheme 3.1. Schematic for analyzing surface effects from encapsulation and stressing: TMV contains glutamate residues, shown in blue, on the interior pore modifiable with EDC chemistry. The viral RNA, shown in orange, is embedded inside the TMV pore. a) Native TMV is incubated with 2-methylimidazole and zinc acetate to form TMV@ZIF. b) TMV@ZIF is subjected to denaturing conditions such as heat and organic solvents. c) Stressed TMV@ZIF is exfoliated with EDTA. d) Recovered TMV surface integrity is characterized by ELISA.

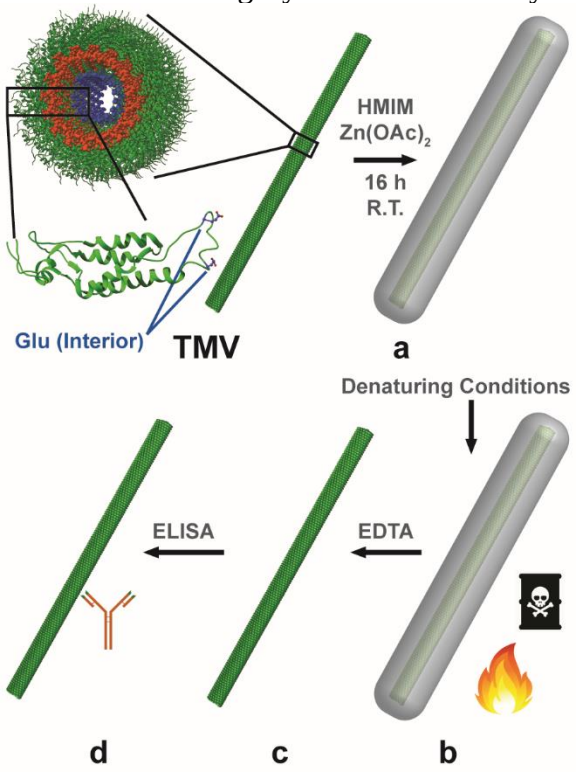

pore where the viral RNA is located. This allows many bioconjugations to the same virus particle, increasing local concentration of active sites and immobilizing them, which is one reason it is thought to be such a useful platform for vaccine development.[178-180]

Since TMV is an established pre-clinical vaccine platform, it is a reasonable model to test the efficacy of thermal protection when encapsulated inside ZIF-8. While it is possible to remove the ZIF-8 shell to obtain pristine TMV, we wondered if this additional step was unnecessary. Indeed, it had occurred to us that the dissolution of ZIF-8, which happens slowly in biological media, may present a method to formulate ‘slow release’ agents for proteins—an area of active

research interest.[187-188] We thus sought to determine if we could simply leave the TMV inside the protective ZIF-8 shell and inject this composite subcutaneously in a mouse model as a method to slowly release TMV, producing an immune response similar to injecting native TMV subcutaneously.

We can quantify changes to the surfaces of TMV as a result of ZIF-8 growth and removal using anti-TMV antibodies measured in an enzyme-linked immunosorbent assay (ELISA). A damaged or unfolded protein at the virus surface will not interact strongly with their complementary antibodies and this loss of affinity will manifest as a diminished ELISA response. The TMV@ZIF composite was subjected to stressors, including heat and denaturing solvents, the ZIF shell was removed, and the recovered protein was examined by ELISA to confirm surface intactness. Tobacco plant infection and *in vivo* studies further demonstrate the viability of ZIF-8 as a protective shell. Finally, we conducted longitudinal *in vivo* studies to ascertain the toxicity and immunogenicity of the TMV@ZIF-8 when implanted subcutaneously. Our results show that this strategy has considerable potential to operate concurrently as a substrate to stabilize proteins at above-ambient conditions as well as deliver them effectively intact and in a more linear dose.

RESULTS AND DISCUSSION

TMV@ZIF can be prepared in a number of different morphologies[34] ranging from bulky rhombic dodecahedra containing hundreds of viruses to discrete rod-shaped core-shell bionanoparticles with a shell thickness tunable from 10 to 40 nm. Each of these morphologies have different colloidal and dispersion characteristics and for this study the following criteria

were considered: i) the composite made had to be dispersible in solution for easy *in vivo* injection, and ii) the kinetics of shell dissolution should allow for complete dissolution of all *in*

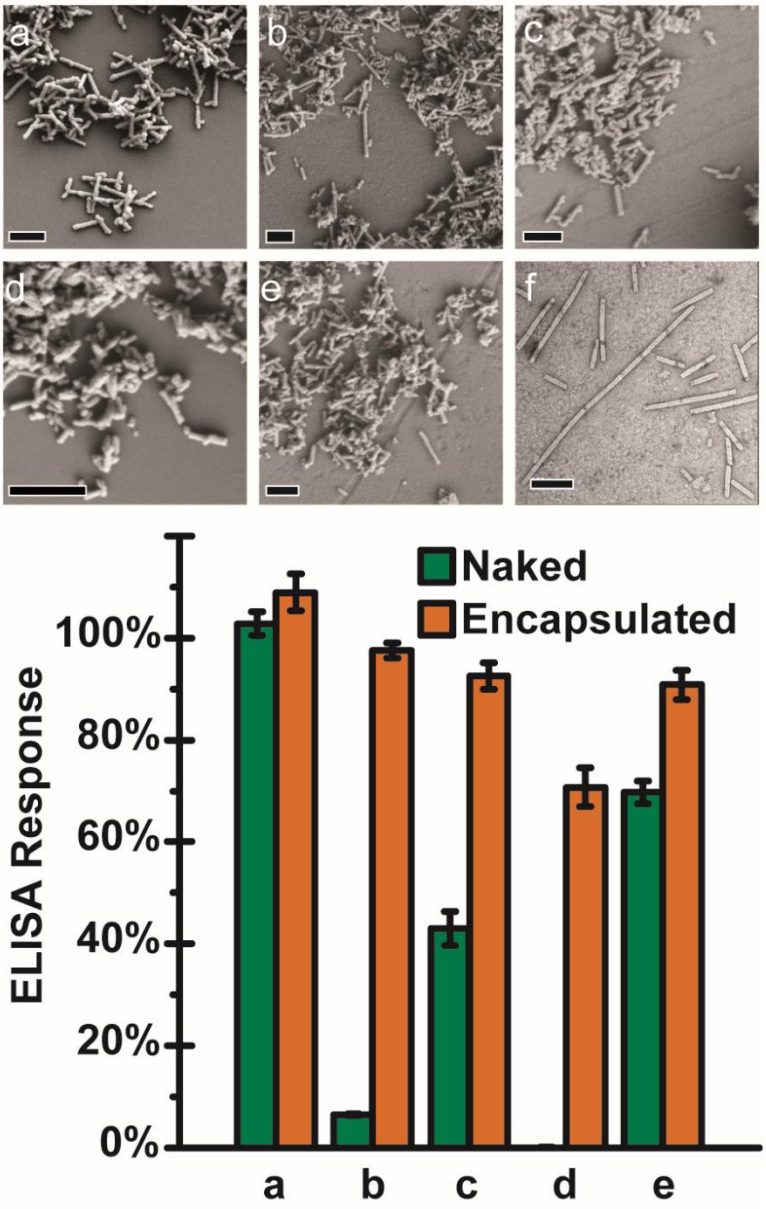

Figure 3.1. Top: SEM images of TMV@ZIF a) non-stressed, b) heating at 100 °C for 20 min, and after soaking overnight in c) methanol, d) 6 M guanidinium chloride, and e) ethyl acetate. Scale bars represent 1 µm. f) TEM image of exfoliated non-stressed TMV. Scale bar is 200 nm. Bottom: The ELISA response of naked and encapsulated TMV subject to no stress (a), heating (b), methanol (c), 6 M guanidinium chloride (d), and ethyl acetate (e). These labels correlate to the SEM images a-e above. The percentages range from buffer blank (0% TMV) to a separate internal control of non-stressed naked TMV (100% TMV).

vivo administered ZIF-8 by the end of our one-month study. When we attempted to suspend rhombic dodecahedra, they settled out of solution too quickly and clogged the syringe. This is in line with literature reports that particles larger than 1000 nm tend to settle rather quickly, making them a difficult material for injection.[189-190] We chose to continue forward with rods, as the ~350 nm particle size allow for them to be easily dispersed into solution and the shell exfoliates more rapidly than the larger rhombic dodecahedra. We thus set out to determine whether the ZIF-8 shell would increase the stability of TMV and if it could be delivered *in vivo*. The encapsulation of TMV into ZIF-8 crystals was obtained by mixing TMV (0.111 mg) with an aqueous solution of 2-methylimidazole (400 mM, 3.0 mL), followed by an aqueous solution of zinc acetate (20 mM, 1.5 mL) (**Scheme 3.1**). After 16 h, the TMV@ZIF particles were collected by centrifugation at 4300 ×*g* and the shell diameter and rod-like morphology were verified by scanning electron microscopy (SEM) (**Figure 3.1a**). The morphology of TMV@ZIF is clearly different from the common rhombic dodecahedral native ZIF-8 crystals.

TMV@ZIF was then stressed under various conditions to determine the stability of the encapsulated virus surface. Stability versus various solvents was tested: soaking in methanol, ethyl acetate, and 6 M guanidinium chloride—a common protein denaturant[191]—overnight. Thermal stability was tested by heating TMV@ZIF to 100 °C for 20 min. After stressing, samples retained their rod-like morphology, as seen in SEM (**Figure 3.1b-e**), and the ZIF-8 shells retained their crystallinity, as seen in PXRD (**Figure 3.2**). The post-stressed composites were exfoliated in EDTA, desalted, and resuspended in 0.1 M sodium phosphate buffer. The protein concentrations were then determined by Lowry assay, and all samples were diluted to 5.0 $\times 10^{-4}$ mg/mL and ELISA response determined. Since changes in the viral proteins surface are

being investigated, the ELISA results were normalized to naked non-stressed TMV (100%), and buffer blank (0%) for comparison between the two. We were pleased to discover that the process of the shell formation and exfoliation did not significantly alter the protein surface and that the shell confers considerable protection to TMV when exposed to high temperatures. For instance, the percent difference between naked TMV and TMV@ZIF when heated to 100 °C for 20 min was 165.0% (**Figure 3.1 bottom, Table 3.1**). Likewise, the percent difference between protected and unprotected exposure to the strongly denaturing guanidinium chloride was 199.2% (**Figure 3.1 bottom**). We were also able to demonstrate that the ZIF was able to confer protection against other denaturing organic solvents (**Table 3.1**). Percent difference was calculated according to the equation: $\frac{|V_1 - V_2|}{\left(\frac{V_1 + V_2}{2}\right)}$ where V_1 and V_2 are values expressed in percentages.

Table 3.1. ELISA values of stressed TMV, stressed TMV@ZIF, and their percent differences

Stress	Naked	Encapsulated	Percent Difference
Non-Stressed	102.8 ± 2.3%	108.9 ± 3.6%	3.9%
Heated	6.447 ± 0.188%	97.53 ± 1.52%	165.0%
Methanol	43.02 ± 3.26%	92.49 ± 2.63%	55.42%
6 M Guanidine HCl	0.09033 ± 0.08277%	70.70 ± 3.78%	199.2%
Ethyl Acetate	69.72 ± 2.25%	90.81 ± 2.84%	18.33%

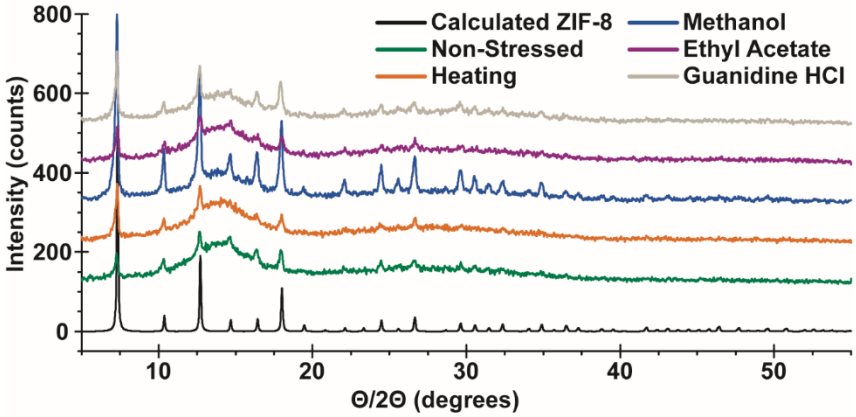

Figure 3.2. PXRD spectra of stressed TMV@ZIF samples.

We then set out to determine whether encapsulating TMV would damage the RNA. To assess the protection that TMV@ZIF has on the RNA of TMV, *Nicotiana benthamiana* plants were inoculated with phosphate buffer as a negative control, TMV@ZIF, TMV@ZIF exfoliated with EDTA, and native TMV as a positive control. The infection of *N. benthamiana* depends on the disassembly of the capsid to liberate the intact viral RNA and begin replication. Consequently, any damage to the RNA will reduce viral load in plants.

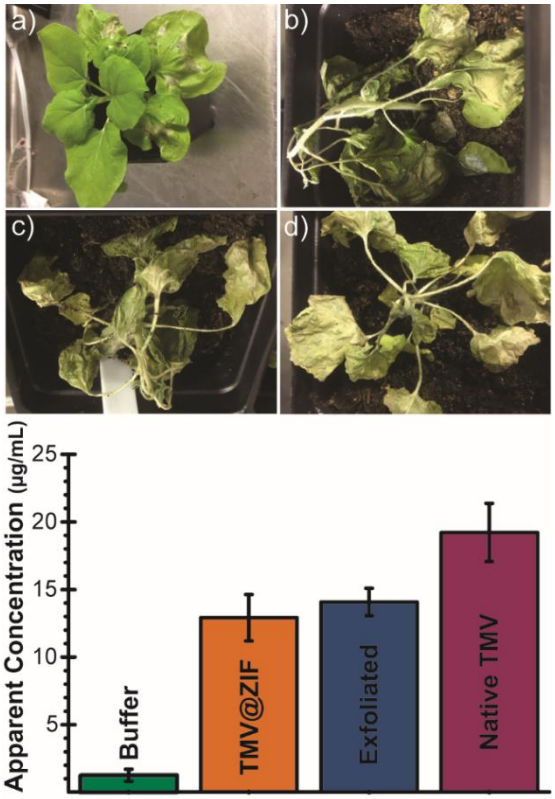

Figure 3.3. Top: *N. benthamiana* plants 10 days after inoculation with a) 0.1 M pH 7.4 potassium phosphate buffer as a negative control, b) TMV@ZIF, c) exfoliated TMV@ZIF, and d) native TMV as a positive control. Bottom: A bar graph showing the viral recovery of TMV from 1 g of harvested leaves measured by ELISA. Leaves were inoculated with buffer as a negative control, TMV@ZIF, exfoliated TMV@ZIF, and native TMV as a positive control.

Inoculated leaves were collected after 10 days post infection. Visually, the control plants remained green and the other plants withered (**Figure 3.3a-d**). ELISA was performed on 1 g of

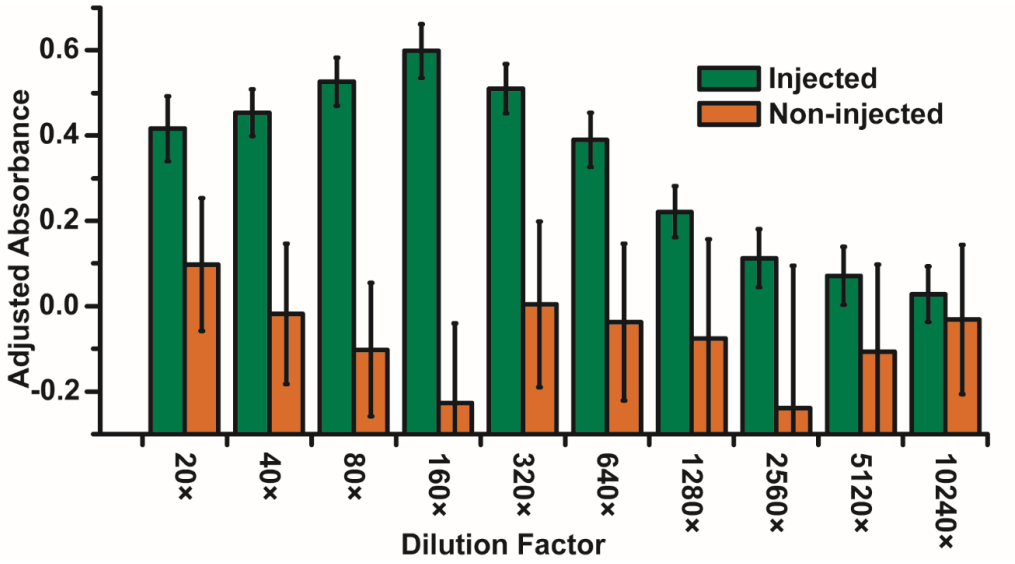

Figure 3.4. ELISA response of test mice after 10 days.

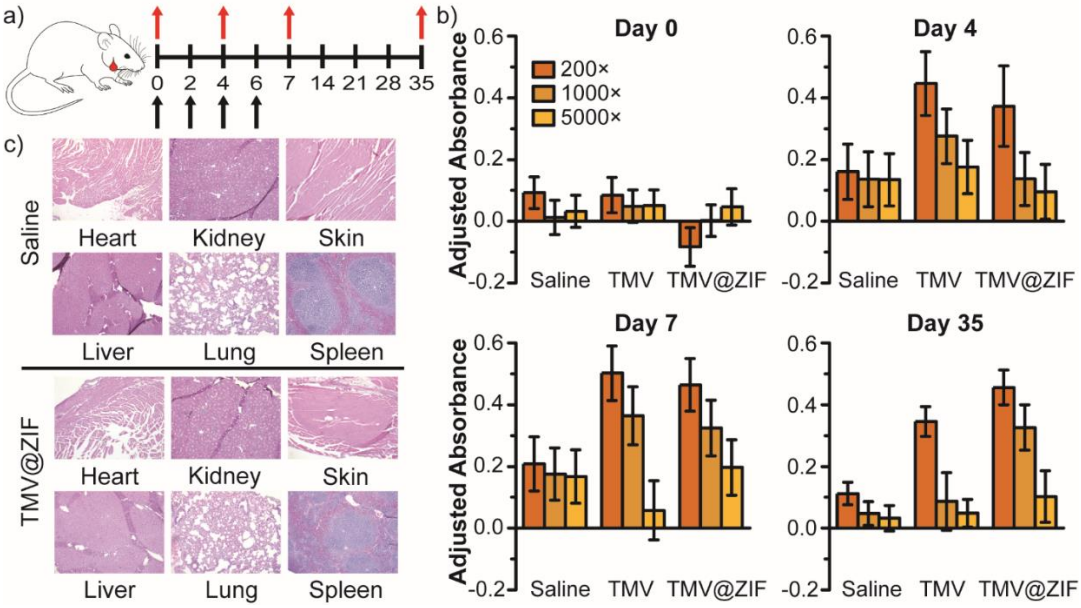

Figure 3.5. a) Time schedule showing the days the mice were injected (black arrows) and submandibular blood withdrawals were performed (red arrows). Serum samples were diluted 200×, 1000×, and 5000×. b) ELISA response for each time point, buffer blank subtracted. c) hematoxylin & eosin Y staining of saline and TMV@ZIF injected mice.

leaves macerated in 10 mL of extraction buffer and centrifuged to remove the large plant matter. Since the relative amount of TMV present in the leaf matter was being investigated, the ELISA results were fit to a standard curve of native TMV and results reported as apparent TMV

concentration in μg/mL. The TMV@ZIF, exfoliated TMV@ZIF, and native TMV plants showed a clear increase in ELISA response compared to the buffer-inoculated plants, with percent differences of 164.32% (a 10-fold increase), 167.01% (an 11-fold increase), and 175.29% (a 15-fold increase), respectively (**Figure 3.3 bottom**). This indicates that the TMV remains virulent and that the RNA survives the encapsulation and exfoliation process.

We next turned our attention to *in vivo* studies on murine models to determine i) whether the virus would release from the protective ZIF shell *in vivo*, ii) how the antiTMV IgG production against subcutaneously administered TMV@ZIF compares to native TMV, and iii) the biocompatibility of TMV@ZIF composite. In order to determine relative antibody production and optimize serum dilutions, 2 groups (n = 4) of BALB/c test mice were either non-injected or injected subcutaneously with native TMV and blood drawn after 10 days. In the test mice, there was a clear antiTMV ELISA response in mice injected with native TMV compared to non-injected mice after 10 days, and an optimal serum dilution range of 200× to 5000× was found (**Figure 3.4**). To continue our investigation, 12 BALB/c mice were divided into three groups (n = 4) and subcutaneously injected on day 0, 2, 4, and 6 with saline, native TMV, or TMV@ZIF. Multiple injections were administered to enhance the antibody production levels in mice. We hypothesized that the TMV@ZIF would protect the encapsulated TMV in the body for as long as native TMV and result in a similar antibody production level. Submandibular blood draws were conducted on day 0, 4, 7, and 35 (**Figure 3.5a**). The ELISA response, which measures the production of mouse antibodies against TMV, shows that the TMV@ZIF elicits an antibody response comparable to naked TMV (**Figure 3.5b**). Antibody production typically depends upon successful uptake by antigen presenting cells (APCs)—for instance macrophages and dendritic

cells—in the body. This means that the shell is being removed before or during APC uptake. Exactly what is happening requires further study; however, there is literature precedent[165] that ZIF-8 can dissolve in the presence of cell media and it is not unexpected that ZIF-8 would dissociate in the interstitial fluids of the subcutaneous region prior to cellular uptake. The antibody levels that were detected for the composites were comparable to that of naked TMV, confirming that the TMV@ZIF does not need to be exfoliated before administration. Five days after the last blood withdrawal, hematoxylin and eosin Y (H&E) stained images were taken on various organs for each mouse to further evaluate TMV@ZIF biocompatibility. No visual difference could be determined between mice injected with saline and with TMV@ZIF (**Figure 3.5c**). This confirms the biocompatibility of TMV@ZIF, following multiple subcutaneous injections with no apparent toxicity or behavioral changes in the mice. While some literature has shown *in vitro* toxicity,[165, 192] our study has concluded that these results may not translate *in vivo*.

Our method depends upon the slow degradation of ZIF-8 *in vivo* by physiological salts and macromolecules, suggesting that encapsulation and protein-ZIF composite formation may be an intriguing way to prolong a linear dose of protein-based drugs. This could be especially useful for the administration of insulin and vaccines, which typically require multiple injections over time to achieve a sustained effect.[193] Histology of the tissue at the subcutaneous site of administration at the conclusion of the study—which consisted of four consecutive TMV@ZIF injections—did not uncover any residual material, tissue damage, or scarring, which lead us to suspect that the full dose was being absorbed into the animal, as shown in **Figure 3.5c**.

To better understand the rate at which TMV@ZIF was taken up by the mouse, we conducted time dependent *in vivo* imaging using TMV labeled on its interior with the red-

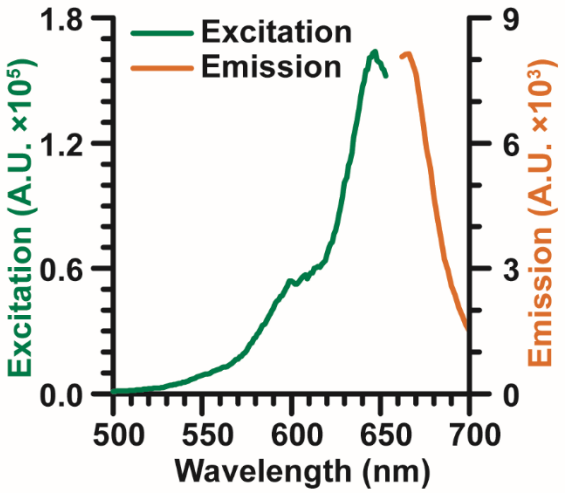

Figure 3.6. Excitation and emission spectra of Cy5-TMV. Excitation λ_{max} = 647 nm; Emission λ_{max} = 666 nm

emitting fluorophore Cy5 (Cy5-TMV, **Figure 3.6**). The Cy5-TMV concentration was determined by NanoDrop to be 12.59 mg/mL and the apparent Cy5 concentration by UV-Vis was 37.44 µM (**Figure 3.7**). Calculating the number of moles of Cy5 and TMV present in the Cy5-TMV (TMV M.W. = 4.08 ×10^7 g/mol, Cy5 M.W. = 746.97 g/mol), the average number of Cy5 molecules per TMV rod was determined to be 12.13. This labeled TMV was encapsulated inside ZIF-8, which caused a quenching of the red fluorescence (**Figure 3.8**). This fluorescence of Cy5-TMV was restored in full when the shell was removed, providing a clear indication of shell removal. For this study, 6 BALB/c mice were divided into two groups (n = 3), shaved to remove the hair on their torso and limbs, and injected subcutaneously with either un-encapsulated Cy5-TMV or Cy5-TMV@ZIF and imaged over two weeks. The images shown in **Figure 3.9b** show that, prior to injection, the only fluorescence comes from the hairs near the head. As shown in the series of images in **Figure 3.9c**, subcutaneous injection of Cy5-TMV decayed slowly over a period of 120 h. In contrast, the Cy5-TMV@ZIF fluoresced weakly at first, followed by an increase then

gradual decay. After 288 h, the fluorescence at the injection site for the encapsulated material returned to baseline (**Figure 3.9a**).

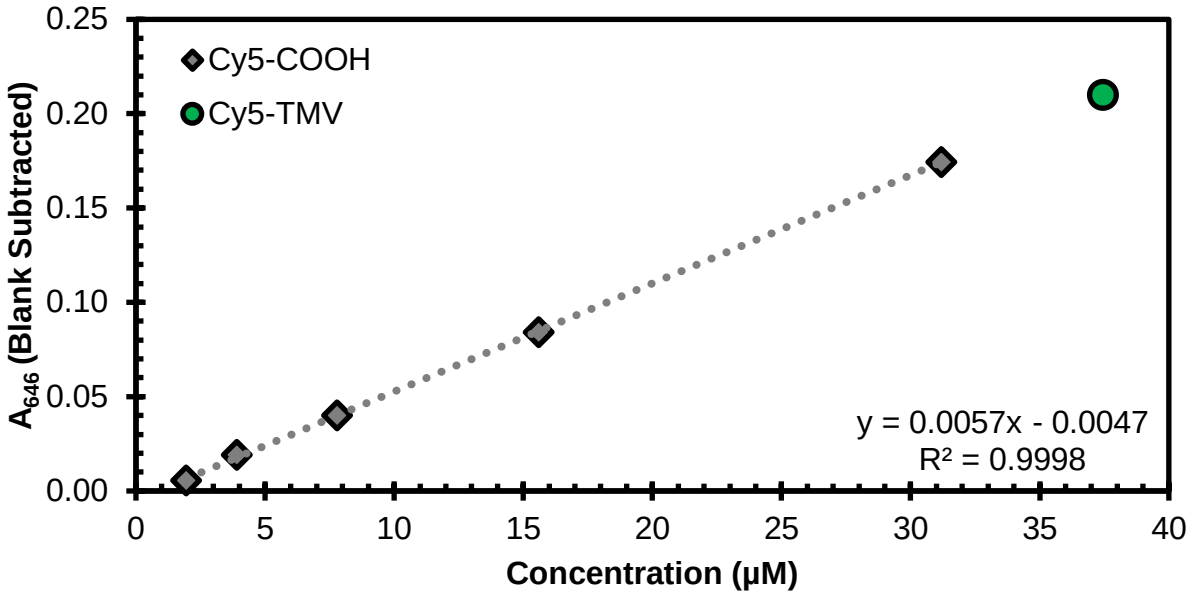

Figure 3.7. UV-Vis absorbance at 646 nm of Cy5-COOH in solution and Cy5-TMV.

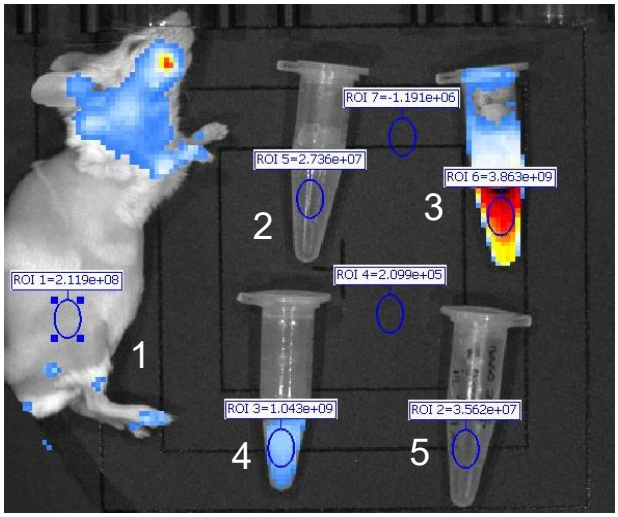

Figure 3.8. Regions of interest and their and their radiant efficiencies ($\times 10^7$): 1) Mouse skin: 21.2, 2) Saline: 2.7, 3) Cy5-TMV: 386.3, 4) Cy5-TMV@ZIF: 104.3, and 5) ZIF-8 in water: 3.6. It should be noted that the quantity of Cy5-TMV in tubes 3 and 4 are the same, however, the ZIF shell attenuates the fluorescence.

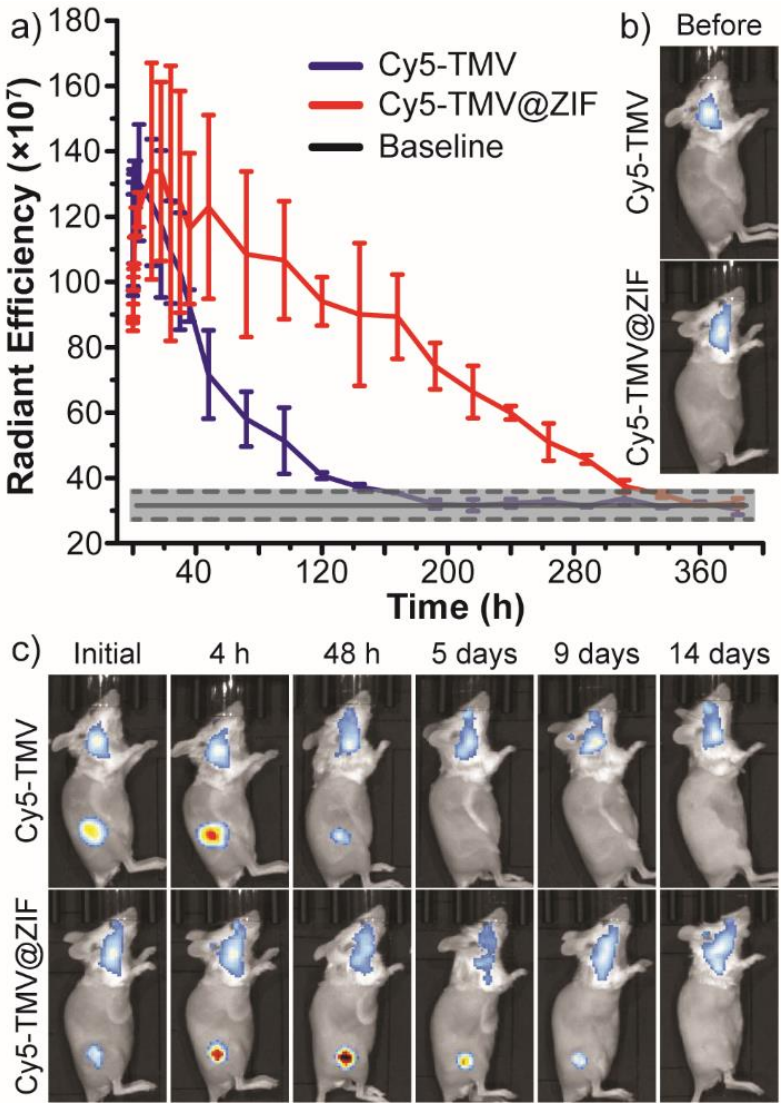

Figure 3.9. a) Fluorescence intensity over time. The baseline is the average fluorescence intensity of 4 mice before injection. The dashed line represents the error of the baseline. b) Images of the mice prior to injection of Cy5-TMV or Cy5-TMV@ZIF. The mice were shaved, and the only initial fluorescence comes from the hairs on the head. c) After injection and time point images of Cy5-TMV or Cy5-TMV@ZIF.

CONCLUSIONS

The results of this study strongly indicate that ZIF-8 coatings not only provide protection against denaturing solvents and heat, but the nucleation and growth of the crystalline lattice does not alter the secondary or tertiary structure of protein and protein ensembles. Further, the shell

does not significantly damage the viral RNA. The ZIF-8 shells are exceptionally easy to synthesize on proteins, their composites are formed in a few seconds, and are ready to use within hours. It is clear from histology data that prolonged exposure to ZIF-8 does not alter tissue morphology at either the injection site or distal organs. Qualitatively, we saw no behavior changes in mice following administration, nor did any mice become ill or die as a result of prolonged exposure to TMV@ZIF composites. On the other hand, *in vivo* data clearly suggest that the administration of equal quantities of immunogenic protein yielded identical antibody responses, showing that the release of the protein from the ZIF shell occurs to completion. This was further corroborated with time-dependent *in vivo* imaging studies, which showed a time-delayed release of the injection over the course of 14 days—a property of ZIF-8 we aim to exploit in subsequent studies. Taken together, these data strongly suggest ZIF-8 based shells may provide a method to concurrently protect and deliver proteinaceous drugs safely.

Materials, instrumentation, and experimental methods can be found in **Appendix B**.

CHAPTER 4

INVESTIGATION OF ZIF-8 MINERALIZATION OF PROTEINACEOUS PARTICLES

INTRODUCTION

Therapeutic proteins are rapidly becoming a major means of combating many diseases. As the number of therapeutic protein drugs available continues to rise, more methods to prolong their viability are needed to combat the inherent instability of proteins outside of a relatively narrow thermal and chemical range. The field of biomimetic mineralization of proteinaceous material with metal organic frameworks (MOFs) continues to grow with these needs, and a fundamental understanding of the mechanisms and conditions that facilitate MOF nucleation and growth is needed. A major goal in protein@MOF composite synthesis is to provide thermal, chemical, and mechanical protection to the protein, whether for cold chain remediation,[21] enhanced therapeutic activity,[194] or prolonged drug release.[195] The most commonly studied MOF in this regard has been zeolitic imidazolate framework 8 (ZIF-8), composed of zinc ions and 2-methylimidazole (HMIM) ligands. There have been some investigations[34, 196] into protein-specific ZIF-8 formation mechanisms, but there has not been a comprehensive study to link them together. This metastudy aims to compile a list of works to compare various ZIF-8 encapsulation conditions on different proteins and virus particles supplemented by experimental data to elucidate a pattern that may indicate more general mechanisms.

RESULTS AND DISCUSSION

Our previous work[34] of ZIF-8-coated TMV was examined and converted to final concentrations of metal, ligand, and protein in the reaction solution. These data were plotted on a bubble graph of metal per protein mass versus ligand-metal ratio with bubble size proportional to

protein concentration, in addition to TZ-Thin and TZ-Thick conditions from our other work[20] (**Figure 4.1**). The morphologies of the composites reported were cross-correlated to possibly identify areas of the parameter space to further explore with different proteins and other studies in the literature. The goal was to identify a pattern of reaction conditions to apply to general protein encapsulation. It was found that a region not well explored was at low concentrations of zinc and low ligand-metal ratios, as seen by the lack of data points in the lower left corner of **Figure 4.1**.

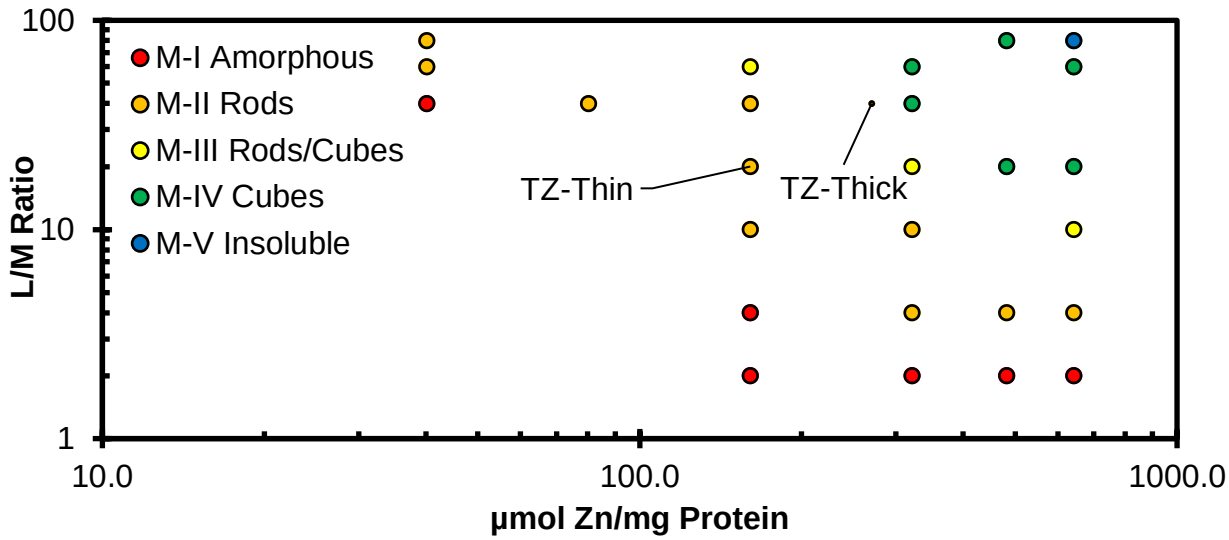

Figure 4.1. Conversion of the TMV@ZIF Li Plot from reference [34] and conditions from reference [20] to final metal and protein concentrations versus ligand-metal ratio on a log-log plot.

Other works[33, 196-200] that reported rhombic dodecahedral ZIF-8 composites of different encapsulated proteins were then plotted (**Figure 4.2**) by parsing experimental conditions and converting them to be read on the plot. It was hoped that a pattern would emerge, and a suitable set of conditions could be identified for general protein encapsulation. Only conditions involving proteinaceous material, 2-methylimidazole, and zinc salts were used; methods that added

excipients such as PVP or NaCl were not included, nor were methods of encapsulation in thin films.

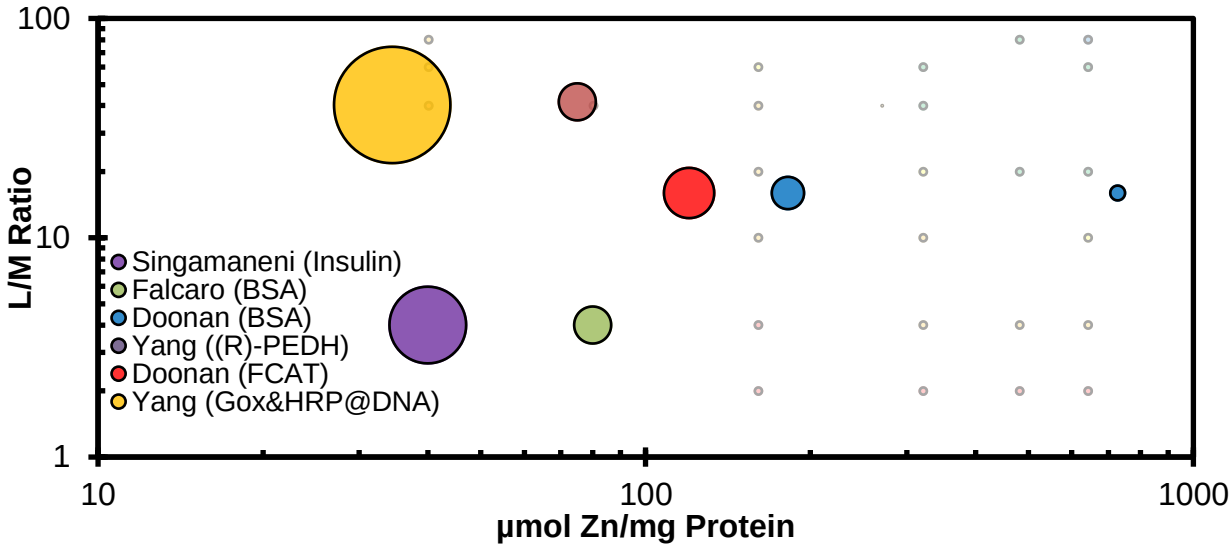

Figure 4.2. Experimental conditions from other works converted and plotted on the graph. The data points from Figure 4.1 are included for reference.

Several areas were identified to explore with TMV, TMV CP, BSA, and bacteriophage Qβ as the encapsulated proteins (**Figure 4.3**). Encapsulations were performed by mixing the protein of interest with 0.5 mL of a 2-methylimidazole solution, adding 0.5 mL of zinc solution, incubating for 16-18 hours, collecting composites by centrifugation, washing them with water and methanol, and examining morphology by SEM (**Figures 4.4 – 4.9**). The precursor and protein concentrations were adjusted such that the final concentrations in the incubation solution after mixing were the same as conditions reported, though the volume was kept low to facilitate multiple parallel reactions without running out of protein material. Variables investigated were moles of zinc per mass of protein, moles of HMIM per mass of protein, ligand-metal ratio, precursor solution concentrations, final protein concentrations, and type of protein.

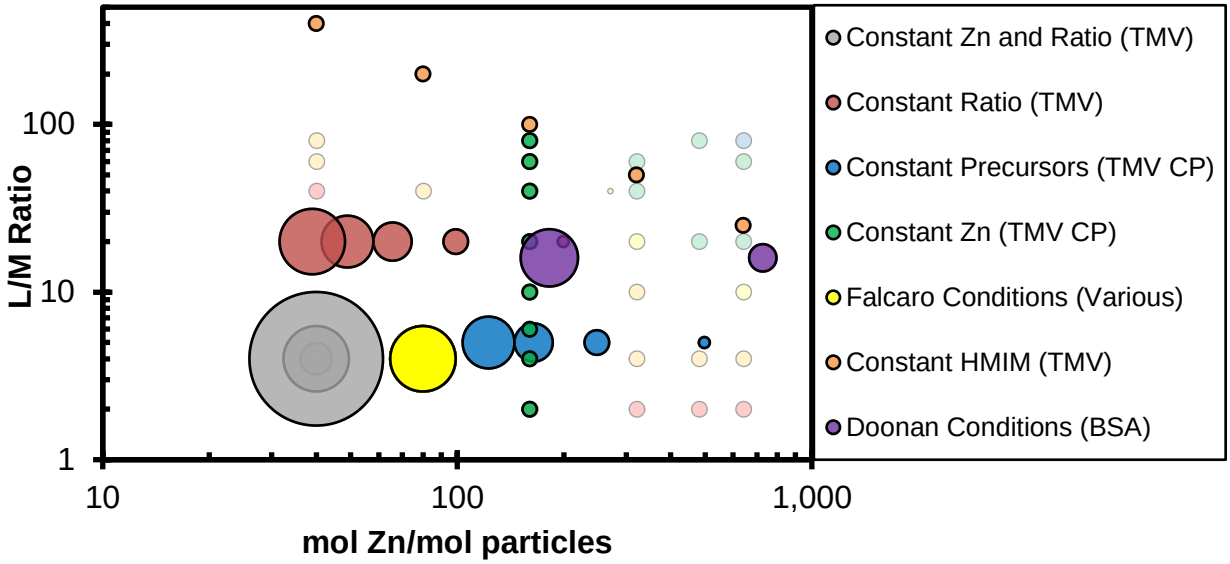

Figure 4.3. Plot of experimental conditions.

First, conditions at the same final Zn concentration and L/M ratio as Singamaneni[197] but with varying final protein concentrations were tried, using TMV as the protein (**Figure 4.3, grey bubbles**). In this region, a TMV concentration that was the same as our previous work would be expected to be amorphous. I postulated that higher protein concentrations might yield rods or even rhombic dodecahedra. As seen in **Figure 4.4**, increasing protein concentrations led to more of a net-like pattern, and no discrete particles. Next, a series of conditions at constant L/M ratio and zinc precursor volume was tried at different protein concentrations. The constant zinc precursor concentration with different protein precursor volumes led to different zinc per protein values (**Figure 4.3, maroon bubbles**). This set of conditions formed a line in 3D space (if the protein concentrations were plotted on a *z*-axis) that would intersect the plane of the Li Plot[34] at the TZ-Thin location. Therefore, rods were expected at that point, and morphologies at points further away were investigated. As shown in **Figure 4.5**, as the protein concentration increased while the zinc per protein decreased, the morphology moved from mostly rods to mostly

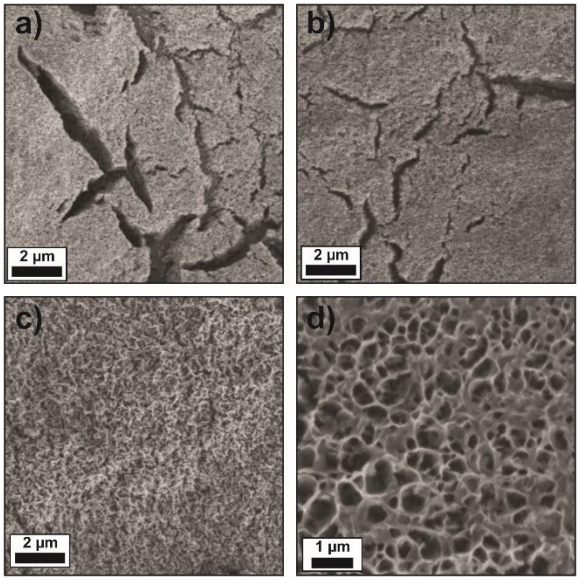

Figure 4.4. SEM images of TMV@ZIF created with constant Zn and HMIM at protein concentrations of a) 0.0625 mg/mL, b) 0.125 mg/mL, c) 0.25 mg/mL, and d) 0.5 mg/mL.

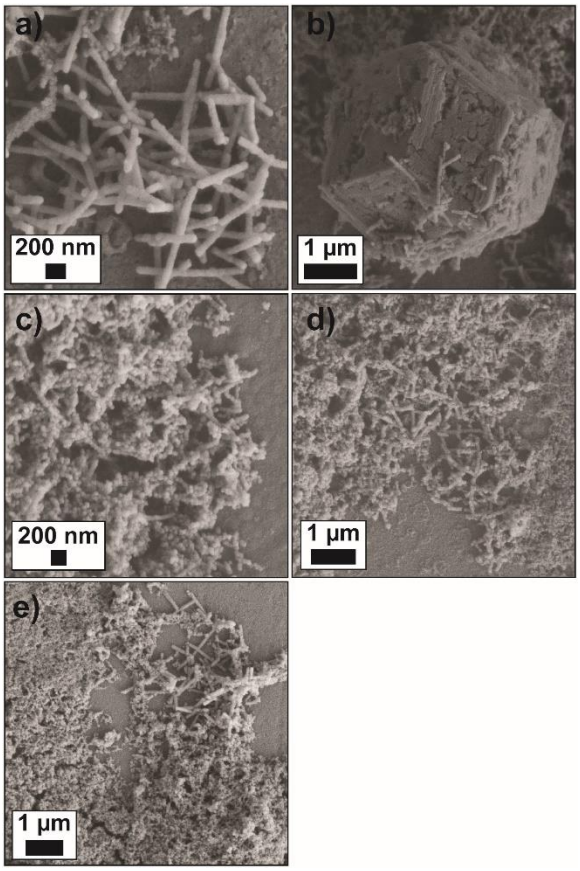

Figure 4.5. SEM images of TMV@ZIF created with constant L/M ratio at protein concentrations of a) 0.05 mg/mL, b) 0.10 mg/mL, c) 0.15 mg/mL, d) 0.20 mg/mL, and e) 0.25 mg/mL.

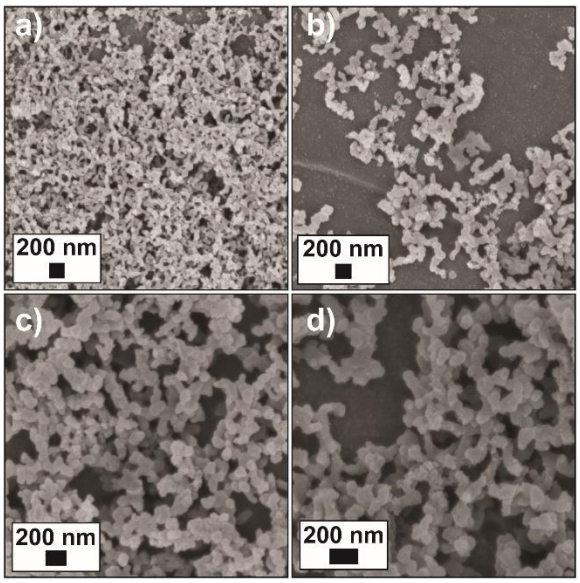

Figure 4.6. SEM images of TMV CP@ZIF created with constant precursor concentrations at protein concentrations of a) 0.05 mg/mL, b) 0.10 mg/mL, c) 0.15 mg/mL, and d) 0.20 mg/mL.

granules. This set of conditions – constant L/M ratio and zinc precursor – was repeated in a different area of the plot (**Figure 4.3, blue bubbles**) and with TMV coat proteins as the protein. Because there is no possibility of rod-like morphology with individual coat proteins, morphologies were examined for discrete particles and rhombic dodecahedra. As shown in **Figure 4.6**, discrete particles were found at all conditions tested, with no rhombic dodecahedra or amorphous mass present. TMV CP were then investigated at constant zinc per protein and final protein concentration with different L/M ratios (**Figure 4.3, green bubbles**). The range of ratios were chosen to span the entire plot from the amorphous region to the rhombic dodecahedra region. I wanted to see if the area that rhombic dodecahedra appears coincided with that for whole TMV particles. As shown in **Figure 4.7**, at low L/M ratios, 4-fold crystals formed with small amounts of amorphous matter. These are likely either zinc oxide or zinc acetate crystals. As the L/M ratio increased, discrete particles could be found up until a ratio of 40, when large rhombic dodecahedra formed in addition to the particles. As the ratio further increased, the

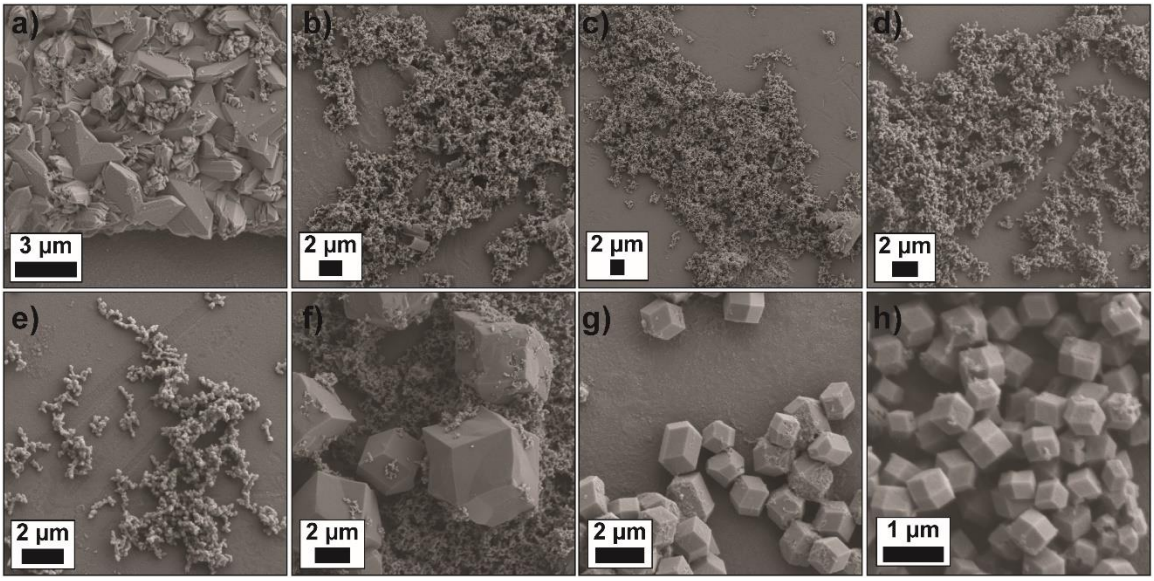

Figure 4.7. SEM images of TMV CP@ZIF created with constant Zn and protein concentration at L/M ratios of a) 2, b) 4, c) 6, d) 10, e) 20, f) 40, g) 60, and h) 80.

number of discrete particles decreased and so did the size of the rhombic dodecahedra, until a ratio of 80, where only rhombic dodecahedra could be found. This border coincides with the Region M-III (Rods/Cubes) border from the Li Plot. This suggests that the L/M ratio is an important factor in determining morphology. Next, conditions identical to those reported by Falcaro[33] were tested with different protein sources, including BSA – which was used in Falcaro's study. It was hoped that these conditions would reveal whether cuboid particles could be obtained on either BSA, TMV CP, or even virus particles like Qβ and TMV (**Figure 4.3, yellow bubble**). As shown in **Figure 4.8**, all types of proteins resulted in discrete particles, but no cuboids. It was noted, however, that TMV produced rods, despite being in the amorphous region, even with a different protein concentration. This suggests that different protein concentrations might shift the borders of the regions in the Li Plot. Next, conditions were chosen with TMV to investigate formation of rhombic dodecahedra at very high L/M ratios at constant HMIM per protein and protein concentration (**Figure 4.3, orange bubbles**). It was hoped that

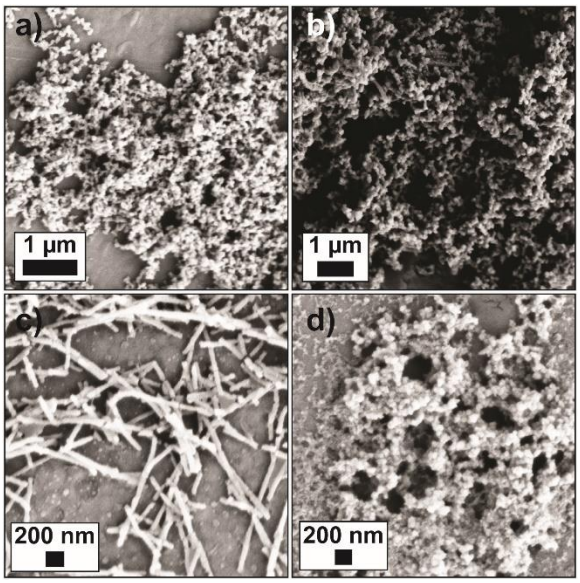

Figure 4.8. SEM images of Protein@ZIF created at the same conditions as Falcaro[33] with different protein sources: a) BSA, b) TMV CP, c) TMV, and d) Qβ.

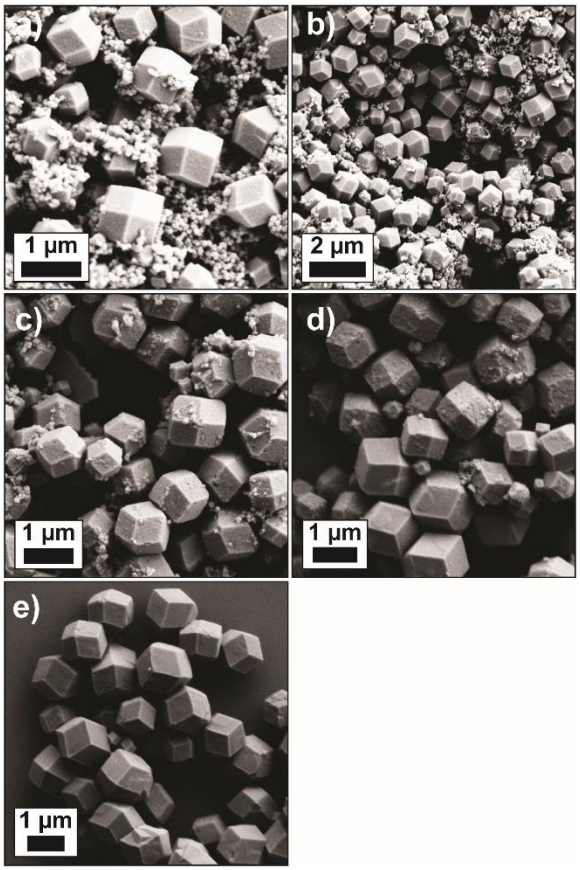

Figure 4.9. SEM images of TMV@ZIF created with constant HMIM at L/M ratios of a) 400, b) 200, c) 100, d) 50, and e) 25.

these conditions were firmly within the rhombic dodecahedra region of the Li Plot and that at least at higher zinc and thus lower L/M ratios rhombic dodecahedra would appear. As shown in **Figure 4.9**, at low zinc and high L/M ratio, rhombic dodecahedra do indeed form, in addition to small granules. As the zinc per protein increases, the L/M ratio decreases, and the conditions move into the main area of the Li Plot, and the granules decrease in number. The rhombic dodecahedra are the same size through all the conditions and become sharper and more ideal as the zinc increases. This suggests that the amount of HMIM per protein plays a role in the size of the rhombic dodecahedra.

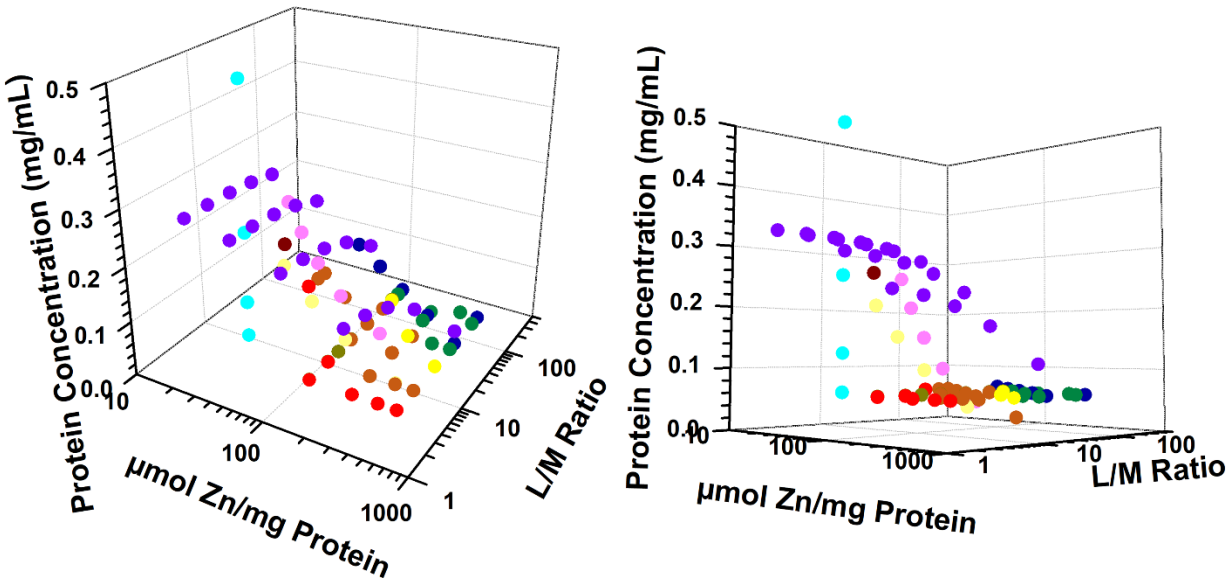

Figure 4.10. 3D Plot (2 views) of the explored parameter space.

A summary of the explored space on a 3D plot of zinc concentration versus ligand-metal ratio versus protein concentration can be found in **Figure 4.10**. The Li Plot is found as a horizontal plane at 0.0625 mg/mL protein concentration and colored in red, orange, yellow, green, and dark blue. Also included in purple is the converted ternary plot data from Doonan.[196] The explored conditions were plotted versus several different criteria. Since different types of

proteins encapsulate in different ways, the amount of protein was converted to the number of expected particles. TMV, for example, has a very small number of particles per mass of protein, because its 2130 copies of the 17534 Da coat protein are all part of a single virus particle. Separated TMV coat proteins, if individually encapsulated, would have 2130 times more particles than individually encapsulated TMV rods. Therefore, the moles of zinc per moles of expected particles were plotted against the ligand-metal ratio (**Figure 4.11**). The difference in class of protein material (individual proteins versus whole virus particles) can be clearly seen, though this does not reveal any particular pattern.

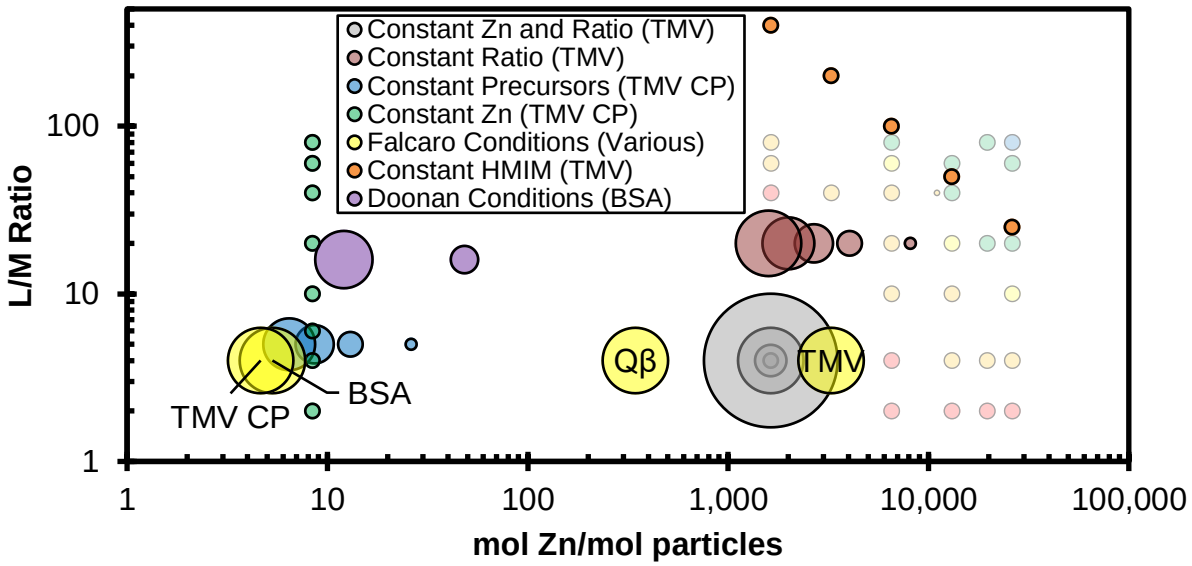

Figure 4.11. Plot of moles of zinc per moles of expected particles versus L/M ratio.

CONCLUSIONS

Through this metastudy, it was found that the ligand-metal ratio plays an important part in determining final morphology of ZIF-8 encapsulation of various protein material. The final concentration of ligand affects the particle size, and the protein concentration affects the encapsulation quality. Further efforts to codify encapsulation conditions from the literature on a

variety of proteins supplemented by further experimental conditions will help identify optimal conditions for protein encapsulation in ZIF-8. This would allow a good starting point for optimization of vaccine encapsulation and further reduce the need for cold chain infrastructure.

Materials, instrumentation, and experimental methods can be found in **Appendix C**.

CHAPTER 5

REVERSIBLY THERMOSALIENT NDI CRYSTAL SWITCH

From manuscript in preparation, Welch, R. P.[†]; Dharmarwardana, M.[†]; Caicedo-Narvaez, C.; Luzuriaga, M. A.; Arimilli, B. S.; McCandless, G. T.; Fahimi, B.; Gassensmith, J. J. Reversibly Thermosalient NDI Crystal Switch. [†]These authors contributed equally to the manuscript.

INTRODUCTION

Materials that can transduce heat into well-defined and directed motion have a wide range of applications for are needed in a diverse array of technologies from microscopic pumps to energy harvesting. For instance, transducing well-defined thermally induced reciprocating actuation simply by taking advantage of the natural temperature fluctuation between day and night cycles is a possible way to harness ambient temperature changes into useful pollution-free electricity. In addition, the ever-increasing interest in the miniaturization of mechanical devices demands new actuating materials that can produce motion in the micron to millimeter regime. While actuators that operate from electrochemical stimuli are well-known,[201-202] the application of thermal expansion actuators has been limited by poor mechanical properties, material fatigue, or low coefficients of thermal expansion (CTEs). For instance, metallic aluminum and lead, which have the highest known CTEs in pure metals, are still in the regime of 20×10^{-6} K^{-1}. Thermo-responsive actuating shape-memory polymers have been developed,[203-206] but they typically require a change in the global environmental temperature to actuate.[207]

Dynamic crystals are mechanically active single crystalline entities capable of amplifying small changes in molecular packing into large-scale anisotropic macroscopic motion. These materials—so-called thermosalient solids—have CTEs over an order of magnitude higher than

the best pure-metals and undergo phase transitions at rates exceeding 10^5 times faster than non-thermosalient transitions.[208] This expansion is caused by a diffusionless "sergeants and soldiers" phase transition that is initiated at crystalline extremities and rapidly propagates throughout the crystal.[46, 209] Unfortunately, these crystals are typically undergo a single and irreversible crystal-to-crystal (SCC) phase transition that results in their destruction by splitting, jumping, or even dramatically exploding. These irreversible dynamic crystals have found applications as fuses,[62] making use of their one-time ability to actuate to break a circuit, however this irreversibility greatly limits their applications. In contrast to irreversible systems, there are very few reversible systems, and most of these are limited to a dozen or so cycles before the crystal degrades. Designing such systems is complicated by the fact that structure-function relationships in molecular crystals can be difficult to derive and thus *a priori* synthesis of actuating materials is challenging.

In this report we show a synthetic strategy in a family of thermosalient crystals we developed that lead us to a fully reversible actuator capable of over 200 cycles and room temperature stability for multiple years. Our family of actuating molecular crystals is based on a naphthalene diimide (NDI) core with alkoxyphenyl substituents.[46] By varying the number of carbon atoms on the alkyl chain,[210] we report that the irreversible thermosalient behavior is tunable across temperature ranges by altering the alkyl chain from four to nine carbons. Here we report that, when the alkyl chain is 10 linear carbons, the thermosalient crystals reversibly shrinks to 90% of its original length instantaneously upon heating beyond 45 °C and, upon cooling below 35 °C, the crystal instantaneously expands back to its original length. This temperature regime is important because it occurs around physiologically important

temperatures, where thermal fuses to prevent skin burns from runaway thermal reactions in batteries can occur. It also is a convenient temperature range for extracting energy in the diurnal cycle of desert climates. We thus anticipate this material and its family may have a multitude of practical applications in addition to being a capable model to study structure-function behavior in these unique materials.

RESULTS AND DISCUSSION

After our discoveries concerning butoxyphenyl-NDI crystals[46] that exhibit irreversible thermosalience and reversible thermochromism, we expanded our search to other NDI derivatives based on alkyl chain length.[210] We found that this NDI family exhibits thermosalience and thermochromism across may derivatives. Upon reaching 10 carbons (Decoxyphenyl-NDI, DNDI), we found the crystal to be reversibly thermosalient, exhibiting negative thermal expansion on heating past the phase transition point common in these derivatives. What's more, the transition temperature was around 45 °C—a temperature range well-suited for more realistic applications than other reversibly thermosalient crystals, which actuate at >80 °C[64, 67] or lower than 0 °C.[53]

DNDI was synthesized based on literature protocols, substituting longer alkyl chains. Naphthalenetetracarboxydianhydride was reacted with 4-aminophenol to create NDI-Phenol. NDI-Phenol was reacted with 1-bromodecane to create DNDI. The crude solution was passed through a silica column with chloroform and evaporated from the fraction tubes to create long single crystals. These crystals were examined with single crystal X-Ray diffraction at low and high temperatures and the fine structure was solved. The crystallographic parameters are summarized in **Table 5.1**.

Table 5.1. Crystallographic parameters at 298K and 338K.

Parameter		298 K	338 K
Crystal System		Triclinic	
Space Group		$P\bar{1}$	
Formula		$C_{46}H_{54}N_2O_6$	
M_r (g/mol)		730.91	
Unit cell (Å)	*a* =	5.232 (4)	8.775 (3)
	b =	7.643 (5)	9.070 (3)
	c =	25.120 (18)	29.218 (10)
	α =	86.887 (19)°	81.70 (2)°
	β =	87.346 (19)°	83.383 (13)°
	γ =	80.28 (2)°	63.15 (2)°
Volume (Å^3)		987.8 (12)	2049.8 (12) Å^3
Crystal Color		Yellow	
Z		1	2
Dimensions (mm)		0.32 × 0.16 × 0.10	N/A[a]
Reflections Collected		11522	33485
R_{int}		0.052	0.168
Density (g cm^{-3})[b]		1.229	1.184
μ (mm^{-1})		0.08	
$R[F^2 > 2\sigma(F^2)]$		0.069	0.120
w$R(F^2)$		0.177	0.280
Mo $K\alpha$ radiation, λ (Å)		0.71073	

[a]Crystal dimensions at 338 K were not available at the time of this report. [b]Although the unit cell volume nearly doubles, the number of units per cell (Z) also double, and the overall density decreases slightly, despite the fact that the bulk crystal decreases in volume significantly.

Single crystal X-ray diffraction analysis indicates that the molecular arrangement within the lattice positions the NDI cores parallel to each other with the alkyl chains fully extended away, forming layers of ribbon-like planes. (**Figure 5.1a and c**). Looking such that the crystal's large axis of thermal contraction is arranged horizontally, the distances between the NDI cores shorten considerably, and they pack together closer (**Figure 5.1b**).

Of primary interest in DNDI crystals, of course, is their sudden negative thermal expansion that occurs at 45 °C. Upon heating the stage past the transition point, the crystal shrinks to ~89% of its cold length in the long direction (**Figure 5.1d**). The width increases slightly and the there is no apparent change in thickness. The hot and cold lengths remain

relatively stable (**Figure 5.1e**) following multiple cycles without loss in compressibility (**Movie D1**).

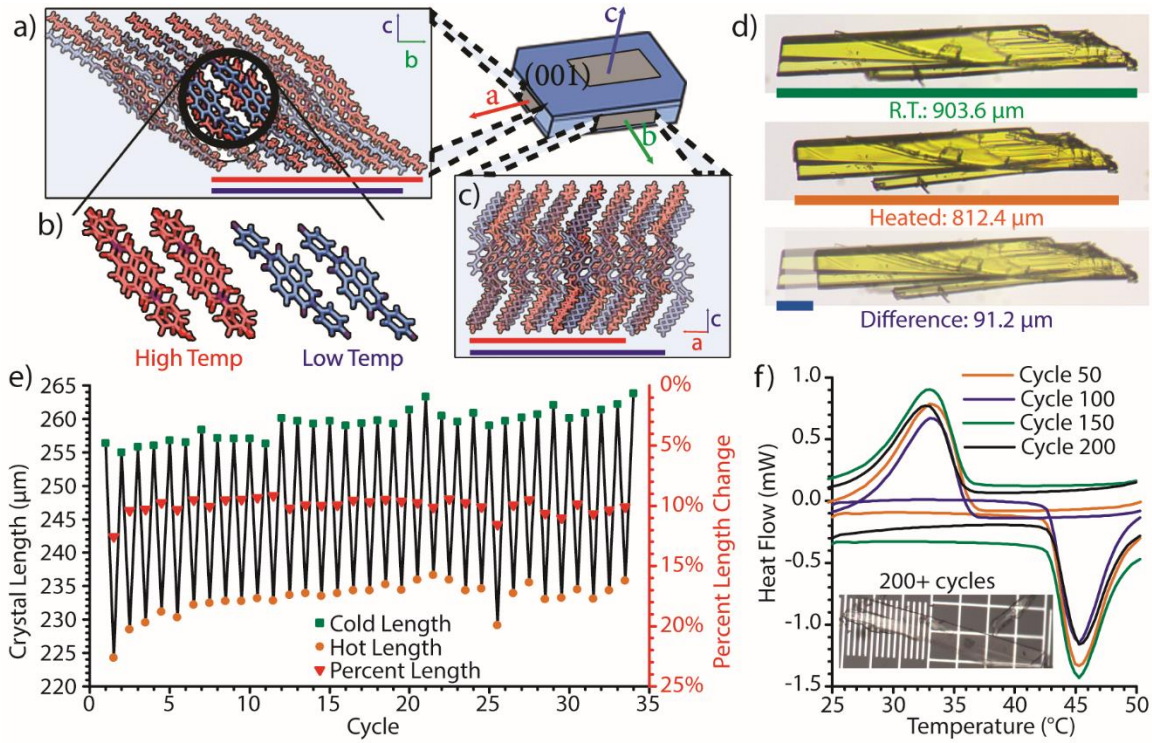

Figure 5.1. Views of molecular crystal packing looking down a) the crystallographic a axis at b) high (red) and low (blue) temperatures and c) down the crystallographic b axis, as illustrated in the bulk crystal orientation. d) Optical micrographs of DNDI crystal at room temperature (top), heated (middle) and an overlay illustrating the length difference (bottom). e) Graph showing crystal length changes of a single crystal over 34 thermal cycles from cold (green squares) to hot (orange circles) and back with percent length change (red triangles). f) DSC traces of DNDI over 200 cycles. Cycles 50, 100, 150, and 200 are shown overlaid. The inset shows a single DNDI crystal from the DSC experiment, which remains ~800 µm long, after 207 cycles. Major divisions of the scale are 100 µm.

We conducted differential scanning calorimetry on bulk DNDI crystals cycling the temperature from 20 °C to 60 °C and back for 200 cycles (**Figure 5.1f**). The exothermic and endothermic peaks show no shift in temperature, width, or height over the cycles, indicating that the bulk molecular rearrangement is not attenuated. The recovered crystals were apparently thinner, having slightly delaminated in the DSC though the recovered crystals continued to

actuate at the same temperatures with the same 10% decrease in length. One such recovered crystal is shown in the insert of **Figure 5.1f**.

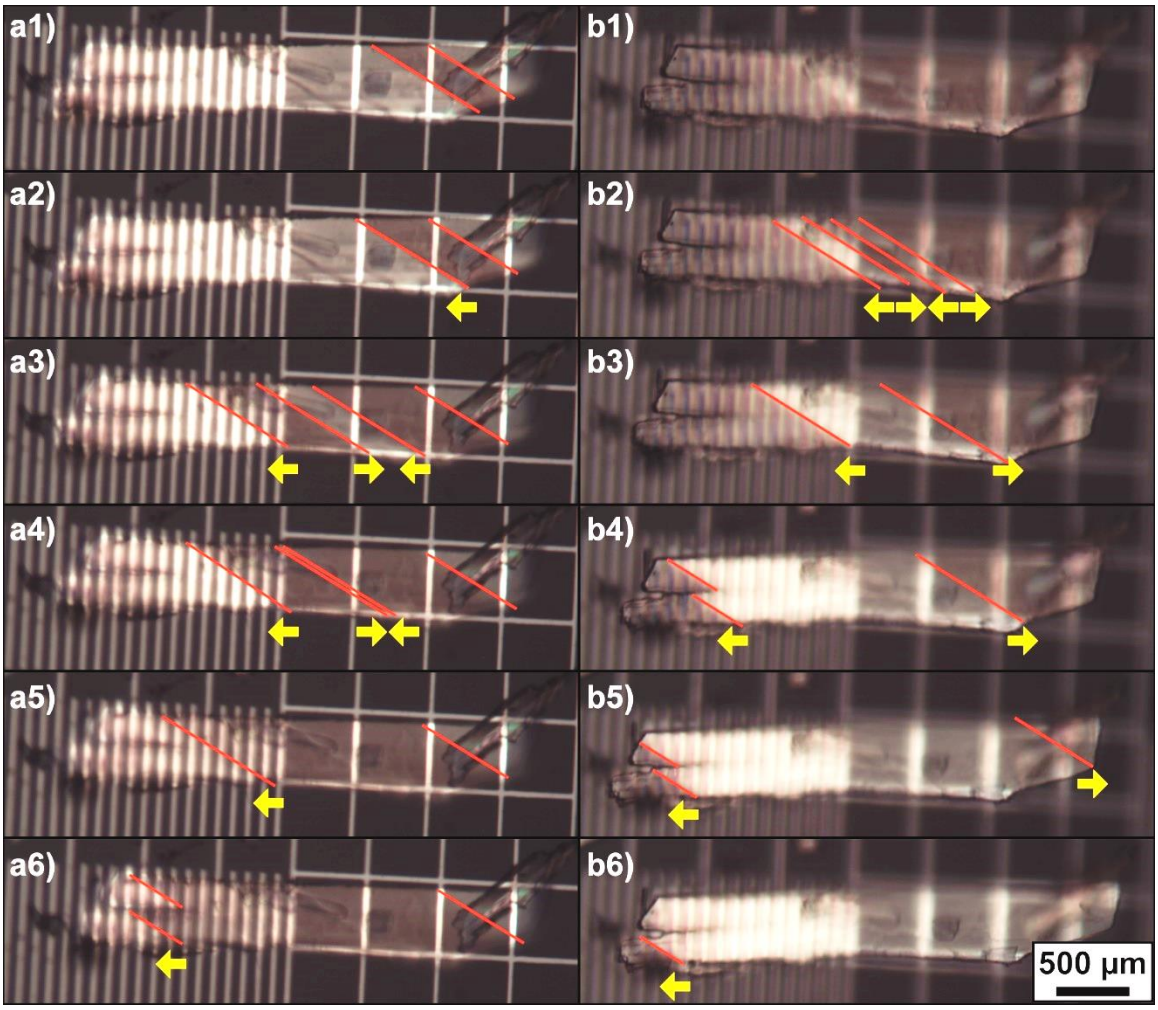

Figure 5.2. Still frames of DNDI crystal under polarized light after 200 thermal cycles subjected to a slow thermal gradient. Propagation (yellow arrows) of the molecular rearrangement wavefronts (red lines) through the long axis of the crystal upon a1-a6) heating and b1-b6) cooling past the respective thermal transition points.

The single-crystal-to-single-crystal transition occurs with a slight change in unit cell parameters, which contributes to a difference in cellular birefringence. We were able to use this change in birefringence to better understand the mechanism of actuation. During a gradual thermal gradient, the transition occurs slowly, nucleating at a certain point along the crystal long

axis while all of the molecules in a line rearrange. The "wavefront" (**Figure 5.2, red diagonal lines**) then propagates lengthwise as a solid line in either direction down the crystal (**Figure 5.2, yellow arrows**). At crystal imperfections, cracks, or dislocations, the wave front can stall, and the stress lines become apparent. The thermal gradient takes a bit longer to affect the other side of the obstacle, during which the wave front above or below the disturbance may continue propagating past, causing the crystal to split disjointly until the wave fronts catch up and the sections merge again (**Movie D2**). The most common method of crystal splitting in this manner is along the plane parallel to the large [001] face, causing delamination of the parallel sheets. Repeated thermal cycles tend to cleave or shear the crystal into thinner crystals that continue to actuate. Intriguingly, the phase transition can occur at any point in the crystal and occasionally it can occur at multiple locations. These phase transitions presumably follow a "sergeants and soldiers" propagation wherein the phase transition induces the transition nearby.

To take advantage of this thermosalience, inspiration was drawn from Khalil et al.[62] to coat the crystal in a conductive silver layer for use in an electronic circuit. DNDI exhibits no conductivity in its natural state, so a conductive coating is required to allow current to pass through. Selected large DNDI crystals were collected in a vial, 5 mL of silver nitrate, 200 mg of D-(+)-glucose, and 5 drops of ammonium hydroxide were added. The mixture was gently heated and swirled until the silver mirror appeared on the insides of the vial, then the vial was gently agitated at R.T for two days. The contents of the vial were vacuum filtered and rinsed with water then dried and examined by SEM (**Figure 5.3a**). A thin uniform coating of silver nanoparticles was found on the crystal surface and the crystals were visually grey and shiny instead of their

usual yellow (**Figure 5.3d-h**). Attempts to close a circuit with these crystals failed because the silver coating

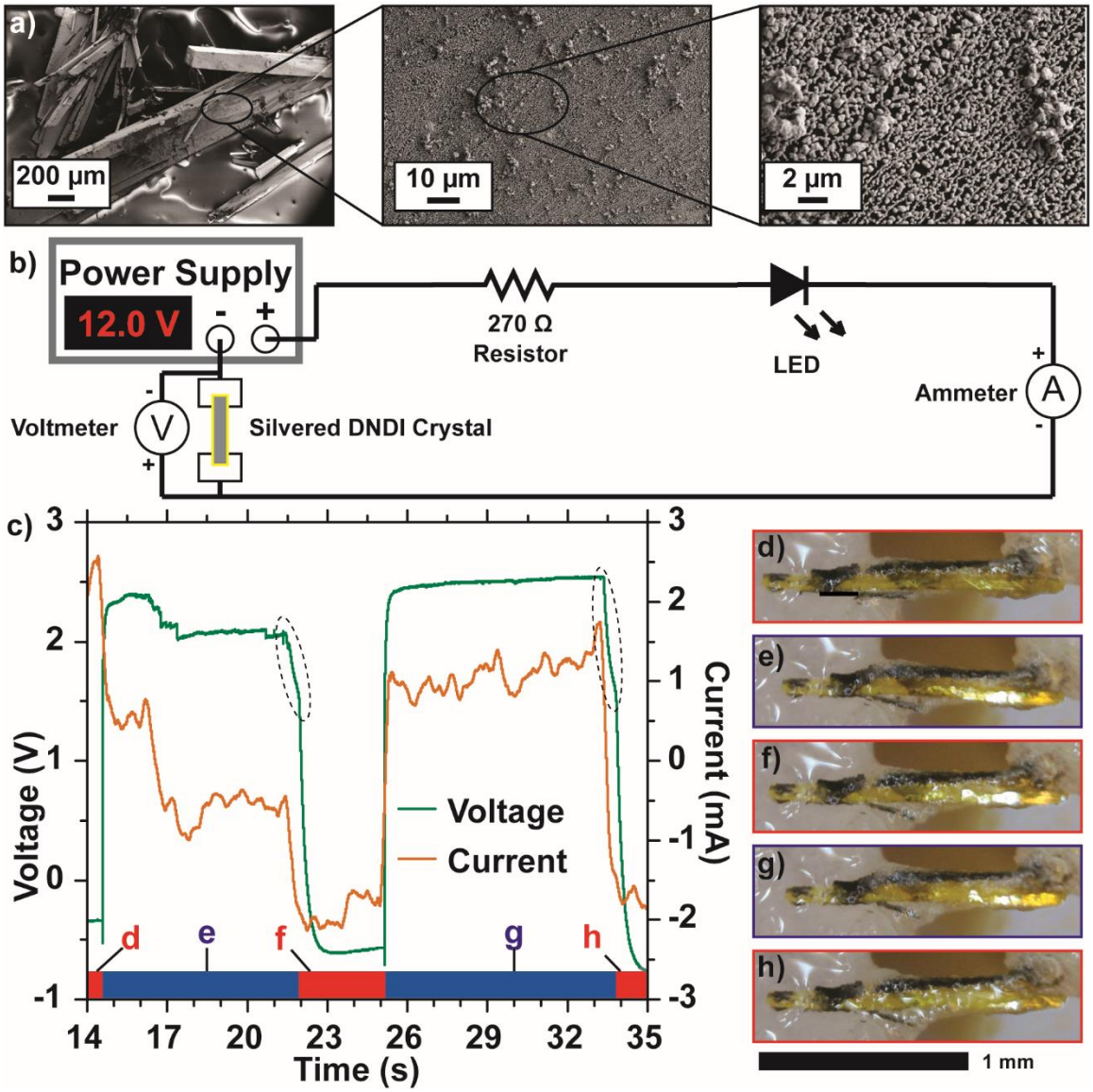

Figure 5.3. a) SEM micrographs of silvered DNDI crystals at progressively higher magnifications. At higher magnification, individual silver nanoparticles are visible. b) Circuit schematic for electrical actuation. c) Oscilloscope traces of the measured voltage and current through the circuit over time. The red sections represent the time the crystal was expanded, and the blue sections represent the time the crystal was contracted. The dotted black ellipses on the voltage trace indicate the capacitor discharge in the power supply upon turning off the voltage. d-h) Images of the silvered crystal across the electrodes at increasing time from left to right. The image border colors represent the respective section of the timeline they were taken from. The scale bars represent 1 mm.

was not thick enough, and the silver mirror reaction was redone on the same crystals. As the silver coating grew thicker, the silver particles merged into a solid sheet. The coating appeared to have a higher affinity for itself than to the crystal surface, and upon thermal transition of the crystal, the silver coating delaminated from the crystal but remained intact (**Movie D3**). These crystals successfully closed a circuit and were deemed conductive enough to proceed.

The conductive crystals were connected in an electronic circuit (**Figure 5.3b**) to bridge a gap of a width such that it is smaller than a cold crystal but larger than a hot one. Initial attempts using copper electrodes resulted in intermittent conduction at best, as there was not very good contact between the crystal and the copper electrodes. Other attempts such as clamping or direct attachment failed as well, owing to the fragile nature and small size of the crystals. Eventually, filter paper soaked in saturated sodium chloride as a liquid electrolyte solution was used. Naked DNDI crystals show no electrical conductivity whatsoever, so any electrical measurements are entirely based on the nature of the coating. Upon passing a current through the coated crystal, the silver coating visibly turned black moving from the negative to the positive end of the crystal (**Movie D4**). Once the current provided enough heat to the circuit path—either the silver coating or the liquid electrolytes—the crystal contracted.

On applying or removing the voltage, the crystal rapidly responded by contracting or expanding, respectively (**Figure 5.3c**). The measured current was very noisy, so the trace was smoothed to obtain an average curve. On turning off the power supply, the voltage drops slowly at first, then rapidly to the baseline, indicated by the dotted ellipses in **Figure 5.3c**. This is because the capacitors in the power supply are discharging briefly after turning the voltage off.

Reexpansion force measurements were obtained using a piezoelectric sensor placed against a heated crystal and measuring the voltage produced by the piezoelectric material in response to the crystal pushing into it (**Figure 5.4**). This voltage can be converted to Newtons once the physical parameters of the sensor are determined. The crystals selected were difficult to align and register any force, but the force output was plotted against the crystal length for four crystals in a range of ~1.5 to ~3.5 mm. The forces registered in a range of ~4 to ~5.5 mN in a loose inverse proportion with length. The crystals tend to break apart under any resistance to expansion, however. This suggests that the internal forces holding the [001] planes together are weaker than the outward expansion force, as the energy required to push outwards instead shears the crystal along its plane.

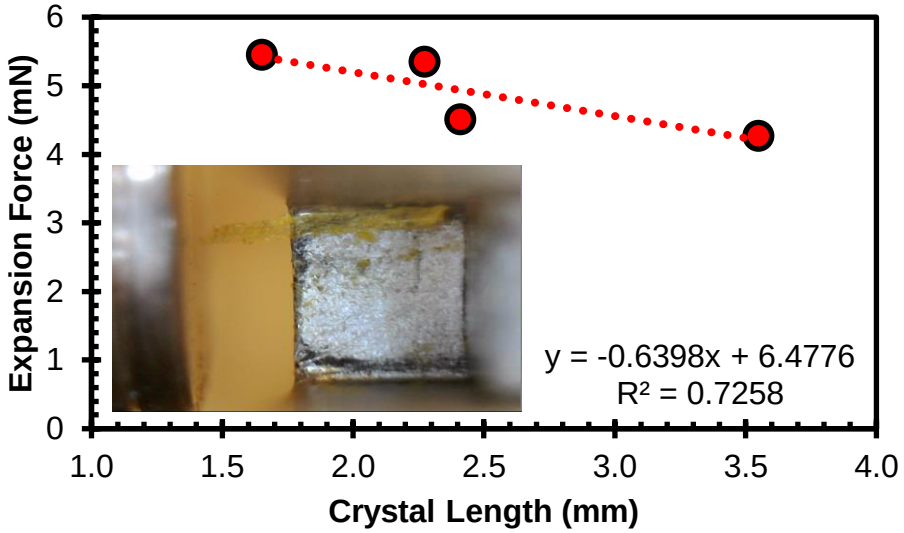

Figure 5.4. Force-length comparison of 4 DNDI crystals. The inset shows a crystal resting on the aluminum heatsink with the backstop on the right and the sensor on the left.

CONCLUSIONS

We have shown that DNDI can be used as a thermally-activated actuator for use as an electrical switch or indicator, reusable over many cycles in reasonably realistic circumstances.

These crystals retain their actuation capability even after breaking into smaller parts and show promising potential for use embedded in an elastic matrix that can align and magnify the expansive capabilities of DNDI for use as a thermal-actuated sensor, muscle, or thermomechanical servo. These crystals have potential to impact the fields of electronics and micromechanics in positive ways.

Materials, instrumentation, experimental methods, and a list of supplemental video files may be found in **Appendix D**.

CHAPTER 6

CONCLUSIONS AND FUTURE WORK

SUMMARY

This dissertation has shown two methods of controlling thermal energy: through protection of a sensitive protein systems and through driving crystallographic reversible thermosalient phase changes for doing mechanical work. In Chapter 2 and 3, methods of protecting tobacco mosaic virus in a protective ZIF-8 shell were developed and applied to proof-of-concept vaccine protection and delivery modes. In Chapter 4, a broader parameter space of general protein encapsulation in ZIF-8 was explored to investigate patterns in synthesis conditions. In Chapter 5, thermal energy was used to drive thermosalient crystal phase changes to convert concerted nano-scale molecular movement into mechanical work. These investigations and their contributions to their many fields pave the way for further development into real improvements in patient care and micromechanics.

CONCLUSIONS

The field of chemistry is very broad, and it is broadening further every day as research interests continue to overlap with adjacent fields such as biology, physics, and materials science. A continuing effort of collaboration and merging of different areas of research are required to further human understanding of reality and the universe. The joining of the fields of chemical virology and materials science have introduced novel vaccine protection platforms with promising game-changing potential in the areas of cold-chain remediation, vaccine delivery on the macro-, micro-, and nano-scales, and therapeutic protein drug effectiveness. The interface of chemistry and materials science has led to developments in single-crystal molecular actuators

that can be useful in micromachines or electronics. There are many more modes of thermal energy harnessing and protection to explore, and this work helps to lay the foundation for future developments.

FUTURE DIRECTIONS

There are several directions that could be followed from this work. More detailed studies of plant infection by encapsulated or stressed TMV to elucidate and quantify viral replication and RNA protection could be performed, as well as further in vivo murine immunogenic studies on stressed encapsulated TMV. There could be studies on dosage, administration schedules, and more complete immunogenic response assays to examine other immune factors such as cytokines and antigen-presenting cells. Correlating injection dose and frequency with overall antibody levels can provide much-needed data as a guide for other encapsulated materials. It may also reveal more parameters that are significant to establishing a desired immune response; these parameters may have been overshadowed by the dosage and frequency. Work is planned to move on from TMV as a substrate and encapsulate well-established vaccines and other proteinaceous therapeutics. The immune response of these established vaccines can be assayed more completely and reliably, allowing more focus to be placed on varying the ZIF-8 shell morphologies and exploring thermal protection and stability more completely. These efforts will go a long way towards eliminating the need for a cold chain infrastructure in delivering and storing these vaccines. Further characterization and scale-up, incorporation of future literature and experiments into the metastudy, and additional parameter exploration are planned. Further applications of DNDI, computational determination of the molecular thermal shifting mechanism, and further development of the thermodynamic NDI family are underway as well.

APPENDIX A

TEMPLATE DIRECTED SYNTHESIS OF POROUS AND PROTECTIVE CORE-SHELL BIONANOPARTICLES

MATERIALS

Glacial acetic acid, acetonitrile, aminoguanidine bicarbonate, boric acid, 2-bromoethanamine hydrobromide, 1-butanol, chloroform, cupric sulfate pentahydrate, dichloromethane (DCM), diethyl ether, 1-(3-dimethylaminopropyl)-3-ethylcarbodiimide hydrochloride (EDC), dimethyl sulfoxide (DMSO), ethylenediaminetetraacetic acid, (EDTA), fluorescein isothiocyanate (FITC), hydrochloric acid, 1-hydroxybenzotriazole hydrate (HOBt), anhydrous magnesium sulfate, *β*-mercaptoethanol, methanol, 2-methylimidazole (HMIM), 4-nitroaniline, polyethylene glycol 8000 (PEG 8000), potassium hydroxide, propargyl amine, sodium ascorbate, sodium azide, sodium chloride, sodium hydroxide, sodium nitrite, *p*-toluene sulfonic acid monohydrate, triethylamine, tris(3-hydroxypropyltriazolylmethyl)amine (THPTA), Triton X-100 surfactant, and zinc acetate dihydrate were purchased from Alfa Aesar, Acros Organics, Fisher Scientific, or Sigma Aldrich, and used as received without further purification. 18.2 MΩ DI H_2O was obtained from an ELGA PURELAB flex water purification system or a Thermo Scientific Barnstead NANOpure water purification system.

INSTRUMENTATION

Centrifuges

All microcentrifuge tubes were centrifuged using a Beckman Coulter Microfuge 16 Microcentrifuge. TMV isolation centrifugation was carried out using a Beckman Coulter Optima L-100 XP Ultracentrifuge with a Type 45 Ti rotor. Sartorius Vivaspin Turbo centrifugal

concentrators were centrifuged using a Beckman Coulter Allegra X-14R Centrifuge with a SX4750 rotor.

Electron Microscopy

Scanning electron microscopy (SEM) was conducted on a Zeiss Supra 40 Scanning Electron Microscope with an accelerating voltage of 2.5 kV. To enhance the conductivity, the sample was treated with gold sputtering method prior to microscope characterization. Transmission electron microscopy (TEM) was conducted by FEI Tecnai G2 Spirit Biotwin transmission electron microscope with an accelerating voltage of 120 kV. For TZ-thin and TZ-thick, the diluted sample suspension was directly cast on copper grid without negative staining. The purified exfoliated TZ-thick sample, which simply contains a dilute solution of TMV, was treated with negative staining using 2% uranyl acetate aqueous solution for 30 s.

Powder X-ray Diffraction (PXRD)

PXRD data for ZIF-8, TMV@ZIF-8 composites were collected using a Bruker D8 Advance powder X-ray diffractometer with CuKα (1.54060 Å) at 40 kV and 30 mA. 2θ was measured from 5° to 80° with 0.02° step size.

Thermogravimetric Analysis (TGA)

Thermal stability analysis for ZIF-8, TZ-thin and TZ-thick was conducted on a TA Instruments Q500 Thermogravimetric Analyzer under air atmosphere. The heating ramp was set as 10 °C/min from 25 to 800 °C.

N_2 Sorption Analysis

Low-pressure gas adsorption experiments of activated ZIF-8, TZ-thin and TZ-thick (up to 760 Torr) were carried out on a Micromeritics ASAP 2020 surface area analyzer. Ultrahigh-

purity-grade N_2, (obtained from Airgas Corporation) was used for all adsorption measurements. N_2 (77 K) isotherms were measured using a liquid nitrogen bath. Brunauer-Emmett-Teller (BET) surface areas were calculated using the relative pressure range 0.01-0.1 P/P_0. Pore size distributions were determined using a non-local density functional theory (NLDFT) carbon slit-pore model in the Micromeritics Software Package.

Fluorescence

Fluorescence measurements were recorded on a Synergy™ H4 Hybrid Multi-Mode Microplate Reader.

Electrospray Ionization Mass Spectrometry (ESI-MS)

Modified TMV samples were characterized by LC/ESI-MS system composed of Agilent 1100 series HPLC system followed by 4000 QTRAP mass spectrometer. HPLC was performed using reverse phase Agilent Zorbax® C18 (150 mm) column with acetonitrile:18.2 MΩ DI H_2O gradient (1 mL/min) mobile phase containing 0.1% acetic acid. Spectra obtained from Analyst software (4000 QTRAP) were deconvoluted using Peakview 2.1 software from AB SCIEX.

NanoDrop

NanoDrop UV-Vis measurements were performed on a Thermo Scientific NanoDrop 2000 Spectrophotometer.

Nuclear Magnetic Resonance Spectroscopy (NMR)

NMR spectroscopy was performed on a Bruker Ascend 500 MHz Spectrometer.

METHODS

Isolation of TMV

TMV was isolated from infected *N. Benthamiana* leaves according to a modification of a published procedure.[211] The tobacco plants were grown and infected in-house, and infected leaves were collected and stored at -80 °C until needed. 100 g of leaves were pulverized with a mortar and pestle and homogenized in an ice-cold extraction buffer (0.1 M pH 7.4 KP buffer, 0.2% (v/v) β-mercaptoethanol). The mixture was filtered through cheesecloth to remove the plant solids, and the filtrate centrifuged at 11000 ×g for 20 min at 4°C. The supernatant was filtered through cheesecloth again, and an equal volume of 1:1 chloroform/1-butanol mixture was added and stirred on ice for 30 min. The mixture was centrifuged at 4500 ×g for 10 min. The supernatant was collected, and the aqueous phase separated. To the aqueous phase was added NaCl to 0.2 M, 8% (w/w) PEG 8000, and 1% (w/w) Triton X-100 surfactant. The mixture was stirred on ice for 30 min and stored at 4 ℃ for 1 h. The solution was centrifuged at 22000 ×g for 15 min at 4 °C. The supernatant was discarded, and the pellet resuspended in 0.1 M pH 7.4 KP buffer at 4 °C overnight. The solution was carefully layered over a 40% (w/w) sucrose cushion and centrifuged at 160000 ×g for 2.5 h at 4 °C. The supernatant was discarded, and the pellet resuspended in 0.01 M pH 7.4 KP buffer overnight. The solution was portioned equally into microcentrifuge tubes and centrifuged at 15513 ×g for 15 min. The supernatant was collected as the final TMV solution. UV-vis measurements were taken with NanoDrop at 260 nm (RNA) and 280 nm (protein). A ratio of A_{260}/A_{280} around 1.26 indicates intact TMV. Using the Beer-Lambert Law with $\varepsilon = 3$ as reported,[211] the solution concentration was determined.

Synthesis of TMV@ZIF-8

Desalting Procedure for Buffer Replacement

This protocol is used on any concentration of TMV stock to remove the buffer and replace it with 18.2 MΩ DI H_2O using a GE Health Care PD midi Trap G-25 column. The column was rinsed with 4 mL 18.2 MΩ DI H_2O four times before adding 1 mL of the virus solution. The initial void volume was then discarded. Another 1.5 mL of 18.2 MΩ DI H_2O was then added to the top of the column and this volume was collected as the desalted virus solution and its concentration was re-determined by NanoDrop.

Preparation of Initial TMV@ZIF-8 Prototype

The initial prototype is denoted as TZ-P1. In a typical synthesis of TZ-P1, 41.7 µL of a 6 mg/mL desalted TMV solution (0.25 mg of TMV) was added into a microcentrifuge tube, followed by 500 µL of a 160 mM HMIM aqueous solution and 500 µL of a 40 mM $Zn(OAc)_2$ aqueous solution (HMIM:Zn= 4:1). The mixture was shaken for 20 s then set on the bench overnight. The whitish flocculates formed right after shaking. The flocculates were separated by centrifugation at 2656 ×*g* for 10 min. The product was washed by 18.2 MΩ DI H_2O twice.

Preparation of TZ-thin

In a typical synthesis, 10.4 µL of a 6 mg/mL desalted TMV solution (0.0625 mg of TMV) was added into a microcentrifuge tube, followed by 500 µL of a 400 mM HMIM aqueous solution and 500 µL of a 20 mM $Zn(OAc)_2$ aqueous solution. The mixture was shaken for 20 s then set on the bench overnight to allow full crystal growth. The whitish flocculates formed right after shaking. The flocculates were separated by centrifugation at 2656 ×*g* for 10 min. The product was washed by 18.2 MΩ DI H_2O twice.

Preparation of TZ-thick

In a typical synthesis, 18.5 µL of a 6 mg/mL desalted TMV solution (0.111 mg of TMV) was added into a 20 mL glass scintillation vial, followed by 3000 µL of a 400 mM HMIM aqueous solution and 1500 µL of a 20 mM $Zn(OAc)_2$ aqueous solution. The mixture was shaken for 20 s then set on the bench overnight. The whitish flocculates formed right after shaking. The flocculates were separated by centrifugation at 2656 ×*g* for 10 min. The product was washed by 18.2 MΩ DI H_2O twice.

General Exfoliation Procedure

The exfoliation solution was prepared by adding EDTA to 1 M to a 1 M aqueous KOH solution, adding KOH until the EDTA dissolved, and then adjusting the pH to 7.0 with HCl. The TMV@ZIF-8 suspension is centrifuged at 2656 ×*g* for 10 min and the supernatant carefully removed. 500 µL of the exfoliation solution is added, the TMV solution is vortexed for 30 s, and left to sit for 2 h. The solution is then desalted as described earlier.

Synthesis of fTMV@ZIF-8

Synthesis of 2-azidoethanamine

2-azidoethanamine was synthesized as reported in the literature.[212] A 50 mL round bottom flask was charged with 10 mL of H_2O and 1.9172 g of sodium azide. 2.0633 g of 2-bromoethanamine hydrobromide was added and the reaction stirred at 80 °C for 24 h. The reaction mixture was cooled to 0 °C in an ice bath and 10 mL of diethyl ether and 3 g of solid KOH was added. The mixture was washed 3× with diethyl ether and the combined organic phases dried with $MgSO_4$, filtered, the solvent evaporated under a stream of dry N_2, and transferred between vessels with DCM. 0.3691 g of the product was recovered as a viscous

brown liquid (43% yield). ^{1}H-NMR ($CDCl_3$, 500 MHz) δ: 3.35 (t, J = 5.55, 2H) 2.86 (t, J = 5.60, 2H) 1.53 (s, 2H). ^{13}C-NMR ($CDCl_3$, 125 MHz) δ: 54.52, 41.25.

Synthesis of fluorescein-azide

5-(3-(2-Azidoethyl)thioureido)-2-(6-hydroxy-3-oxo-3H-xanthen-9-yl)-benzoic acid [fluorescein-azide] was synthesized as reported in the literature.[213] A 25 mL round bottom flask was charged with 0.1523 g of FITC in 15 mL of methanol. 0.0738 g of 2-azidoethanamine and 500 µL of triethylamine was added, and the reaction stirred at room temperature overnight. The solvent was evaporated under vacuum and 0.0846 g of dark orange powder collected (46% yield). ^{1}H-NMR (CD_3OD, 500 MHz) δ: 7.99 (d, J = 1.95, 1H), 7.73 (dd, J = 8.15, J = 2.05, 1H), 7.21 (d, J = 8.15, 1H), 7.08 (d, J = 9.05, 2H), 6.65 (d, J = 2.20, 2H), 6.62 (dd, J = 9.08, J = 2.23, 2H), 3.84 (t, J = 5.90, 2H), 3.60 (t, J = 5.95, 2H). ^{13}C-NMR (DMSO-d6, 125 MHz) δ: 180.96, 168.62, 160.48, 152.20, 146.07, 141.31, 129.13, 127.39, 124.37, 116.90, 113.16, 109.98, 102.31, 49.44, 42.92.

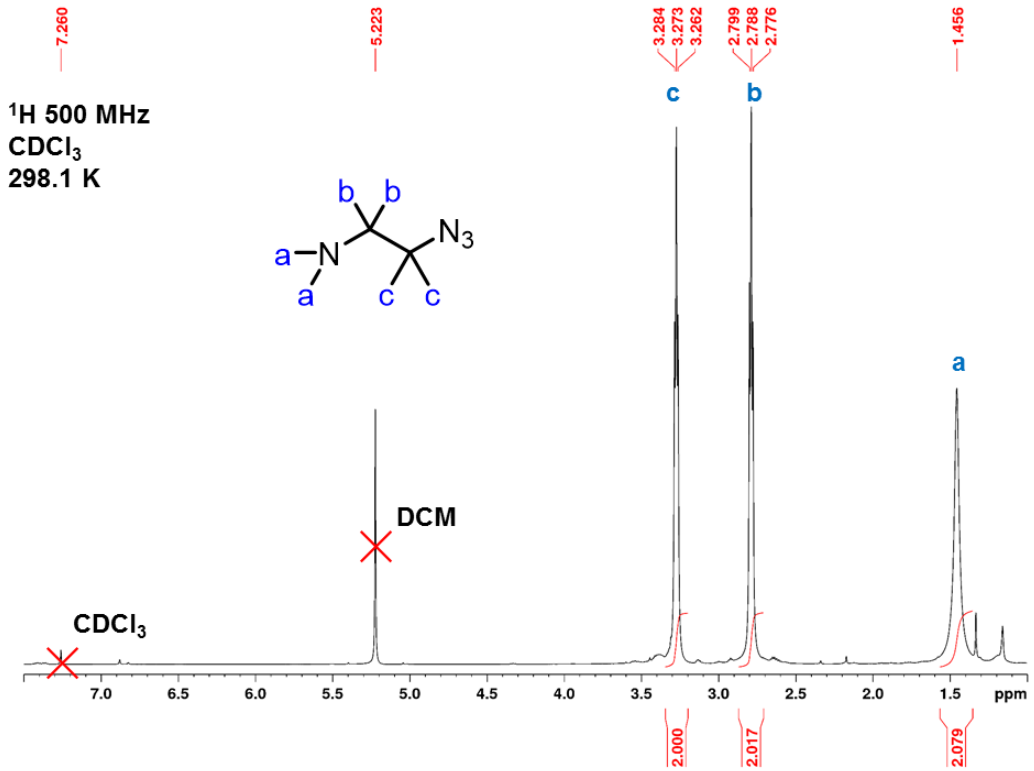

Figure A.1. ^{1}H NMR spectrum of 2-azidoethanamine in $CDCl_3$ at 500 MHz, referenced to $CDCl_3$.

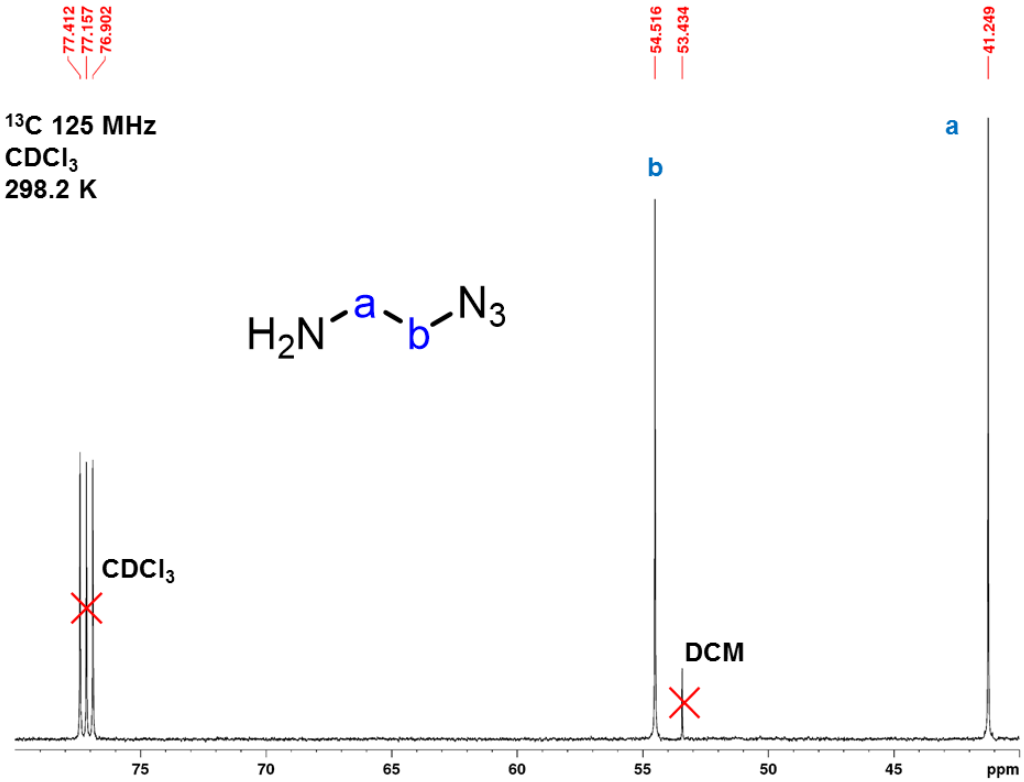

Figure A.2. ^{13}C NMR spectrum of 2-azidoethanamine in $CDCl_3$ at 125 MHz, referenced to $CDCl_3$.

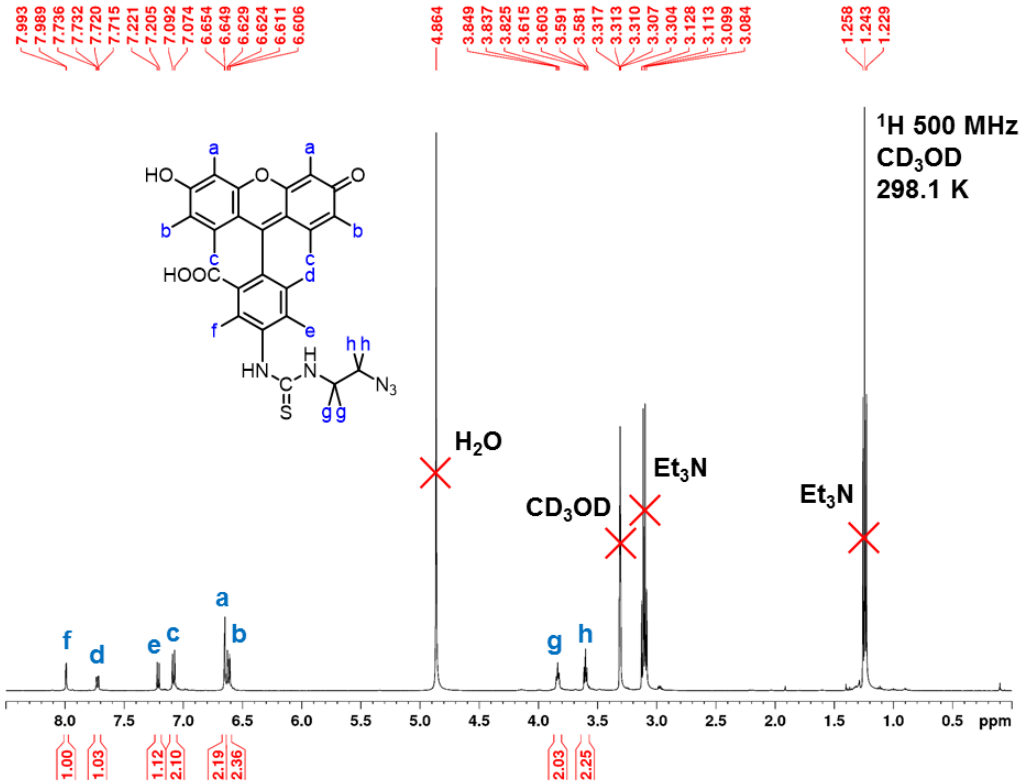

Figure A.3. ^{1}H NMR spectrum of fluorescein-azide in CD_3OD at 500 MHz, referenced to CD_3OD.

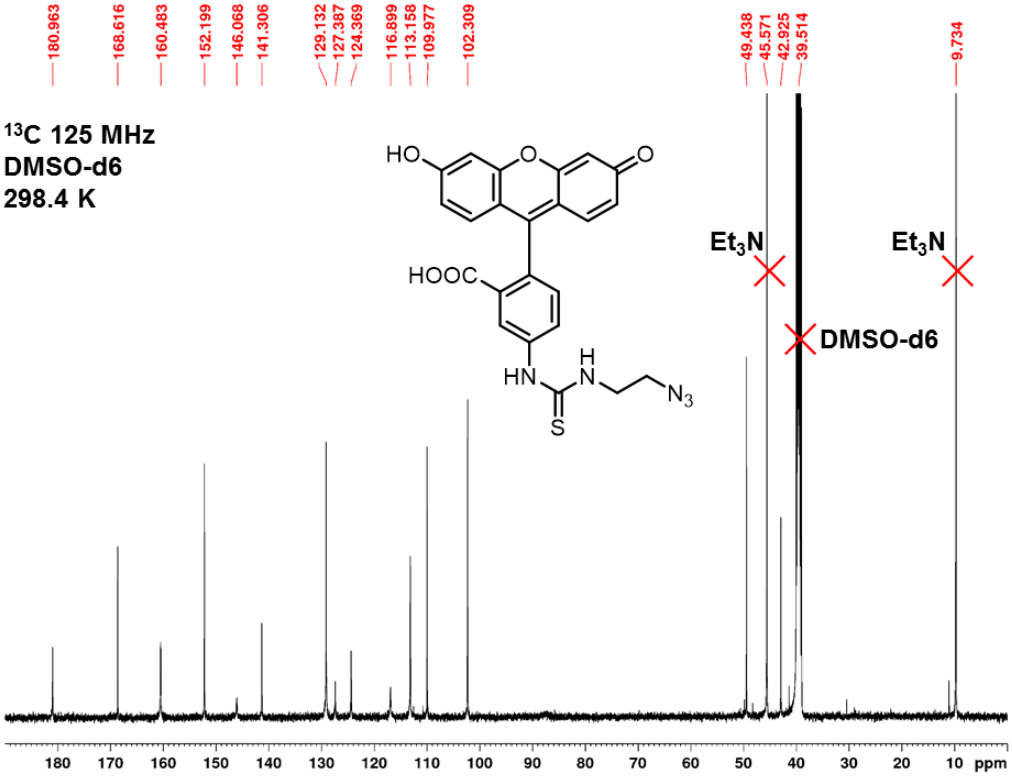

Figure A.4. ^{13}C NMR spectrum of fluorescein-azide in DMSO-d_6 at 125 MHz, referenced to DMSO-d_6.

Preparation of interior-alkyne-TMV

2 mg of TMV (391 µL of 5.12 mg/mL in 0.01 M pH 7.4 KP buffer) was diluted to 774 µL with 0.1 M pH 7.4 HEPES buffer and thoroughly mixed in a small scintillation vial. To this solution was added 130 µL of 0.1 M propargyl amine in 18.2 MΩ DI H_2O and 3.0 mg of HOBt. 32 µL of 0.1 M EDC in 18.2 MΩ DI H_2O was added at t=0 h to start the reaction, and again after t=6 h and t=18 h. The vial was mixed gently until t=24 h. The TMV solution was passed through a pre-equilibrated GE Health Care PD midi Trap G-25 column with 0.01 M pH 7.4 KP buffer.

Preparation of fTMV

Aminoguanidine bicarbonate was dissolved in conc. HCl and evaporated under vacuum to yield aminoguanidine hydrochloride. The interior-alkyne-TMV solution was concentrated in a

Sartorius Vivaspin Turbo 15 centrifugal concentrator (M.W. cutoff = 10,000 Da) and then diluted to 770 µL with 0.01 M pH 7.4 KP buffer in a small scintillation vial. 190 µL of DMSO, and 10 µL of 0.01 M fluorescein-azide in DMSO were added to the solution and vortexed for 10 s. In a separate vial, 25 mg of $CuSO_4 \cdot 5H_2O$ and 220 mg THPTA were added to 1 mL of 18.2 MΩ DI H_2O, vortexed for 10 s, and left to sit for 5 min to allow the coordination complex to form. To the TMV solution was added 10 µL of the Cu-THPTA solution, 10 µL of 0.2 M aminoguanidine hydrochloride in 18.2 MΩ DI H_2O, and lastly, 10 µL of 0.2 M sodium ascorbate in 18.2 MΩ DI H_2O (which starts the click reaction). The virus solution was gently mixed for 2 h. 10 µL of 0.5 M EDTA in 18.2 MΩ DI H_2O (buffered to pH 8.0 with NaOH pellets) was added and the solution stirred for 10 min to remove the copper. The solution was passed through a pre-equilibrated GE Health Care PD midi Trap G-25 column with 0.01 M pH 7.4 KP buffer. The eluent was concentrated in a centrifugal concentrator and concentration determined by NanoDrop to be 0.994 mg/mL.

Preparation of fTMV@ZIF-8

The fTMV@ZIF-8 was prepared by following the TZ-thin synthetic procedure.

General Protocol of Diazonium Coupling Reaction

Native TMV

Diazonium salt was prepared by mixing the following solutions at 0 °C for 1 h: 400 µL of an ice cold 0.3 M *p*-toluene sulfonic acid monohydrate solution, 75 µL of a 0.68 M 4-nitroaniline solution in acetonitrile, and 25 µL of a 3.0 M aqueous sodium nitrite solution. Next, 791 µL of 0.1 M pH 8.8 borate buffer was added to 171 µL of 11.71 mg/mL TMV solution on ice. To this mixture, 38 µL of the *in situ* formed diazonium salt (35 eq) was added and this reaction mixture

was briefly vortexed, then placed in an ice bath for 30 min. The modified TMV sample was purified by passing through a GE Health Care PD midi Trap G-25 column. To determine the reaction efficiency, TMV coat proteins were characterized by ESI-MS following a published procedure.[116] The coat proteins were isolated by adding two volumes of glacial acetic acid to the TMV solution and centrifuging at 14462 ×*g* for 10 min to remove any of the particles in the solution.

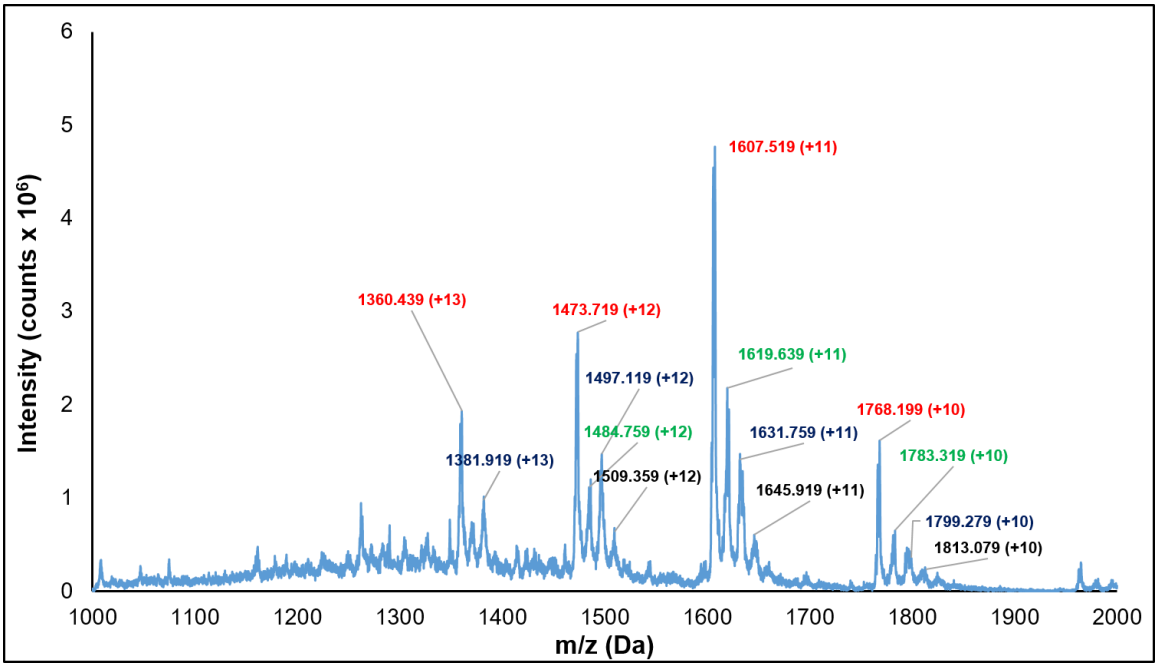

Figure A.5. Raw non-deconvoluted ESI-MS spectrum of modified native TMV; all four tyrosine residues have been modified.

TZ-thin and TZ-thick

Diazonium salt was prepared by mixing following solutions at 0 °C for 1 h: 400 µL of an ice cold 0.3 M *p*-toluene sulfonic acid monohydrate solution; 75 µL of 0.68 M 4-nitroaniline in acetonitrile; and 25 µL of 3.0 M aqueous sodium nitrite. Subsequently, TZ-thin or TZ-thick containing 1 mg of TMV was suspended in 18.2 MΩ DI H_2O. Diazonium salt (38 µL) was then added to the TMV@ZIF-8 suspension. The reaction mixture was briefly vortexed, then place in

an ice bath for 30 min. Then TZ-thin or TZ-thick composite materials were separated from the reactants by centrifugation at 2656 ×*g* for 10 min followed by thoroughly washing with 18.2 MΩ DI H_2O. Modified TZ-thin or TZ-thick was characterized using ESI-MS. The coat proteins were isolated by adding two volumes of glacial acetic acid to the TMV solution and centrifuging at 14462 ×*g* for 10 min to remove any of the particles in the solution.

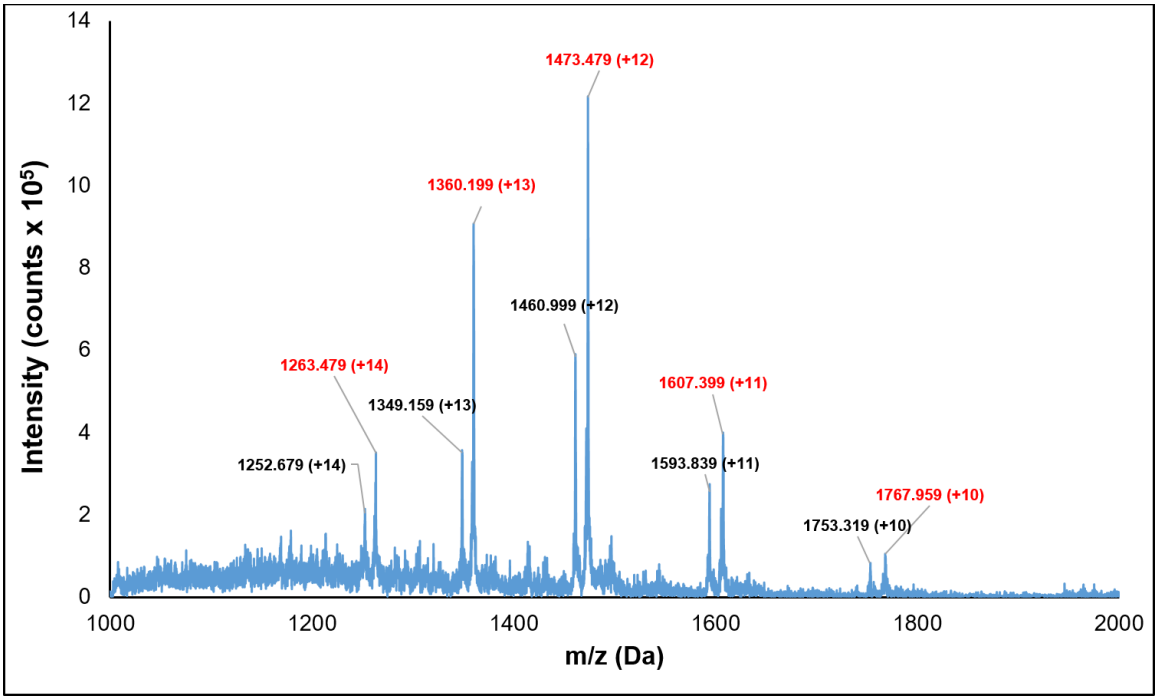

Figure A.6. Raw non-deconvoluted ESI-MS spectrum of TZ-thin rods.

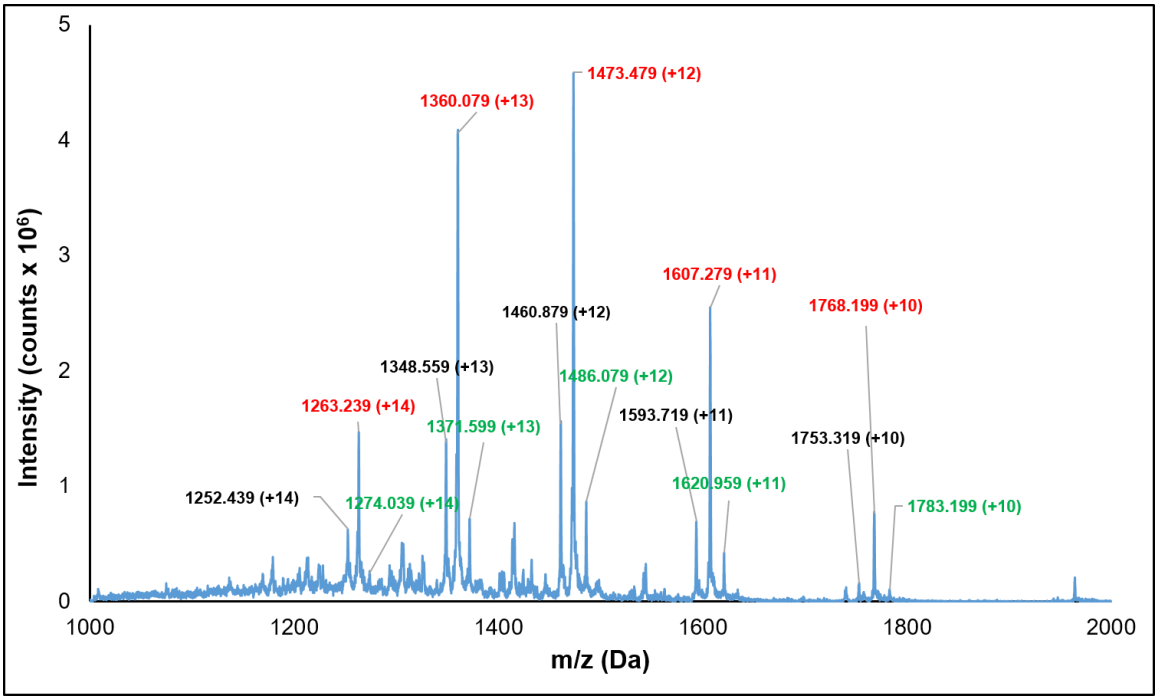

Figure A.7. Raw non-deconvoluted ESI-MS spectrum of TZ-thick rods.

6 - Study of ZIF-8 Encapsulation Efficiency and Solution Stability

Calibration Curve of fTMV

Fluorescence intensity readings were taken in a 96-well plate using 100 µL aliquots, 0.01 M pH 7.4 KP buffer as a blank, and aliquots of the base fTMV solution with dilution factors of 1×, 10×, 20×, 40×, 80×, 160×, 320×, 640×, 1280×, 2560×, and 5120× at 518 nm with excitation at 450 nm. The points were plotted and a linear best-fit line (R^2 = 0.9964) constructed to use as a calibration curve.

Fluorescence of Supernatant

The fTMV@ZIF-8 was suspended in 1 mL of 18.2 MΩ DI H_2O. Because TMV@ZIF-8 forms a stable suspension in water and does not settle out of solution, it is necessary to gently centrifuge the sample to afford a headspace to extract an aliquot of the sample. These centrifuge speeds are incapable of sedimenting non-encapsulated TMV. After centrifugation, the

sedimentation gradually returns to form a heterogeneous suspension again. Therefore, for each time point, the mixture was centrifuged at 4722 ×*g* for 10 min. 100 µL was carefully removed from the top of the supernatant, and put in a 96-well plate, with 100 µL of 18.2 MΩ DI H_2O as a blank, and fluorescence intensity recorded at 518 nm with excitation at 450 nm. The 100 µL supernatant aliquot was returned to the fTMV@ZIF-8 solution. The solution was centrifuged and a 100 µL aliquot measured and returned every hour for 10 h, and again at the 24 h time point.

Exfoliation and Recovery of Fluorescence

After the 24 h stability test, the fTMV was released by treating the sample with exfoliation solution to dissolve the ZIF-8 over 2 h. The solution was again centrifuged at 4722 ×*g* for 10 min. A 100 µL aliquot was taken from the supernatant and its fluorescence intensity was measured in a 96-well plate against 100 µL of the exfoliation solution as a blank at 518 nm with excitation at 450 nm. If the detector was saturated, 50 µL of the supernatant aliquot was transferred to another well and diluted with 50 µL of exfoliation solution and re-measured. This was repeated until the detector was not saturated. In this case, a 4× dilution was required, and the intensity value correspondingly multiplied by 4 to get the original intensity.

Stability Test for Organic Solvent Tolerance

In a microcentrifuge tube, the fresh product (TZ-thin or TZ-thick) was suspended in methanol after being properly washed with 18.2 MΩ DI H_2O and methanol. Then the product was centrifuged at 2656 ×*g* and washed with the desired organic solvent (DMF/acetonitrile/methanol/DCM) to remove water. The composite was then suspended in the organic solvent for 16 h. To confirm the integrity by SEM, an aliquot of the composite suspension (5 µL) was directly cast on a clean silicon chip and dried under ambient conditions,

except the suspension in DMF, which needed to be re-suspended in methanol to facilitate drying process.

To determine the stability of the embedded virus particles in methanol, TZ-thick was soaked in methanol for 16 h. The solution was centrifuged at 2656 ×*g* for 10 min, and the supernatant carefully removed. The solids were treated with exfoliation solution to dissolve the ZIF-8 shell. The solution was then desalted as described earlier. Later, the integrity of virus was characterized by TEM with negative staining.

Thermal Stability Test

In a microcentrifuge tube, TZ-thin or TZ-thick was suspended in 500 μL of 18.2 MΩ DI H_2O. A beaker of tap water was heated to 100 °C and allowed to boil. The microcentrifuge tubes were floated in the boiling water bath for 20 min. The sample was allowed to cool down to room temperature on the bench and 5 μL of this suspension was added directly to a clean Si chip and characterized by SEM.

APPENDIX B

ENHANCED STABILITY AND CONTROLLED DELIVERY OF MOF ENCAPSULATED VACCINES AND THEIR IMMUNOGENIC RESPONSE IN VIVO

MATERIALS

Acetic acid, acetic anhydride, acetone, bovine serum albumin, 6-bromohexanoic acid, 1-butanol, chloroform, *o*-dichlorobenzene, diethanolamine, egg albumin, ethyl acetate, 1-ethyl-3-(3-dimethylaminopropyl)carbodiimide (EDC), ethylenediamine, ethylenediaminetetraacetic acid (EDTA), guanidinium chloride, hydrazinobenzene sulfonic acid hydrates, hydrochloric acid, hydroxybenzotriazole (HOBt), 4-(2-hydroxyethyl)piperazine-1-ethanesulfonic acid (HEPES), iodomethane, magnesium chloride, malonaldehyde bis(phenylimine) monohydrochloride, β-mercatoethanol, methanol, 3-methyl-2-butanone, 2-methylimidazole, paraformaldehyde, *p*-nitrophenyl phosphate, potassium hydroxide, potassium phosphate dibasic, potassium phosphate monobasic, poly(ethylene glycol) 8000, poly(vinylpyrrolidone) 40k (PVP 40k), 2-propanol, pyridine, sodium azide, sodium bicarbonate, sodium carbonate, sodium chloride, sodium hydroxide, sodium phosphate dibasic, sodium phosphate monobasic, sodium sulfite, sucrose, Triton X-100, Tween-20, and zinc acetate dihydrate were purchased from Sigma-Aldrich (St. Louis, MO, USA), Thermo Fisher Scientific (Waltham, MA, USA), Chem-Impex Int'l (Wood Dale, IL, USA), or VWR (Radnor, PA, USA), and used without further modification.
Lowry assay was performed using a Pierce Modified Lowry assay kit (Thermo Fisher Scientific).
ELISA was performed using a TMV ELISA kit (Agdia Inc. Elkhart, IN, USA).
Rabbit antiTMV IgG and Rabbit antiTMV-alkaline phosphatase IgG were provided with the ELISA kit. Goat antimouse-alkaline phosphatase IgG was purchased from Sigma-Aldrich.

Cy5-COOH was synthesized according to a literature protocol.[182]

Ultrapure water was obtained from an ELGA PURELAB flex 2 system with resistivity measured to at least 18.2 MΩ-cm.

ELISA Buffers

ELISA buffers were prepared according to documentation provided with the TMV ELISA kit.

Coating buffer: pH 9.6 Sodium carbonate/bicarbonate with sodium azide

Wash buffer: 0.1 M pH 7.4 PBS with 0.2% Tween-20

Sample Extraction buffer: Wash buffer with PVP 40k, sodium sulfite, chicken egg albumin, and sodium azide

Conjugate buffer: Wash buffer with bovine serum albumin, PVP 40k, and sodium azide

Substrate buffer: 1 M pH 9.8 diethanolamine with magnesium chloride and sodium azide

INSTRUMENTATION

UV-Vis

UV-Vis spectra were taken using a UV-1601PC UV-Vis-NIR Spectrophotometer (Shimadzu, Kyoto, Japan), Tecan Spark 20M plate reader (Tecan, Männedorf, Switzerland), or Biotek Synergy H4 hybrid reader (Biotek, Winooski, VT, USA). NanoDrop UV-Vis measurements were performed on a Thermo Scientific NanoDrop 2000 Spectrophotometer.

Fluorescence

Fluorescence measurements were taken using a Tecan Spark 20M plate reader.

Scanning Electron Microscopy

SEM was performed on a ZEISS Supra 40 Scanning Electron Microscope (Zeiss, Oberkochen, Germany) with an accelerating voltage of 2.5 kV and a working distance of 6.7 to 15.3 mm. Samples were sputtered with a 37 Å layer of gold.

Transmission Electron Microscopy

Transmission electron micrographs were taken on a JEOL JEM-1400+ (JEOL, Tokyo, Japan) at 120 kV with a Gatan 4k × 4k CCD camera. 5 µL of the ~0.1 mg/mL desalted sample was placed on a 300 mesh Formvar/carbon-coated copper grid (Electron Microscopy Sciences, Hatfield, PA, USA), allowed to stand for 30 seconds, and wicked off with Whatman #1 filter paper. 5 µL of 2% uranyl acetate (SPI Supplies, West Chester, PA, USA) was placed on the grid, allowed to stand for 30 seconds, wicked off as before, and the grid allowed to dry completely in air.

***In vivo* Fluorescence Imager**

Fluorescent animal imaging was taken with IVIS Lumina III (PerkinElmer, Waltham, MA, USA) at an excitation of 620 nm and emission at 670 nm with a 0.5 s exposure.

METHODS

Propagation and Isolation of TMV

TMV particles were isolated from *Nicotiana benthamiana* plants from a previously published method.[20] The tobacco plants were grown, infected, and collected after 10 d of infection and stored at -80 °C until needed. Approximately 100 g of leaves were blended in pulses with 1000 mL of ice-cold extraction buffer (0.1 M pH 7.4 potassium phosphate (KP) buffer, 0.2% (v/v) β-mercaptoethanol) followed by being pulverized with a mortar and pestle.

The mixture was filtered through cheesecloth to remove the plant solids, and the filtrate centrifuged at 11,000 ×g for 20 min at 4°C. The supernatant was filtered through cheesecloth again, and an equal volume of 1:1 chloroform/1- butanol mixture was added and stirred on ice for 30 min. The mixture was centrifuged at 4500 ×g for 10 min. The aqueous phase was collected, followed by the addition of NaCl to a final concentration of 0.2 M, 8% (w/w) PEG 8000, and 1% (w/w) Triton X-100 surfactant. The mixture was stirred on ice for 30 min and stored at 4 °C for 1 h. The solution was centrifuged at 22,000 ×g for 15 min at 4 °C. The supernatant was discarded, and the pellet resuspended in 0.1 M pH 7.4 potassium phosphate (KP) buffer at 4 °C overnight. The supernatant was carefully layered on a 40% (w/v) sucrose gradient in 0.01 M KP buffer (with at least one freeze-thaw cycle) in ultraclear tubes and centrifuged in a swing bucket rotor for 2 h at 96,000 ×g. The light-scattering region was collected and centrifuged at 360,562 ×g for 1.5 h. The supernatant was discarded, and the pellet resuspended in 0.01 M pH 7.4 KP buffer overnight. The solution was portioned equally into microcentrifuge tubes and centrifuged at 15,513 ×g for 15 min. The supernatant was collected as the final TMV solution. UV-Vis measurements were taken with NanoDrop at 260 nm (RNA) and 280 nm (protein). A ratio of A_{260}/A_{280} around 1.23 indicates intact TMV. Using the Beer-Lambert Law with $\varepsilon = 3$ as reported,[20] the solution concentration was determined.

Synthesis

Cy5-COOH was synthesized according to literature protocol[214] and is reproduced below from reference [182].

Scheme B.1. Synthesis of Cy5-COOH, reproduced from reference [182].

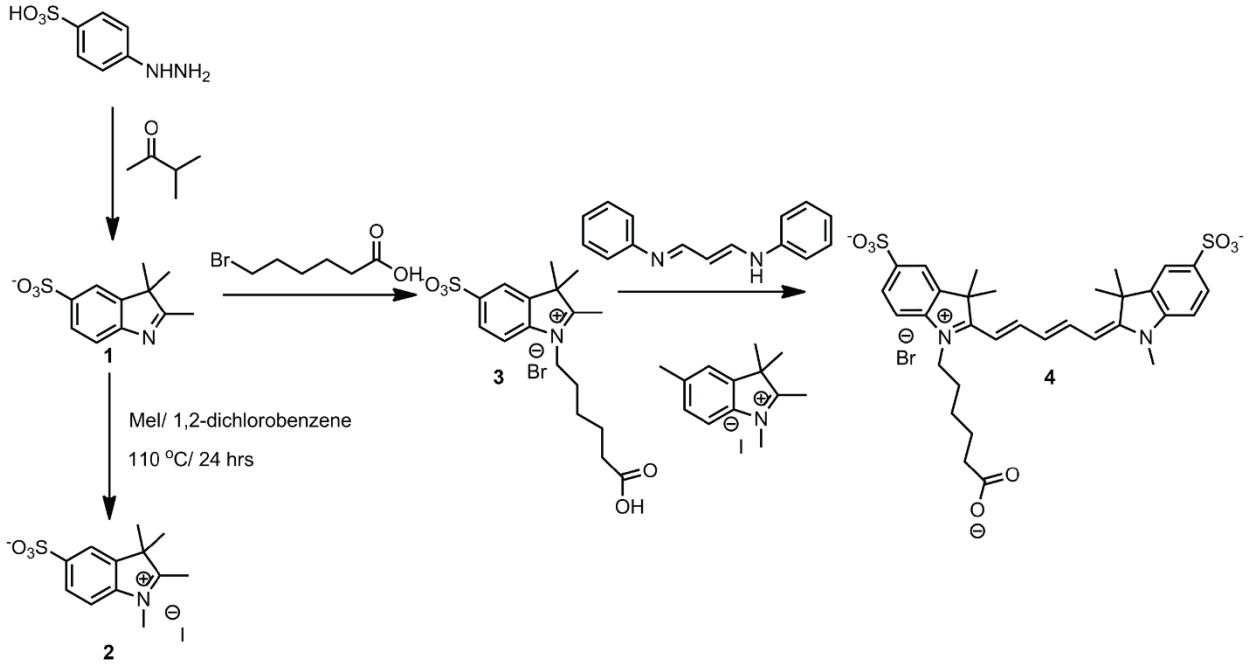

Synthesis of 3H-Indole-2,3,3-trimethyl-5-sulfonic Acid, Potassium Salt (1)

Hydrazinobenzene sulfonic acid hydrates (1.50 g, 7.60 mmol) and 3-methyl-2-butanone (2.52 mL, 23.4 mmol) were dissolved in acetic acid (4.5 mL). The mixture was heated to reflux at 110 °C for 3 h and acetic acid was removed. A solution of crude sulfonic acid in methanol (10 mL) was added dropwise to a stirred solution of potassium hydroxide (0.500 g) in 2-propanol (10 mL). The resulting mixture was stirred at 25 °C for 24 h and filtered through a paper filter. The residue was dried under reduced pressure to provide the crude compound (1.02 g, 4.49 mmol, 59.1% yield) (**1).** ^{1}H-NMR (600 MHz, D_2O) δ ppm 1.237 (s, 6H), 2.259 (s, 3H), 7.494 (d, J=8.02, 1H), 7.764 (d, J=8.09, 1H), 7.792 (s, 1H).

*Synthesis of 3H-Indolium, 1-Methyl-2,3,3-trimethyl-5-sulfonate (**2**)*

A slurry of crude **1** (0.900 g, 3.24 mmol) in iodomethane (3.5 mL, 0.20 mol) under N_2 was heated to reflux for 24 h and cooled down to 25 °C. The liquid phase was decanted, and the

residue was washed with acetone (3 × 50 mL), filtered with a paper filter, and dried under reduced pressure at 40 °C to afford the crude compound (0.440 g, 1.25 mmol, 38.7% yield) (**2**). ^{1}H-NMR (600 MHz, D_2O) δ ppm 1.522 (s, 6H), 2.153 (s, 3H), 3.971 (s, 3H), 7.777 (d, J=8.25, 1H), 7.963 (d, J=8.80, 1H), 8.026 (s, 1H).

*Synthesis of 3H-Indolium, 1-(5-Carboxypentyl)-2,3,3-trimethyl-5-sulfonate (**3**)*

3H-Indole-2,3,3-trimethyl-5-sulfonic Acid, Potassium Salt (1.02 g, 3.70 mmol) and 6-bromohexanoic acid (0.827 g 4.33 mmol) were suspended in *o*-dichlorobenzene (5 mL). The suspension was stirred at 110 °C for 19 h, then allowed to cool to room temperature, and the supernatant was removed to afford 3H-Indolium, 1-(5-Carboxypentyl)-2,3,3-trimethyl-5-sulfonate (1.10 g, 2.73 mmol, 73.80% yield) (**3**). ^{1}H-NMR (600 MHz, D_2O) δ ppm 1.378 (m, 2H), 1.586 (s, 6H), 1.601 (m, 4H), 1.904 (t, J=7.65, 2H), 2.301 (t, J=7.14, 2H), 4.433 (t, J=7.41, 2H), 7.818 (d, J=8.58, 1H), 7.945 (d, J=8.64, 1H), 7.952 (s, 1H).

*Synthesis of 3H-Indolium, 2-[5-[1-(5-Carboxypentyl)-1,3-dihydro-3,3- dimethyl-5-sulfo-2H-indol-ylidene]-1,3-pentadien-1-yl]-1-methyl-3,3-dimethyl-5-sulfonate (**4**)*

A suspension of 1-methyl-2,3,3-trimethyl-3H-indol-1-ium-5-sulfonate (**2**) (0.253 g, 1.00 mmol) and malonaldehyde bis(phenylimine) monohydrochloride (0.235 g, 1.10 mmol) in acetic acid (5 mL) and acetic anhydride (5 mL) was refluxed at 110 °C for 4 h. Solvent was removed under reduced pressure and the resultant solid was dissolved in pyridine (10 mL) under N_2. The mixture was then treated with compound (**3**) (0.353 g, 1.00 mmol) at 25 °C. Reaction mixture was stirred at 60 °C for 4 h, cooled down to 25 °C, and agitated a heterogeneous mixture by addition of ethyl acetate (10 mL). Resulting mixture was filtered through a paper filter, and the residue was dried under reduced pressure and purified with reverse flash chromatography to

yield (**4**) as a dark blue solid (0.150 g, 0.234 mmol, 23.4% yield). ^{1}H-NMR (600 MHz, D_2O) δ ppm 1.372 (m, 2H), 1.539 (m, 14H), 1.716 (p, J=4.90, 4H), 2.294 (t, J=7.50, 2H), 3.518 (s, 3H), 3.964 (m, 2H), 6.0474 (t, J=14.03, 2H), 6.376 (t, J=12.19, 1H), 7.259 (t, J=6.78, 2H), 7.741-7.779 (m, 3H), 7.871 (t, J=12.72, 2H).

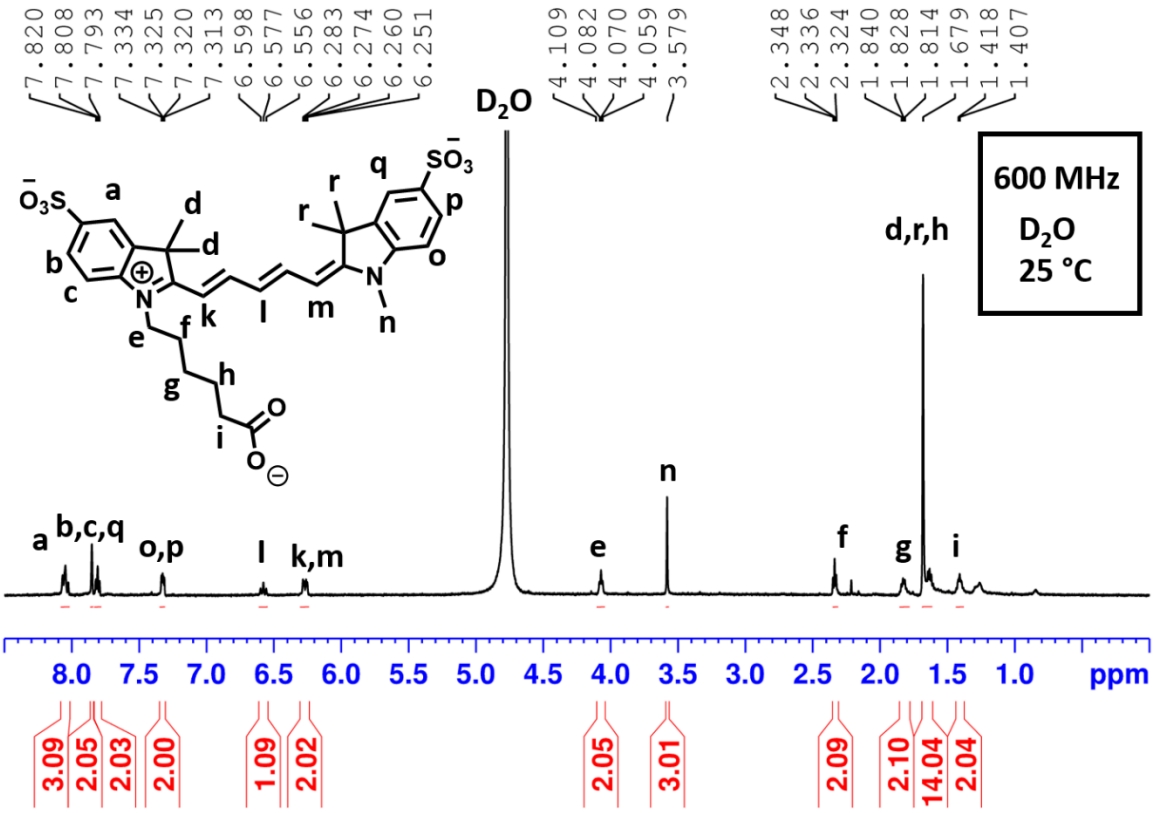

Figure B.1. ^{1}H NMR spectra of (**4**)

Preparation of TMV@ZIF composites

TMV@ZIF

TMV@ZIF was prepared according to literature protocol.[20] 0.111 mg of native TMV was added to a 20 mL scintillation vial, followed by 3 mL of 400 mM 2-methylimidazole in 3 1 mL aliquots. 3 × 500 µL aliquots of 20 mM zinc acetate dihydrate were rapidly added to the virus-ligand solution, and the vial capped and swirled for 20 sec. Flocculates appeared within the first

few seconds of zinc addition. The solution was left to incubate on the benchtop at R.T. for 16 to 18 h. The ripened solution was then transferred to a 15 mL Falcon tube and centrifuged at 4300 ×*g* for 20 min at 4 °C. The supernatant was discarded, and the pellet washed with ultrapure water twice. The final TMV@ZIF powder was then ether used as-is or dried in air.

Bioconjugation

Interior-modified Cy5-TMV was prepared according to a previously reported method.[182] The interior surface of TMV was modified with ethylenediamine (EA) using an EDC coupling reaction. 200 µL of a TMV solution (10 mg/mL) was diluted to 2 mg/mL with 574 µL of 0.1 M pH 7.4 HEPES buffer at R.T. followed by the addition of 130 µL of 0.1 M EA, 3 mg of HOBt, and 96 µL of 0.1 M EDC. The reaction mixture was incubated at R.T. for 24 h, purified with a PD MidiTrap G-25 column, and the solution was washed three times with 0.1 M KP buffer and concentrated to 10 mg/mL with a 10K MWCO Pierce™ Protein Concentrator to yield *in*EA-TMV. Cy5-COOH was then attached by the EDC reaction. 200 µL of the *in*EA-TMV solution (10 mg/mL) was diluted to 2 mg/mL with 574 µL of 0.1 M pH 7.4 HEPES buffer at R.T. followed by the addition of 130 µL of 0.1 M Cy5-COOH, 3 mg of HOBt, and 96 µL of 0.1 M EDC. The reaction mixture was incubated at R.T. for 24 h, purified with a PD MidiTrap G-25 column, and the solution was washed three times with 0.1 M KP buffer and concentrated to 10 mg/mL with a 10K MWCO Pierce™ Protein Concentrator to yield Cy5-TMV.

Cy5-TMV@ZIF

Cy5-TMV@ZIF was prepared using the same protocol as TMV@ZIF, except using Cy5-TMV instead of native TMV.

EDTA Exfoliation

Exfoliation buffer was prepared by adding EDTA to 0.1 M in a 0.1 M potassium hydroxide solution. Solid potassium hydroxide pellets were added until the EDTA was fully dissolved, then the pH adjusted to 7.0 with HCl.

TMV@ZIF composites were exfoliated by reducing the solvent level to a minimum or drying out, then adding 1 to 2 mL of EDTA Exfoliation buffer and left on a rotisserie at 37 °C. Wet samples became water-clear within the first few minutes. Resuspended dried samples became cloudy and required a longer time to clear up, up to overnight. Samples were then buffer exchanged with a 10K MWCO Pierce™ Protein Concentrator.

TMV@ZIF Stressing

Three batches of TMV@ZIF were combined and either left as is (non-stressed), soaked in 1 mL of methanol, ethyl acetate, or 6 M guanidinium chloride overnight, or heated to 100 °C in a water bath for 20 min. Naked TMV samples were stressed in the same manner, with 0.333 mg of TMV soaked in 1 mL solvent overnight, or heated to 100 °C for 20 min. Encapsulated samples were collected via centrifugation at 4300 ×g for 20 min, rinsed with ultrapure water, and exfoliated in EDTA overnight. Exfoliated and naked samples were buffer exchanged into 0.1 M pH 7.4 sodium phosphate buffer in a centrifugal filter for concentration determination by Lowry assay and then diluted to 5×10^{-4} mg/mL for ELISA measurements.

ELISA

Stressed TMV

Stressed TMV@ZIF samples were exfoliated, then both exfoliated stressed TMV@ZIF and stressed naked TMV samples were desalted with a 10K MWCO Pierce™ Protein

Concentrator and resuspended in 0.1 M pH 7.4 sodium phosphate buffer. Protein concentrations were then determined by Lowry assay before being diluted to 5×10^{-4} mg/mL for ELISA. Rabbit anti-TMV IgG in coating buffer was added 100 µL per well to a 96-well plate and incubated at R.T. for 4 h or overnight at 4 °C. The plate was emptied and washed 3× with wash buffer. Samples and standards—concentrations determined by Lowry assay—were diluted to 5×10^{-4} mg/mL with sample extraction buffer, added 100 µL per well with additional wells filled with 100 µL per well with just sample extraction buffer as the buffer blank, and incubated for 2 h at R.T. or overnight at 4 °C. The plate was emptied and washed 8× with wash buffer. Alkaline phosphatase-conjugated rabbit anti-TMV IgG in conjugate buffer was added 100 µL per well and incubated for 2 hours at R.T. The plate was emptied and washed 8× with wash buffer. 1 mg/mL *p*-nitrophenyl phosphate in substrate buffer was added 100 µL per well and the plate developed for 45 min at R.T. The plate was read at 405 nm, 420 nm, and 450 nm, and the absorbance values of buffer blank wells averaged and subtracted from the entire plate. Experiments were performed in 4 replicates and the values were normalized between that of naked non-stressed TMV (100%) and that of the buffer blank (0%).

Plant Infection

Nicotiana benthamiana plants were divided into 4 groups (n = 6 plants) and inoculated with 0.01 M pH 7.4 KP buffer as a negative control, TMV@ZIF in ultrapure water, TMV@ZIF exfoliated with EDTA and buffer exchanged into 0.01 M pH 7.4 KP buffer, and native TMV in 0.01 M pH 7.4 KP buffer as a positive control. Solutions were prepared such that 50 µL of solution delivered 5 µg of TMV, and 50 µL per leaf was used. To ensure no cross contamination each group was placed in different trays and watered and handled separately. After 10 d, the

plants were collected into separate bags and stored at -80 °C until needed. Frozen leaves were coarsely ground and approximately 1 g of recovered plant matter per group was macerated using a mortar and pestle in 10 mL of sample extraction buffer per 1 g of leaves. The plant pulp was allowed to extract overnight at 4 °C, then centrifuged to remove large plant matter, and the supernatant collected as samples for ELISA.

Mouse Serum

Rabbit anti-TMV IgG in coating buffer was added 100 µL per well to a 96-well plate and incubated at R.T. for 4 h or overnight at 4 °C. The plate was emptied and washed 3× with wash buffer. The collected plant extraction solutions were added 100 µL per well in 1×, 10×, and 50× dilutions, and incubated for 2 h at R.T. or overnight at 4 °C. The plate was emptied and washed 8× with wash buffer. Alkaline phosphatase-conjugated rabbit anti-TMV IgG in conjugate buffer was added 100 µL per well and incubated for 2 h at R.T. The plate was emptied and washed 8× with wash buffer. 1 mg/mL *p*-nitrophenyl phosphate in substrate buffer was added 100 µL per well and the plate developed for 45 min at R.T. The plate was read at 405 nm, 420 nm, and 450 nm, and the absorbance values of buffer blank wells averaged and subtracted from the entire plate. Experiments were performed in 4 replicates, a best-fit line was fit to the blank-subtracted averaged standard values, sample values were calculated from the equation, dilutions were back-calculated and averaged, and values reported as the average ± standard deviation of the apparent sample concentrations in µg/mL.

Test Mice

8 BALB/c mice were divided into two groups (n = 4) and either left uninjected or injected subcutaneously with 100 µg of native TMV in saline. Blood was drawn submandibularly after 10

d, centrifuged to remove erythrocytes, and relative antiTMV IgG levels determined by ELISA as per the above procedure. Serum was serially diluted by factors of 2 from 20× to 10240× in order to determine relative ELISA responses and optimal serum dilution levels for subsequent ELISAs.

Mouse Time Study

All mice studies were approved by the Institutional Animal Care and Use Committee at the University of Texas at Dallas (Protocol # 17-05). 12 BALB/c mice were divided into three groups (n = 4) and injected with saline, native TMV in saline, or TMV@ZIF suspended in saline. TMV solutions were prepared such that 200 µL delivered 10 µg of TMV. Doses of 200 µL of saline, TMV, or TMV@ZIF were administered subcutaneously on day 0, 2, 4, and 6 and blood was withdrawn submandibularly on day 0, 4, 7, and 35. The blood was centrifuged to remove erythrocytes, and the antiTMV IgG content of the resultant serum was determined by ELISA as described above. At the end of the study, the mice were sacrificed for histological analysis on the spleen, liver, kidney, lung, heart, and the skin at the administration site. The mice were sacrificed by carbon dioxide asphyxiation, the organs harvested, and fixed in 4% formaldehyde overnight. The fixed organs were moved to a 70% ethanol solution and processed with an ASP300 S tissue processor (Leica Biosystems, Buffalo Grove, IL) for dehydration into paraffin. The organs were then embedded into paraffin wax using a HistoCore Arcadia C and H paraffin embedding station (Leica Biosystems, Buffalo Grove, IL). Each organ was sliced into 4 µm sheets using a RM2235 manual microtome (Leica Biosystems, Buffalo Grove, IL) and imaged with a DMi1 optical microscope (Leica Biosystems, Buffalo Grove, IL) at 40× magnification.

Mouse Imaging

Ten BALB/c mice were fed a non-fluorescent diet and shaved once the mice showed no abdominal autofluorescence. The mice were anaesthetized with isoflurane and injected with 200 µL of saline (n = 4), Cy5-TMV (n = 3), or Cy5-TMV@ZIF (n = 3). The TMV-containing solutions were prepared such that 200 µL delivered 10 µg of TMV. A series of time points were taken at 1, 5, 10, and 30 min, with additional time points at 1, 2, 4, 8, 12, 18, 24, 30, 36, 48, and every 24 h thereafter until the fluorescence decayed back to the average level of the saline injected mice.

APPENDIX C

INVESTIGATION OF ZIF-8 MINERALIZATION OF PROTEINACEOUS PARTICLES

MATERIALS

2-methylimidazole and zinc acetate dihydrate were purchased from Sigma-Aldrich (St. Louis, MO, USA) and used without further modification.

TMV was isolated and prepared as described in Appendix B – Methods – TMV Isolation

Qβ for the different protein study was obtained from Arezoo Shahrivarkevishai at a concentration of 1 mg/mL in 0.1 M pH 7.4 KP buffer and used as-is.

BSA was obtained from desalted BSA standards for protein assays and concentration was determined by NanoDrop.

INSTRUMENTATION

Scanning Electron Microscopy

SEM samples were prepared and imaged according to the procedure in Appendix B – Instrumentation – Scanning Electron Microscopy.

NanoDrop

Proteinaceous sample concentrations were determined according to the procedure in Appendix B – Instrumentation – NanoDrop.

METHODS

Protein@ZIF Encapsulation

All encapsulations were carried out under general conditions. Amounts of protein and concentrations of HMIM and zinc were selected to target a specific combination of conditions in the final post-mixing solution. A small volume (<50 μL) of concentrated protein-containing

solution in appropriate buffer was added to a microcentrifuge tube. 0.5 mL of the HMIM solution was added to the protein drop and briefly mixed. 0.5 mL of the zinc acetate solution was rapidly added to the protein-HMIM solution and gently mixed for 20 s. The solution was then left undisturbed for 16-18 h at R.T. The tube was centrifuged at 6000 ×*g* for 10 min, the supernatant collected or discarded, and the pellet washed twice with water and once with ethanol and left to dry in air. Samples were collected for SEM analysis.

Preparation of TMV Coat Proteins

Solutions of TMV coat proteins (TMV CP) were prepared according to Schlick et al.[116] under the "Refolding Procedure for Internally Modified TMV Capsids" experimental section. To a solution of TMV was added two volumes of glacial acetic acid and incubated for 15 minutes. The precipitated RNA was removed from solution by centrifuging at 10000 rpm for 10 minutes in a microcentrifuge and collecting the supernatant. The supernatant was eluted through a pre-equilibrated G-25 Medium Sephadex column with 1.5 mL of 1% aqueous acetic acid. The eluent was added dropwise to 10 mL of 0.1 mL pH 7.4 potassium phosphate buffer. The solution was left at R.T. for 2 h to precipitate the coat proteins then centrifuged at 5000 rpm for 10 min. The supernatant was discarded, and the pellet dissolved in 0.1 M potassium hydroxide. The KOH solution was added to a dialysis cartridge (MWCO 3 kDa) and dialyzed at 4 °C against 0.1 M pH 8.0 Tris buffer overnight. The resulting solution was recovered and concentration examined by NanoDrop with $\varepsilon_{280} = 1.30$.[215]

APPENDIX D

REVERSIBLY THERMOSALIENT NDI CRYSTAL SWITCH

MATERIALS

1-bromodecane, silver nitrate, ammonium hydroxide, D-(+)-Glucose, potassium carbonate, 1-methyl-2-pyrrolidone (NMP), 1,4,5,8-naphthalenetetracarboxylic dianhydride, chloroform, hydrochloric acid, N,N'-dimethylformamide (DMF), 4-aminophenol, and sodium chloride were purchased from Sigma-Aldrich (St. Louis, MO, USA), or Thermo Fisher Scientific (Waltham, MA, USA) and used without further modification.

INSTRUMENTATION

Scanning Electron Microscopy

Crystals were selected for SEM and adhered to the sample holder pin with double-sided copper tape and imaged under the same conditions as in Appendix B – Instrumentation – Scanning Electron Microscopy with no gold sputtering.

Digital Scanning Calorimetry

Thermal properties of DNDI samples were analyzed with differential scanning calorimetry (DSC) using a TA Instruments Q2000. The crystals were heated from 20 °C to 60 °C then back to 20 °C for 200 cycles at a heating rate of 20 °C/min, under a flow of nitrogen (40 mL/min). The crystals were recovered from the pan afterwards for further analysis.

Electrical Measurement

Voltage was supplied with a Global Specialties 1325 (Global Specialties, Yorba Linda, CA, USA) or a Longwei Electric 302D (Longwei Electric, No.50 Tangxia Industrial Zone, Dongguan, China) power supply. Voltage measurements were recorded on a Tektronix DPO

3014 oscilloscope (Tektronix, Beaverton, OR, USA) or a Keysight 34465A multimeter (Keysight Technologies, Santa Rosa, CA, USA).

METHODS

Synthesis

NDI-Phenol

NDI-Phenol was synthesized according to a literature protocol.[210] A mixture of 1,4,5,8-naphthalenetetracarboxylic dianhydride (4.582 g, 2.119 mmol and 4-aminophenol (4.627 g, 4.240 mmol) was heated under reflux at 130 °C for 24 h. The reaction product was then collected under filtration and washed with DMF.

DNDI

DNDI was synthesized based on a literature protocol.[216] NDI-Phenol (2. 00 g, 4.4 mmol), 1-bromodecane (19.448 g, 88 mmol) and K_2CO_3 (4.8 g, 8.7 mmol) were stirred in NMP (80 mL) at 70 °C for 6 h. The reaction mixture was poured into diluted HCl, the precipitate was filtered off, and dried in vacuum. The crude product was purified by flash column in isocratic chloroform and allowed to crystallize in the fraction tubes.

Hot Stage Microscopy

A polarized optical microscope was set up with a heat gun and a cooling apparatus each pointed at the underside of the stage. The cooling apparatus consisted of a vacuum flask partially filled with water and embedded in an ice bath with an air hose delivering air to the top of the flask and another air hose delivering cooled air from the flask stem to the underside of the stage. Alternating use of the heat gun and cooling apparatus allowed a range of temperatures from approximately 5 °C to 70 °C in a reasonable cycle time of less than five minutes.

Silver mirror

Selected DNDI crystals were added to a scintillation vial and 5 mL 1 M silver nitrate and 0.2 g (D)-glucose added. 5 drops of ammonium hydroxide was added and the vial capped and gently heated while swirling until the silver mirror appeared on the inside of the vial surface. The vial was then left on a rotisserie to gently tumble for 2 days. The vial contents were vacuum filtered and rinsed with water. Silver flakes were picked out and the silvered crystals were carefully collected into a separate vial for storage. Selected silvered crystals were mounted on double-sided copper tape for examination by SEM.

Electrical Actuation

A circuit was constructed according to **Figure 5.3b**. Originally, copper tape was used for the electrodes, but the silvered DNDI crystals did not make good contact so we instead used liquid electrolyte electrodes that consisted of Whatman #1 filter paper cut into an "L" shape and moistened with a saturated NaCl solution. Two acrylic blocks were placed such that there was an air gap between the electrodes that the silvered crystal bridged, ensuring that the only electrical circuit path is across the crystal and not liquid electrolytes that have seeped away from the electrodes. During the course of the electrical measurements, the electrodes were occasionally moistened with fresh NaCl solution to maintain conductivity.

Force Measurements

A squared metal rod was machined to fit snugly between the fins of an aluminum heatsink with a setscrew to hold it down firmly in the trench to act as an adjustable backstop for expanding crystals. A thermocouple was glued into the next trench over for temperature monitoring. The heatsink assembly was clamped firmly in place and a Honeywell

FSG005WNPB force sensor (Honeywell, Golden Valley, MN, USA) was glued to an adjustable stage and clamped at the end of the backstopped trench. Selected crystals were placed in the trench such that they would re-expand against the backstop and protrude outwards from the end of the trench against the force sensor. An Opti-TekScope digital USB microscope camera (Opti-TekScope, Chandler, AZ, USA) was mounted above the assembly to monitor alignment and to record crystal lengths. A soldering iron heated to 850 °C was applied to a neighboring trench to heat the aluminum and the crystal by conduction until the thermal threshold was passed and the crystal contracted. The backstop was carefully adjusted such that the contracted crystals was butted up against it, and all of the expansion force would be applied in the opposite direction, that is, into the sensor. The assembly was cooled by placing a chunk of ice against the bottom surface of the heatsink away from the crystal until the crystal re-expanded. The sensor values were converted to Newtons according to the manufacturer's data sheet. The trench width was determined with a microscope calibration slide, and this width was then used to determine individual crystal lengths by pixel count from the microscope images.

List of associated supplementary files

Movie D1. DNDI crystal contracting and expanding in multiple cycles.

Movie D2. DNDI crystal under polarized light showing propagation of wavefronts.

Movie D3. A silvered DNDI crystal delaminating from the silver coating upon heating on a hot plate.

Movie D4. Electrical actuation of a silvered DNDI crystal across saturated NaCl electrodes upon voltage increase.

REFERENCES

1. Mallamace, F.; Corsaro, C.; Mallamace, D.; Vasi, S.; Vasi, C.; Baglioni, P.; Buldyrev, S. V.; Chen, S.-H.; Stanley, H. E., Energy landscape in protein folding and unfolding. *Proc. Natl. Acad. Sci. U. S. A.* **2016,** *113* (12), 3159-3163.

2. Carmichael, S. P.; Shell, M. S., Entropic (de) stabilization of surface-bound peptides conjugated with polymers. *J. Chem. Phys.* **2015,** *143* (24), 243103.

3. Huus, K.; Havelund, S.; Olsen, H. B.; van de Weert, M.; Frokjaer, S., Thermal Dissociation and Unfolding of Insulin. *Biochemistry* **2005,** *44* (33), 11171-11177.

4. Niedziela-Majka, A.; Kan, E.; Weissburg, P.; Mehra, U.; Sellers, S.; Sakowicz, R., High-Throughput Screening of Formulations to Optimize the Thermal Stability of a Therapeutic Monoclonal Antibody. *J. Biomol. Screening* **2014,** *20* (4), 552-559.

5. Lim, J. Y.; Kim, N. A.; Lim, D. G.; Kim, K. H.; Jeong, S. H., Effects of thermal and mechanical stress on the physical stability of human growth hormone and epidermal growth factor. *Arch. Pharmacal Res.* **2015,** *38* (8), 1488-1498.

6. Lah, J.; Prislan, I.; Kržan, B.; Salobir, M.; Francky, A.; Vesnaver, G., Erythropoietin Unfolding: Thermodynamics and Its Correlation with Structural Features. *Biochemistry* **2005,** *44* (42), 13883-13892.

7. Rincón, V.; Rodríguez-Huete, A.; López-Argüello, S.; Ibarra-Molero, B.; Sanchez-Ruiz, J. M.; Harmsen, M. M.; Mateu, M. G., Identification of the structural basis of thermal lability of a virus provides a rationale for improved vaccines. *Structure* **2014,** *22* (11), 1560-1570.

8. Schlehuber, L. D.; McFadyen, I. J.; Shu, Y.; Carignan, J.; Duprex, W. P.; Forsyth, W. R.; Ho, J. H.; Kitsos, C. M.; Lee, G. Y.; Levinson, D. A., Towards ambient temperature-stable vaccines: the identification of thermally stabilizing liquid formulations for measles virus using an innovative high-throughput infectivity assay. *Vaccine* **2011,** *29* (31), 5031-5039.

9. Krogh, A.; Hemmingsen, A. M., The destructive action of heat on insulin solutions. *Biochem. J.* **1928,** *22* (5), 1231-1238.

10. Kristensen, D.; Chen, D.; Cummings, R., Vaccine stabilization: Research, commercialization, and potential impact. *Vaccine* **2011,** *29*, 7122-7124.

11. Silvestre, C.; Duraccio, D.; Cimmino, S., Food packaging based on polymer nanomaterials. *Prog. Polym. Sci.* **2011,** *36*, 1766-1782.

12. Ashok, A.; Brison, M.; LeTallec, Y., Improving cold chain systems: Challenges and solutions. *Vaccine* **2017,** *35* (17), 2217-2223.

13. Bogataj, M.; Bogataj, L.; Vodopivec, R., Stability of perishable goods in cold logistic chains. *Int. J. Prod. Econ.* **2005,** *93-94*, 345-356.

14. Pisal, S.; Wawde, G.; Salvankar, S.; Lade, S.; Kadam, S., Vacuum foam drying for preservation of LaSota virus: effect of additives. *AAPS PharmSciTech* **2006,** *7* (3), E30-E37.

15. LeClair, D. A.; Cranston, E. D.; Lichty, B. D.; Xing, Z.; Thompson, M. R., Consecutive spray drying to produce coated dry powder vaccines suitable for oral administration. *ACS Biomater. Sci. Eng.* **2018,** *4* (5), 1669-1678.

16. Pastor, M.; Esquisabel, A.; Talavera, A.; Año, G.; Fernández, S.; Cedré, B.; Infante, J. F.; Callicó, A.; Pedraz, J. L., An approach to a cold chain free oral cholera vaccine: in vitro and in vivo characterization of Vibrio cholerae gastro-resistant microparticles. *Int. J. Pharm.* **2013,** *448*, 247-258.

17. Pelegri-O'Day, E. M.; Paluck, S. J.; Maynard, H. D., Substituted Polyesters by Thiol–Ene Modification: Rapid Diversification for Therapeutic Protein Stabilization. *J. Am. Chem. Soc.* **2017,** *139* (3), 1145-1154.

18. Wang, C.; Luan, J.; Tadepalli, S.; Liu, K.-K.; Morrissey, J. J.; Kharasch, E. D.; Naik, R. R.; Singamaneni, S., Silk-Encapsulated Plasmonic Biochips with Enhanced Thermal Stability. *ACS Appl. Mater. Interfaces* **2016,** *8* (40), 26493-26500.

19. Sridhar, B. V.; Janczy, J. R.; Hatlevik, Ø.; Wolfson, G.; Anseth, K. S.; Tibbitt, M. W., Thermal Stabilization of Biologics with Photoresponsive Hydrogels. *Biomacromolecules* **2018,** *19* (3), 740-747.

20. Li, S.; Dharmarwardana, M.; Welch, R. P.; Ren, Y.; Thompson, C. M.; Smaldone, R. A.; Gassensmith, J. J., Template-Directed Synthesis of Porous and Protective Core–Shell Bionanoparticles. *Angew. Chem., Int. Ed.* **2016,** *55* (36), 10691-10696.

21. Wang, C.; Sun, H.; Luan, J.; Jiang, Q.; Tadepalli, S.; Morrissey, J. J.; Kharasch, E. D.; Singamaneni, S., Metal–Organic Framework Encapsulation for Biospecimen Preservation. *Chem. Mater.* **2018,** *30* (4), 1291-1300.

22. Jiang, L.; Bonde Johan, S.; Ye, L., Temperature and pH Controlled Self-Assembly of a Protein–Polymer Biohybrid. *Macromol. Chem. Phys.* **2018,** *219* (7), 1700597.

23. Mukherjee, I.; Sinha, S. K.; Datta, S.; De, P., Recyclable Thermoresponsive Polymer−β-Glucosidase Conjugate with Intact Hydrolysis Activity. *Biomacromolecules* **2018,** *19* (6), 2286-2293.

24. Hu, J.; Zhao, W.; Gao, Y.; Sun, M.; Wei, Y.; Deng, H.; Gao, W., Site-specific in situ growth of a cyclized protein-polymer conjugate with improved stability and tumor retention. *Biomaterials* **2015,** *47*, 13-19.

25. Riccardi, C. M.; Cole, K. S.; Benson, K. R.; Ward, J. R.; Bassett, K. M.; Zhang, Y.; Zore, O. V.; Stromer, B.; Kasi, R. M.; Kumar, C. V., Toward "Stable-on-the-Table" Enzymes: Improving Key Properties of Catalase by Covalent Conjugation with Poly(acrylic acid). *Bioconjugate Chem.* **2014,** *25* (8), 1501-1510.

26. Zhang, Y.; Peng, X.; Zhang, H.; Watts, A. B.; Ghosh, D., Manufacturing and ambient stability of shelf freeze dried bacteriophage powder formulations. *Int. J. Pharm.* **2018,** *542* (1), 1-7.

27. Ohtake, S.; Martin, R. A.; Yee, L.; Chen, D.; Kristensen, D. D.; Lechuga-Ballesteros, D.; Truong-Le, V., Heat-stable measles vaccine produced by spray drying. *Vaccine* **2010,** *28* (5), 1275-1284.

28. Alcock, R.; Cottingham, M. G.; Rollier, C. S.; Furze, J.; De Costa, S. D.; Hanlon, M.; Spencer, A. J.; Honeycutt, J. D.; Wyllie, D. H.; Gilbert, S. C.; Bregu, M.; Hill, A. V. S., Long-Term Thermostabilization of Live Poxviral and Adenoviral Vaccine Vectors at Supraphysiological Temperatures in Carbohydrate Glass. *Sci. Transl. Med.* **2010,** *2* (19), 19ra12.

29. Kanthamneni, N.; Sharma, S.; Meenach, S. A.; Billet, B.; Zhao, J.-C.; Bachelder, E. M.; Ainslie, K. M., Enhanced stability of horseradish peroxidase encapsulated in acetalated dextran microparticles stored outside cold chain conditions. *Int. J. Pharm.* **2012,** *431*, 101-110.

30. Hariyadi, D. M.; Ma, Y.; Wang, Y.; Bostrom, T.; Malouf, J.; Turner, M. S.; Bhandari, B.; Coombes, A. G. A., The potential for production of freeze-dried oral vaccines using alginate hydrogel microspheres as protein carriers. *J. Drug Delivery Sci. Technol.* **2014,** *24* (2), 178-184.

31. Li, A. B.; Kluge, J. A.; Guziewicz, N. A.; Omenetto, F. G.; Kaplan, D. L., Silk-based stabilization of biomacromolecules. *J. Controlled Release* **2015,** *219*, 416-430.

32. Mehta, J.; Bhardwaj, N.; Bhardwaj, S. K.; Kim, K.-H.; Deep, A., Recent advances in enzyme immobilization techniques: Metal-organic frameworks as novel substrates. *Coord. Chem. Rev.* **2016,** *322*, 30-40.

33. Liang, K.; Ricco, R.; Doherty, C. M.; Styles, M. J.; Bell, S.; Kirby, N.; Mudie, S.; Haylock, D.; Hill, A. J.; Doonan, C. J.; Falcaro, P., Biomimetic mineralization of metal-organic frameworks as protective coatings for biomacromolecules. *Nat. Commun.* **2015,** *6*.

34. Li, S.; Dharmarwardana, M.; Welch, R. P.; Benjamin, C. E.; Shamir, A. M.; Nielsen, S. O.; Gassensmith, J. J., Investigation of Controlled Growth of Metal–Organic Frameworks on Anisotropic Virus Particles. *ACS Appl. Mater. Interfaces* **2018,** *10* (21), 18161-18169.

35. Cobo, I.; Li, M.; Sumerlin, B. S.; Perrier, S., Smart hybrid materials by conjugation of responsive polymers to biomacromolecules. *Nat. Mater.* **2014,** *14*, 143.

36. Pelegri-O'Day, E. M.; Maynard, H. D., Controlled Radical Polymerization as an Enabling Approach for the Next Generation of Protein–Polymer Conjugates. *Acc. Chem. Res.* **2016,** *49* (9), 1777-1785.

37. Isarov, S. A.; Pokorski, J. K., Protein ROMP: Aqueous Graft-from Ring-Opening Metathesis Polymerization. *ACS Macro Lett.* **2015,** *4* (9), 969-973.

38. Wright, T. A.; Lucius Dougherty, M.; Schmitz, B.; Burridge, K. M.; Makaroff, K.; Stewart, J. M.; Fischesser, H. D.; Shepherd, J. T.; Berberich, J. A.; Konkolewicz, D.; Page, R. C., Polymer Conjugation to Enhance Cellulase Activity and Preserve Thermal and Functional Stability. *Bioconjugate Chem.* **2017,** *28* (10), 2638-2645.

39. Lucius, M.; Falatach, R.; McGlone, C.; Makaroff, K.; Danielson, A.; Williams, C.; Nix, J. C.; Konkolewicz, D.; Page, R. C.; Berberich, J. A., Investigating the Impact of Polymer Functional Groups on the Stability and Activity of Lysozyme–Polymer Conjugates. *Biomacromolecules* **2016,** *17* (3), 1123-1134.

40. Kovaliov, M.; Allegrezza, M. L.; Richter, B.; Konkolewicz, D.; Averick, S., Synthesis of lipase polymer hybrids with retained or enhanced activity using the grafting-from strategy. *Polymer* **2018,** *137*, 338-345.

41. ControlledTemperatureChainWorkingGroup, Controlled temperature chain: strategic roadmap for priority vaccines 2017-2020. *Geneva: World Health Organization* **2017**.

42. Nguyen, P. Q.; Courchesne, N.-M. D.; Duraj-Thatte, A.; Praveschotinunt, P.; Joshi, N. S., Engineered Living Materials: Prospects and Challenges for Using Biological Systems to Direct the Assembly of Smart Materials. *Adv. Mater.* **2018,** *30* (19), 1704847.

43. Oliveira, J.; Correia, V.; Castro, H.; Martins, P.; Lanceros-Mendez, S., Polymer-based smart materials by printing technologies: Improving application and integration. *Addit. Manuf.* **2018,** *21*, 269-283.

44. Karavasili, C.; Fatouros, D. G., Smart materials: in situ gel-forming systems for nasal delivery. *Drug Discovery Today* **2016,** *21* (1), 157-166.

45. Castellón, E.; Zayat, M.; Levy, D., Sol-gel materials for electro-optical and optically active humidity-sensitive devices. *J. Sol-Gel Sci. Technol.* **2019,** *89* (1), 56-61.

46. Dharmarwardana, M.; Welch, R. P.; Kwon, S.; Nguyen, V. K.; McCandless, G. T.; Omary, M. A.; Gassensmith, J. J., Thermo-mechanically responsive crystalline organic cantilever. *Chem. Commun.* **2017,** *53* (71), 9890-9893.

47. Morimoto, M.; Irie, M., A Diarylethene Cocrystal that Converts Light into Mechanical Work. *J. Am. Chem. Soc.* **2010,** *132* (40), 14172-14178.

48. Chizhik, S.; Sidelnikov, A.; Zakharov, B.; Naumov, P.; Boldyreva, E., Quantification of photoinduced bending of dynamic molecular crystals: from macroscopic strain to kinetic constants and activation energies. *Chem. Sci.* **2018,** *9* (8), 2319-2335.

49. Zhu, J.; Kim, Y.; Lin, H.; Wang, S.; Mirkin, C. A., pH-Responsive Nanoparticle Superlattices with Tunable DNA Bonds. *J. Am. Chem. Soc.* **2018,** *140* (15), 5061-5064.

50. Ahmed, E.; Karothu, D. P.; Naumov, P., Crystal Adaptronics: Mechanically Reconfigurable Elastic and Superelastic Molecular Crystals. *Angew. Chem., Int. Ed.* **2018,** *57* (29), 8837-8846.

51. Calvo-Correas, T.; Shirole, A.; Crippa, F.; Fink, A.; Weder, C.; Corcuera, M. A.; Eceiza, A., Biocompatible thermo- and magneto-responsive shape-memory polyurethane bionanocomposites. *Mater. Sci. Eng. C* **2019,** *97*, 658-668.

52. Pan, N.; Qin, J.; Feng, P.; Li, Z.; Song, B., Color-changing smart fibrous materials for naked eye real-time monitoring of wound pH. *J. Mater. Chem. B* **2019,** *7* (16), 2626-2633.

53. Karothu, D. P.; Weston, J.; Desta, I. T.; Naumov, P., Shape-Memory and Self-Healing Effects in Mechanosalient Molecular Crystals. *J. Am. Chem. Soc.* **2016,** *138* (40), 13298-13306.

54. Zhao, S.; Zhu, R.; Fu, Y., Piezothermic Transduction of Functional Composite Materials. *ACS Appl. Mater. Interfaces* **2019,** *11* (4), 4588-4596.

55. Qu, X.; Deng, Q.; Zheng, K., Enhancement of conductance of GaAs sub-microwires under external stimuli. *J. Appl. Phys.* **2018,** *123* (9), 095107.

56. Houjou, H.; Kato, T.; Huang, H.; Suzuki, Y.; Yoshikawa, I.; Mutai, T., Re-evaluation of the tert-Butyl Method in Crystal Engineering of Salicylideneanilines by Simultaneous Observation of Photochromism and Thermochromism in Single Crystals. *Cryst. Growth Des.* **2019,** *19* (2), 1384-1390.

57. Khalil, A.; Karothu, D. P.; Naumov, P., Direct Quantification of Rapid and Efficient Single-Stroke Actuation by a Martensitic Transition in a Thermosalient Crystal. *J. Am. Chem. Soc.* **2019,** *141* (8), 3371-3375.

58. Jin, M.; Chen, Z.; Tan, X.; Shao, H.; Liu, G.; Hu, H.; Xu, J.; Yu, B.; Shen, H.; Xu, J.; Jiang, H.; Pei, Y.; Jiang, J., Charge Transport in Thermoelectric SnSe Single Crystals. *ACS Energy Lett.* **2018,** *3* (3), 689-694.

59. Naumov, P.; Chizhik, S.; Panda, M. K.; Nath, N. K.; Boldyreva, E., Mechanically Responsive Molecular Crystals. *Chem. Rev. (Washington, DC, U. S.)* **2015,** *115* (22), 12440-12490.

60. Wang, L.; Yang, Y.; Chen, Y.; Majidi, C.; Iida, F.; Askounis, E.; Pei, Q., Controllable and reversible tuning of material rigidity for robot applications. *Mater. Today* **2018,** *21* (5), 563-576.

61. Zhang, H.; Zhang, X.; Bao, C.; Li, X.; Duan, F.; Friedrich, K.; Yang, J., Skin-Inspired, Fully Autonomous Self-Warning and Self-Repairing Polymeric Material under Damaging Events. *Chem. Mater.* **2019,** *31* (7), 2611-2618.

62. Khalil, A.; Ahmed, E.; Naumov, P., Metal-coated thermosalient crystals as electrical fuses. *Chem. Commun.* **2017,** *53* (60), 8470-8473.

63. Etter, M. C.; Siedle, A. R., Solid-state rearrangement of (phenylazophenyl)palladium hexafluoroacetylacetonate. *J. Am. Chem. Soc.* **1983,** *105* (3), 641-643.

64. Alimi, L. O.; van Heerden, D. P.; Lama, P.; Smith, V. J.; Barbour, L. J., Reversible thermosalience of 4-aminobenzonitrile. *Chem. Commun.* **2018,** *54* (48), 6208-6211.

65. Sahoo, S. C.; Panda, M. K.; Nath, N. K.; Naumov, P., Biomimetic Crystalline Actuators: Structure–Kinematic Aspects of the Self-Actuation and Motility of Thermosalient Crystals. *J. Am. Chem. Soc.* **2013,** *135* (33), 12241-12251.

66. Panda, M. K.; Runčevski, T.; Husain, A.; Dinnebier, R. E.; Naumov, P., Perpetually Self-Propelling Chiral Single Crystals. *J. Am. Chem. Soc.* **2015,** *137* (5), 1895-1902.

67. Lončarić, I.; Popović, J.; Despoja, V.; Burazer, S.; Grgičević, I.; Popović, D.; Skoko, Ž., Reversible Thermosalient Effect of N′-2-Propylidene-4-hydroxybenzohydrazide Accompanied by an Immense Negative Compressibility: Structural and Theoretical Arguments Aiming toward the Elucidation of Jumping Phenomenon. *Cryst. Growth Des.* **2017,** *17* (8), 4445-4453.

68. Tamboli, M. I.; Karothu, D. P.; Shashidhar, M. S.; Gonnade, R. G.; Naumov, P., Effect of Crystal Packing on the Thermosalient Effect of the Pincer-Type Diester Naphthalene-2,3-diyl-bis(4-fluorobenzoate): A New Class II Thermosalient Solid. *Chem. – Eur. J.* **2018,** *24* (16), 4133-4139.

69. Centore, R.; Causà, M., Translating Microscopic Molecular Motion into Macroscopic Body Motion: Reversible Self-Reshaping in the Solid State Transition of an Organic Crystal. *Cryst. Growth Des.* **2018,** *18* (6), 3535-3543.

70. Chung, H.; Ruzié, C.; Geerts, Y.; Diao, Y., Hybrid Mechanism of Nucleation and Cooperative Propagation in a Single-Crystal-to-Single-Crystal Transition of a Molecular Crystal. *Cryst. Growth Des.* **2018,** *18* (8), 4245-4251.

71. Gupta, P.; Karothu, D. P.; Ahmed, E.; Naumov, P.; Nath, N. K., Thermally Twistable, Photobendable, Elastically Deformable, and Self-Healable Soft Crystals. *Angew. Chem.* **2018,** *130* (28), 8634-8638.

72. Yaghi, O. M.; O'Keeffe, M.; Ockwig, N. W.; Chae, H. K.; Eddaoudi, M.; Kim, J., Reticular synthesis and the design of new materials. *Nature* **2003,** *423* (6941), 705-714.

73. Furukawa, H.; Cordova, K. E.; O'Keeffe, M.; Yaghi, O. M., The Chemistry and Applications of Metal-Organic Frameworks. *Science* **2013,** *341* (6149).

74. Farha, O. K.; Özgür Yazaydın, A.; Eryazici, I.; Malliakas, C. D.; Hauser, B. G.; Kanatzidis, M. G.; Nguyen, S. T.; Snurr, R. Q.; Hupp, J. T., De novo synthesis of a metal–organic framework material featuring ultrahigh surface area and gas storage capacities. *Nature Chem.* **2010,** *2* (11), 944-948.

75. Li, J.-R.; Zhou, H.-C., Bridging-ligand-substitution strategy for the preparation of metal–organic polyhedra. *Nature Chem.* **2010,** *2* (10), 893-898.

76. Farha, O. K.; Eryazici, I.; Jeong, N. C.; Hauser, B. G.; Wilmer, C. E.; Sarjeant, A. A.; Snurr, R. Q.; Nguyen, S. T.; Yazaydın, A. Ö.; Hupp, J. T., Metal–Organic Framework Materials with Ultrahigh Surface Areas: Is the Sky the Limit? *J. Am. Chem. Soc.* **2012,** *134* (36), 15016-15021.

77. Farha, O. K.; Wilmer, C. E.; Eryazici, I.; Hauser, B. G.; Parilla, P. A.; O'Neill, K.; Sarjeant, A. A.; Nguyen, S. T.; Snurr, R. Q.; Hupp, J. T., Designing Higher Surface Area Metal–Organic Frameworks: Are Triple Bonds Better Than Phenyls? *J. Am. Chem. Soc.* **2012,** *134* (24), 9860-9863.

78. Marshall, R. J.; Griffin, S. L.; Wilson, C.; Forgan, R. S., Single-Crystal to Single-Crystal Mechanical Contraction of Metal–Organic Frameworks through Stereoselective Postsynthetic Bromination. *J. Am. Chem. Soc.* **2015,** *137* (30), 9527-9530.

79. Li, Q.; Zhang, W.; Miljanić, O. Š.; Sue, C.-H.; Zhao, Y.-L.; Liu, L.; Knobler, C. B.; Stoddart, J. F.; Yaghi, O. M., Docking in Metal-Organic Frameworks. *Science* **2009,** *325* (5942), 855-859.

80. Peng, Y.; Krungleviciute, V.; Eryazici, I.; Hupp, J. T.; Farha, O. K.; Yildirim, T., Methane Storage in Metal–Organic Frameworks: Current Records, Surprise Findings, and Challenges. *J. Am. Chem. Soc.* **2013,** *135* (32), 11887-11894.

81. Gándara, F.; Furukawa, H.; Lee, S.; Yaghi, O. M., High Methane Storage Capacity in Aluminum Metal–Organic Frameworks. *J. Am. Chem. Soc.* **2014,** *136* (14), 5271-5274.

82. Lu, G.; Farha, O. K.; Zhang, W.; Huo, F.; Hupp, J. T., Engineering ZIF-8 Thin Films for Hybrid MOF-Based Devices. *Adv. Mater.* **2012,** *24* (29), 3970-3974.

83. Zhang, W.; Wu, Z.-Y.; Jiang, H.-L.; Yu, S.-H., Nanowire-Directed Templating Synthesis of Metal–Organic Framework Nanofibers and Their Derived Porous Doped Carbon Nanofibers for Enhanced Electrocatalysis. *J. Am. Chem. Soc.* **2014,** *136* (41), 14385-14388.

84. Karagiaridi, O.; Lalonde, M. B.; Bury, W.; Sarjeant, A. A.; Farha, O. K.; Hupp, J. T., Opening ZIF-8: A Catalytically Active Zeolitic Imidazolate Framework of Sodalite Topology with Unsubstituted Linkers. *J. Am. Chem. Soc.* **2012,** *134* (45), 18790-18796.

85. Beyzavi, M. H.; Klet, R. C.; Tussupbayev, S.; Borycz, J.; Vermeulen, N. A.; Cramer, C. J.; Stoddart, J. F.; Hupp, J. T.; Farha, O. K., A Hafnium-Based Metal–Organic Framework as an Efficient and Multifunctional Catalyst for Facile CO2 Fixation and Regioselective and Enantioretentive Epoxide Activation. *J. Am. Chem. Soc.* **2014,** *136* (45), 15861-15864.

86. Falkowski, J. M.; Sawano, T.; Zhang, T.; Tsun, G.; Chen, Y.; Lockard, J. V.; Lin, W., Privileged Phosphine-Based Metal–Organic Frameworks for Broad-Scope Asymmetric Catalysis. *J. Am. Chem. Soc.* **2014,** *136* (14), 5213-5216.

87. Mondloch, J. E.; Katz, M. J.; Isley Iii, W. C.; Ghosh, P.; Liao, P.; Bury, W.; Wagner, G. W.; Hall, M. G.; DeCoste, J. B.; Peterson, G. W.; Snurr, R. Q.; Cramer, C. J.; Hupp, J. T.; Farha, O. K., Destruction of chemical warfare agents using metal–organic frameworks. *Nat. Mater.* **2015,** *14* (5), 512-516.

88. Lee, C. Y.; Farha, O. K.; Hong, B. J.; Sarjeant, A. A.; Nguyen, S. T.; Hupp, J. T., Light-Harvesting Metal–Organic Frameworks (MOFs): Efficient Strut-to-Strut Energy Transfer in Bodipy and Porphyrin-Based MOFs. *J. Am. Chem. Soc.* **2011,** *133* (40), 15858-15861.

89. Son, H.-J.; Jin, S.; Patwardhan, S.; Wezenberg, S. J.; Jeong, N. C.; So, M.; Wilmer, C. E.; Sarjeant, A. A.; Schatz, G. C.; Snurr, R. Q.; Farha, O. K.; Wiederrecht, G. P.; Hupp, J. T., Light-Harvesting and Ultrafast Energy Migration in Porphyrin-Based Metal–Organic Frameworks. *J. Am. Chem. Soc.* **2013,** *135* (2), 862-869.

90. Choi, K. M.; Jeong, H. M.; Park, J. H.; Zhang, Y.-B.; Kang, J. K.; Yaghi, O. M., Supercapacitors of Nanocrystalline Metal–Organic Frameworks. *ACS Nano* **2014,** *8* (7), 7451-7457.

91. He, C.; Lu, K.; Liu, D.; Lin, W., Nanoscale Metal–Organic Frameworks for the Co-Delivery of Cisplatin and Pooled siRNAs to Enhance Therapeutic Efficacy in Drug-Resistant Ovarian Cancer Cells. *J. Am. Chem. Soc.* **2014,** *136* (14), 5181-5184.

92. Liu, D.; Poon, C.; Lu, K.; He, C.; Lin, W., Self-assembled nanoscale coordination polymers with trigger release properties for effective anticancer therapy. *Nat. Commun.* **2014,** *5*.

93. Lu, K.; He, C.; Lin, W., Nanoscale Metal–Organic Framework for Highly Effective Photodynamic Therapy of Resistant Head and Neck Cancer. *J. Am. Chem. Soc.* **2014,** *136* (48), 16712-16715.

94. Sindoro, M.; Yanai, N.; Jee, A.-Y.; Granick, S., Colloidal-Sized Metal–Organic Frameworks: Synthesis and Applications. *Acc. Chem. Res.* **2014,** *47* (2), 459-469.

95. Cho, W.; Lee, H. J.; Oh, M., Growth-Controlled Formation of Porous Coordination Polymer Particles. *J. Am. Chem. Soc.* **2008,** *130* (50), 16943-16946.

96. Tsuruoka, T.; Furukawa, S.; Takashima, Y.; Yoshida, K.; Isoda, S.; Kitagawa, S., Nanoporous Nanorods Fabricated by Coordination Modulation and Oriented Attachment Growth. *Angew. Chem., Int. Ed.* **2009,** *48* (26), 4739-4743.

97. Diring, S.; Furukawa, S.; Takashima, Y.; Tsuruoka, T.; Kitagawa, S., Controlled Multiscale Synthesis of Porous Coordination Polymer in Nano/Micro Regimes. *Chem. Mater.* **2010,** *22* (16), 4531-4538.

98. Cravillon, J.; Nayuk, R.; Springer, S.; Feldhoff, A.; Huber, K.; Wiebcke, M., Controlling Zeolitic Imidazolate Framework Nano- and Microcrystal Formation: Insight into Crystal Growth by Time-Resolved In Situ Static Light Scattering. *Chem. Mater.* **2011,** *23* (8), 2130-2141.

99. Umemura, A.; Diring, S.; Furukawa, S.; Uehara, H.; Tsuruoka, T.; Kitagawa, S., Morphology Design of Porous Coordination Polymer Crystals by Coordination Modulation. *J. Am. Chem. Soc.* **2011,** *133* (39), 15506-15513.

100. He, L.; Liu, Y.; Liu, J.; Xiong, Y.; Zheng, J.; Liu, Y.; Tang, Z., Core–Shell Noble-Metal@Metal-Organic-Framework Nanoparticles with Highly Selective Sensing Property. *Angew. Chem., Int. Ed.* **2013,** *52* (13), 3741-3745.

101. Hu, P.; Zhuang, J.; Chou, L.-Y.; Lee, H. K.; Ling, X. Y.; Chuang, Y.-C.; Tsung, C.-K., Surfactant-Directed Atomic to Mesoscale Alignment: Metal Nanocrystals Encased

Individually in Single-Crystalline Porous Nanostructures. *J. Am. Chem. Soc.* **2014,** *136* (30), 10561-10564.

102. Na, K.; Choi, K. M.; Yaghi, O. M.; Somorjai, G. A., Metal Nanocrystals Embedded in Single Nanocrystals of MOFs Give Unusual Selectivity as Heterogeneous Catalysts. *Nano Lett.* **2014,** *14* (10), 5979-5983.

103. Zhang, Z.; Chen, Y.; Xu, X.; Zhang, J.; Xiang, G.; He, W.; Wang, X., Well-Defined Metal–Organic Framework Hollow Nanocages. *Angew. Chem., Int. Ed.* **2014,** *53* (2), 429-433.

104. Zhao, M.; Deng, K.; He, L.; Liu, Y.; Li, G.; Zhao, H.; Tang, Z., Core–Shell Palladium Nanoparticle@Metal–Organic Frameworks as Multifunctional Catalysts for Cascade Reactions. *J. Am. Chem. Soc.* **2014,** *136* (5), 1738-1741.

105. Zhou, J.; Wang, P.; Wang, C.; Goh, Y. T.; Fang, Z.; Messersmith, P. B.; Duan, H., Versatile Core–Shell Nanoparticle@Metal–Organic Framework Nanohybrids: Exploiting Mussel-Inspired Polydopamine for Tailored Structural Integration. *ACS Nano* **2015,** *9* (7), 6951-6960.

106. Strable, E.; Prasuhn, D. E.; Udit, A. K.; Brown, S.; Link, A. J.; Ngo, J. T.; Lander, G.; Quispe, J.; Potter, C. S.; Carragher, B.; Tirrell, D. A.; Finn, M. G., Unnatural Amino Acid Incorporation into Virus-Like Particles. *Bioconjugate Chem.* **2008,** *19* (4), 866-875.

107. Schwarz, B.; Douglas, T., Development of virus-like particles for diagnostic and prophylactic biomedical applications. *Wiley Interdiscip. Rev.: Nanomed. Nanobiotechnol.* **2015,** *7* (5), 722-735.

108. Zhao, X.; Lin, Y.; Wang, Q., Virus-based scaffolds for tissue engineering applications. *Wiley Interdiscip. Rev.: Nanomed. Nanobiotechnol.* **2015,** *7* (4), 534-547.

109. Chen, Z.; Li, N.; Chen, L.; Lee, J.; Gassensmith Jeremiah, J., Dual Functionalized Bacteriophage Qβ as a Photocaged Drug Carrier. *Small* **2016,** *12* (33), 4563-4571.

110. Chen, Z.; Li, N.; Li, S.; Dharmarwardana, M.; Schlimme, A.; Gassensmith, J. J., Viral chemistry: the chemical functionalization of viral architectures to create new technology. *Wiley Interdiscip. Rev.: Nanomed. Nanobiotechnol.* **2016,** *8* (4), 512-534.

111. Wen, A. M.; Infusino, M.; De Luca, A.; Kernan, D. L.; Czapar, A. E.; Strangi, G.; Steinmetz, N. F., Interface of Physics and Biology: Engineering Virus-Based Nanoparticles for Biophotonics. *Bioconjugate Chem.* **2015,** *26* (1), 51-62.

112. Ma, Y.-Z.; Miller, R. A.; Fleming, G. R.; Francis, M. B., Energy Transfer Dynamics in Light-Harvesting Assemblies Templated by the Tobacco Mosaic Virus Coat Protein. *J. Phys. Chem. B* **2008,** *112* (22), 6887-6892.

113. Miller, R. A.; Stephanopoulos, N.; McFarland, J. M.; Rosko, A. S.; Geissler, P. L.; Francis, M. B., Impact of Assembly State on the Defect Tolerance of TMV-Based Light Harvesting Arrays. *J. Am. Chem. Soc.* **2010,** *132* (17), 6068-6074.

114. Bruckman, M. A.; Hern, S.; Jiang, K.; Flask, C. A.; Yu, X.; Steinmetz, N. F., Tobacco mosaic virus rods and spheres as supramolecular high-relaxivity MRI contrast agents. *J. Mater. Chem. B* **2013,** *1* (10), 1482-1490.

115. Bruckman, M. A.; Randolph, L. N.; Gulati, N. M.; Stewart, P. L.; Steinmetz, N. F., Silica-coated Gd(DOTA)-loaded protein nanoparticles enable magnetic resonance imaging of macrophages. *J. Mater. Chem. B* **2015,** *3* (38), 7503-7510.

116. Schlick, T. L.; Ding, Z.; Kovacs, E. W.; Francis, M. B., Dual-Surface Modification of the Tobacco Mosaic Virus. *J. Am. Chem. Soc.* **2005,** *127* (11), 3718-3723.

117. Shenton, W.; Douglas, T.; Young, M.; Stubbs, G.; Mann, S., Inorganic–Organic Nanotube Composites from Template Mineralization of Tobacco Mosaic Virus. *Adv. Mater.* **1999,** *11* (3), 253-256.

118. Dujardin, E.; Peet, C.; Stubbs, G.; Culver, J. N.; Mann, S., Organization of Metallic Nanoparticles Using Tobacco Mosaic Virus Templates. *Nano Lett.* **2003,** *3* (3), 413-417.

119. Knez, M.; Sumser, M.; Bittner, A. M.; Wege, C.; Jeske, H.; Martin, T. P.; Kern, K., Spatially Selective Nucleation of Metal Clusters on the Tobacco Mosaic Virus. *Adv. Funct. Mater.* **2004,** *14* (2), 116-124.

120. Niu, Z.; Liu, J.; Lee, L. A.; Bruckman, M. A.; Zhao, D.; Koley, G.; Wang, Q., Biological Templated Synthesis of Water-Soluble Conductive Polymeric Nanowires. *Nano Lett.* **2007,** *7* (12), 3729-3733.

121. Royston, E.; Ghosh, A.; Kofinas, P.; Harris, M. T.; Culver, J. N., Self-Assembly of Virus-Structured High Surface Area Nanomaterials and Their Application as Battery Electrodes. *Langmuir* **2008,** *24* (3), 906-912.

122. Pomerantseva, E.; Gerasopoulos, K.; Chen, X.; Rubloff, G.; Ghodssi, R., Electrochemical performance of the nanostructured biotemplated V2O5 cathode for lithium-ion batteries. *J. Power Sources* **2012,** *206*, 282-287.

123. Park, K. S.; Ni, Z.; Côté, A. P.; Choi, J. Y.; Huang, R.; Uribe-Romo, F. J.; Chae, H. K.; O'Keeffe, M.; Yaghi, O. M., Exceptional chemical and thermal stability of zeolitic imidazolate frameworks. *Proc. Natl. Acad. Sci. U. S. A.* **2006,** *103* (27), 10186-10191.

124. Chulkaivalsucharit, P.; Wu, X.; Ge, J., Synthesis of enzyme-embedded metal-organic framework nanocrystals in reverse micelles. *RSC Adv.* **2015,** *5* (123), 101293-101296.

125. Wu, X.; Ge, J.; Yang, C.; Hou, M.; Liu, Z., Facile synthesis of multiple enzyme-containing metal-organic frameworks in a biomolecule-friendly environment. *Chem. Commun.* **2015,** *51* (69), 13408-13411.

126. Wu, X.; Yang, C.; Ge, J.; Liu, Z., Polydopamine tethered enzyme/metal-organic framework composites with high stability and reusability. *Nanoscale* **2015,** *7* (45), 18883-18886.

127. Liang, K.; Coghlan, C. J.; Bell, S. G.; Doonan, C.; Falcaro, P., Enzyme encapsulation in zeolitic imidazolate frameworks: a comparison between controlled co-precipitation and biomimetic mineralisation. *Chem. Commun.* **2016,** *52* (3), 473-476.

128. Lyu, F.; Zhang, Y.; Zare, R. N.; Ge, J.; Liu, Z., One-Pot Synthesis of Protein-Embedded Metal–Organic Frameworks with Enhanced Biological Activities. *Nano Lett.* **2014,** *14* (10), 5761-5765.

129. Shieh, F.-K.; Wang, S.-C.; Yen, C.-I.; Wu, C.-C.; Dutta, S.; Chou, L.-Y.; Morabito, J. V.; Hu, P.; Hsu, M.-H.; Wu, K. C. W.; Tsung, C.-K., Imparting Functionality to Biocatalysts via Embedding Enzymes into Nanoporous Materials by a de Novo Approach: Size-Selective Sheltering of Catalase in Metal–Organic Framework Microcrystals. *J. Am. Chem. Soc.* **2015,** *137* (13), 4276-4279.

130. The current result shows that these recrystallized particles are 200 to 300 nm in diameter, which is slightly shorter than the TMV@MOF rods that are mostly seen longer than 300 nm indicating that the virus particles are likely not encapsulated in the crystals. Further studies are underway to see if protein is incarcerated inside. We observed the morphological change of TZ-thin in DCM via SEM characterization. The micrographs indicate that within the first 40 min the rod-shape is retained; however, only polyhedral microcrystals are found after 3 h.

131. Lee, S.-Y.; Lim, J. S.; Culver, J. N.; Harris, M. T., Coagulation of tobacco mosaic virus in alcohol–water–LiCl solutions. *J. Colloid Interface Sci.* **2008,** *324* (1–2), 92-98.

132. Fairen-Jimenez, D.; Moggach, S. A.; Wharmby, M. T.; Wright, P. A.; Parsons, S.; Düren, T., Opening the Gate: Framework Flexibility in ZIF-8 Explored by Experiments and Simulations. *J. Am. Chem. Soc.* **2011,** *133* (23), 8900-8902.

133. Zhang, K.; Lively, R. P.; Zhang, C.; Chance, R. R.; Koros, W. J.; Sholl, D. S.; Nair, S., Exploring the Framework Hydrophobicity and Flexibility of ZIF-8: From Biofuel Recovery to Hydrocarbon Separations. *J. Phys. Chem. Lett.* **2013,** *4* (21), 3618-3622.

134. Zhang, L.; Hu, Z.; Jiang, J., Sorption-Induced Structural Transition of Zeolitic Imidazolate Framework-8: A Hybrid Molecular Simulation Study. *J. Am. Chem. Soc.* **2013,** *135* (9), 3722-3728.

135. Kolokolov, D. I.; Diestel, L.; Caro, J.; Freude, D.; Stepanov, A. G., Rotational and Translational Motion of Benzene in ZIF-8 Studied by 2H NMR: Estimation of Microscopic Self-Diffusivity and Its Comparison with Macroscopic Measurements. *J. Phys. Chem. C* **2014,** *118* (24), 12873-12879.

136. Tanaka, H.; Ohsaki, S.; Hiraide, S.; Yamamoto, D.; Watanabe, S.; Miyahara, M. T., Adsorption-Induced Structural Transition of ZIF-8: A Combined Experimental and Simulation Study. *J. Phys. Chem. C* **2014,** *118* (16), 8445-8454.

137. Zhang, L.; Wu, G.; Jiang, J., Adsorption and Diffusion of CO2 and CH4 in Zeolitic Imidazolate Framework-8: Effect of Structural Flexibility. *J. Phys. Chem. C* **2014,** *118* (17), 8788-8794.

138. Kolokolov, D. I.; Stepanov, A. G.; Jobic, H., Mobility of the 2-Methylimidazolate Linkers in ZIF-8 Probed by 2H NMR: Saloon Doors for the Guests. *J. Phys. Chem. C* **2015,** *119* (49), 27512-27520.

139. Bruckman, M. A.; Steinmetz, N. F., Chemical Modification of the Inner and Outer Surfaces of Tobacco Mosaic Virus (TMV). In *Virus Hybrids as Nanomaterials: Methods and Protocols*, Lin, B.; Ratna, B., Eds. Humana Press: Totowa, NJ, 2014; pp 173-185.

140. Our current hypothesis on this difference in yield is that the thick MOF shell contains better crystallinity comparing to the thin shell; thus, the thick ZIF shell possesses a higher order of periodicity of the pore structure, which could facilitate the transportation of small molecules.

141. Leader, B.; Baca, Q. J.; Golan, D. E., Protein therapeutics: a summary and pharmacological classification. *Nat. Rev. Drug Discovery* **2008,** *7* (1), 21.

142. Thirumalai, D.; Reddy, G., Are native proteins metastable? *Nature Chem.* **2011,** *3*, 910-911.

143. Welch, R. P.; Lee, H.; Luzuriaga, M. A.; Brohlin, O. R.; Gassensmith, J. J., Protein–Polymer Delivery: Chemistry from the Cold Chain to the Clinic. *Bioconjugate Chem.* **2018,** *29* (9), 2867-2883.

144. Lee, P. W.; Shukla, S.; Wallat, J. D.; Danda, C.; Steinmetz, N. F.; Maia, J.; Pokorski, J. K., Biodegradable Viral Nanoparticle/Polymer Implants Prepared via Melt-Processing. *ACS Nano* **2017,** *11* (9), 8777-8789.

145. Liu, Y.; Lee, J.; Mansfield, K. M.; Ko, J. H.; Sallam, S.; Wesdemiotis, C.; Maynard, H. D., Trehalose glycopolymer enhances both solution stability and pharmacokinetics of a therapeutic protein. *Bioconjugate Chem.* **2017,** *28* (3), 836-845.

146. Vrdoljak, A.; Allen, E. A.; Ferrara, F.; Temperton, N. J.; Crean, A. M.; Moore, A. C., Induction of broad immunity by thermostabilised vaccines incorporated in dissolvable microneedles using novel fabrication methods. *J. Controlled Release* **2016,** *225*, 192-204.

147. Doonan, C.; Ricco, R.; Liang, K.; Bradshaw, D.; Falcaro, P., Metal–organic frameworks at the biointerface: synthetic strategies and applications. *Acc. Chem. Res.* **2017,** *50* (6), 1423-1432.

148. Alsaiari, S. K.; Patil, S.; Alyami, M.; Alamoudi, K. O.; Aleisa, F. A.; Merzaban, J. S.; Li, M.; Khashab, N. M., Endosomal Escape and Delivery of CRISPR/Cas9 Genome Editing Machinery Enabled by Nanoscale Zeolitic Imidazolate Framework. *J. Am. Chem. Soc.* **2018,** *140* (1), 143-146.

149. Rosi, N. L.; Eddaoudi, M.; Kim, J.; O'Keeffe, M.; Yaghi, O. M., Advances in the chemistry of metal-organic frameworks. *CrystEngComm* **2002,** *4* (68), 401-404.

150. McGuire, C. V.; Forgan, R. S., The surface chemistry of metal–organic frameworks. *Chem. Commun.* **2015,** *51* (25), 5199-5217.

151. Banerjee, R.; Phan, A.; Wang, B.; Knobler, C.; Furukawa, H.; O'keeffe, M.; Yaghi, O. M., High-throughput synthesis of zeolitic imidazolate frameworks and application to CO2 capture. *Science* **2008,** *319* (5865), 939-943.

152. Hayashi, H.; Côté, A. P.; Furukawa, H.; O'Keeffe, M.; Yaghi, O. M., Zeolite A imidazolate frameworks. *Nat. Mater.* **2007,** *6* (7), 501-506.

153. Li, L.; Yang, L.; Wang, J.; Zhang, Z.; Yang, Q.; Yang, Y.; Ren, Q.; Bao, Z., Highly efficient separation of methane from nitrogen on a squarate-based metal-organic framework. *AIChE J.* **2018,** *64*, 3681-3689.

154. Huxley, M. T.; Burgun, A.; Ghodrati, H.; Coghlan, C. J.; Lemieux, A.; Champness, N. R.; Huang, D. M.; Doonan, C. J.; Sumby, C. J., Protecting-group-free site-selective reactions in a metal–organic framework reaction vessel. *J. Am. Chem. Soc.* **2018,** *140* (20), 6416-6425.

155. Otake, K.-i.; Cui, Y.; Buru, C. T.; Li, Z.; Hupp, J. T.; Farha, O. K., Single-Atom-Based Vanadium Oxide Catalysts Supported on Metal–Organic Frameworks: Selective Alcohol Oxidation and Structure–Activity Relationship. *J. Am. Chem. Soc.* **2018**.

156. Fan, C.; Lv, X.; Liu, F.; Feng, L.; Liu, M.; Cai, Y.; Liu, H.; Wang, J.; Yang, Y.; Wang, H., Silver Nanoclusters Encapsulated into Metal–Organic Frameworks with Enhanced Fluorescence and Specific Ion Accumulation toward the Microdot Array-Based Fluorimetric Analysis of Copper in Blood. *ACS Sens.* **2018,** *3* (2), 441-450.

157. Zhuang, J.; Kuo, C.-H.; Chou, L.-Y.; Liu, D.-Y.; Weerapana, E.; Tsung, C.-K., Optimized metal–organic-framework nanospheres for drug delivery: evaluation of small-molecule encapsulation. *ACS Nano* **2014,** *8* (3), 2812-2819.

158. Adhikari, C.; Das, A.; Chakraborty, A., Zeolitic imidazole framework (ZIF) nanospheres for easy encapsulation and controlled release of an anticancer drug doxorubicin under different external stimuli: a way toward smart drug delivery system. *Mol. Pharm.* **2015,** *12* (9), 3158-3166.

159. Zheng, H.; Zhang, Y.; Liu, L.; Wan, W.; Guo, P.; Nyström, A. M.; Zou, X., One-pot synthesis of metal–organic frameworks with encapsulated target molecules and their applications for controlled drug delivery. *J. Am. Chem. Soc.* **2016,** *138* (3), 962-968.

160. Abánades Lázaro, I.; Haddad, S.; Rodrigo-Muñoz, J. M.; Marshall, R. J.; Sastre, B.; del Pozo, V.; Fairen-Jimenez, D.; Forgan, R. S., Surface-Functionalization of Zr-Fumarate MOF for Selective Cytotoxicity and Immune System Compatibility in Nanoscale Drug Delivery. *ACS Appl. Mater. Interfaces* **2018,** *10* (37), 31146-31157.

161. Majewski, M. B.; Howarth, A. J.; Li, P.; Wasielewski, M. R.; Hupp, J. T.; Farha, O. K., Enzyme encapsulation in metal–organic frameworks for applications in catalysis. *CrystEngComm* **2017,** *19* (29), 4082-4091.

162. Riccò, R.; Liang, W.; Li, S.; Gassensmith, J. J.; Caruso, F.; Doonan, C.; Falcaro, P., Metal–Organic Frameworks for Cell and Virus Biology: A Perspective. *ACS Nano* **2018,** *12* (1), 13-23.

163. Nadar, S. S.; Rathod, V. K., Encapsulation of lipase within metal-organics framework (MOF) with enhanced activity intensified under ultrasound. *Enzyme Microb. Technol.* **2018,** *108*, 11-20.

164. Li, P.; Moon, S.-Y.; Guelta, M. A.; Harvey, S. P.; Hupp, J. T.; Farha, O. K., Encapsulation of a nerve agent detoxifying enzyme by a mesoporous zirconium metal–organic framework engenders thermal and long-term stability. *J. Am. Chem. Soc.* **2016,** *138* (26), 8052-8055.

165. Hoop, M.; Walde, C. F.; Riccò, R.; Mushtaq, F.; Terzopoulou, A.; Chen, X.-Z.; demello, A. J.; Doonan, C. J.; Falcaro, P.; Nelson, B. J.; Puigmartí-Luis, J.; Pané, S., Biocompatibility characteristics of the metal organic framework ZIF-8 for therapeutical applications. *Appl. Mater. Today* **2018,** *11*, 13-21.

166. Maddigan, N. K.; Tarzia, A.; Huang, D. M.; Sumby, C. J.; Bell, S. G.; Falcaro, P.; Doonan, C. J., Protein surface functionalisation as a general strategy for facilitating biomimetic mineralisation of ZIF-8. *Chem. Sci.* **2018,** *9* (18), 4217-4223.

167. Liao, F.-S.; Lo, W.-S.; Hsu, Y.-S.; Wu, C.-C.; Wang, S.-C.; Shieh, F.-K.; Morabito, J. V.; Chou, L.-Y.; Wu, K. C. W.; Tsung, C.-K., Shielding against Unfolding by Embedding Enzymes in Metal–Organic Frameworks via a de Novo Approach. *J. Am. Chem. Soc.* **2017,** *139* (19), 6530-6533.

168. Duan, Y.; Ye, F.; Huang, Y.; Qin, Y.; He, C.; Zhao, S., One-pot synthesis of a metal–organic framework-based drug carrier for intelligent glucose-responsive insulin delivery. *Chem. Commun.* **2018,** *54* (42), 5377-5380.

169. Zhu, Q.; Zhuang, W.; Chen, Y.; Wang, Z.; Villacorta Hernandez, B.; Wu, J.; Yang, P.; Liu, D.; Zhu, C.; Ying, H.; Zhu, Z., Nano-Biocatalysts of Cyt c@ZIF-8/GO Composites with High Recyclability via a de Novo Approach. *ACS Appl. Mater. Interfaces* **2018,** *10* (18), 16066-16076.

170. Deng, H.; Grunder, S.; Cordova, K. E.; Valente, C.; Furukawa, H.; Hmadeh, M.; Gándara, F.; Whalley, A. C.; Liu, Z.; Asahina, S., Large-pore apertures in a series of metal-organic frameworks. *Science* **2012,** *336* (6084), 1018-1023.

171. Chen, Y.; Li, P.; Modica, J. A.; Drout, R. J.; Farha, O. K., Acid-Resistant Mesoporous Metal–Organic Framework toward Oral Insulin Delivery: Protein Encapsulation, Protection, and Release. *J. Am. Chem. Soc.* **2018,** *140* (17), 5678-5681.

172. Li, P.; Modica, J. A.; Howarth, A. J.; Vargas, E.; Moghadam, P. Z.; Snurr, R. Q.; Mrksich, M.; Hupp, J. T.; Farha, O. K., Toward design rules for enzyme immobilization in hierarchical mesoporous metal-organic frameworks. *Chem* **2016,** *1* (1), 154-169.

173. Zhang, Y.; Wang, F.; Ju, E.; Liu, Z.; Chen, Z.; Ren, J.; Qu, X., Metal-Organic-Framework-Based Vaccine Platforms for Enhanced Systemic Immune and Memory Response. *Adv. Funct. Mater.* **2016,** *26* (35), 6454-6461.

174. Xu, A.-W.; Ma, Y.; Cölfen, H., Biomimetic mineralization. *J. Mater. Chem.* **2007,** *17* (5), 415-449.

175. Xu, M.; Zhu, J.; Wang, F.; Xiong, Y.; Wu, Y.; Wang, Q.; Weng, J.; Zhang, Z.; Chen, W.; Liu, S., Improved In Vitro and In Vivo Biocompatibility of Graphene Oxide through Surface Modification: Poly(Acrylic Acid)-Functionalization is Superior to PEGylation. *ACS Nano* **2016,** *10* (3), 3267-3281.

176. Maurer, P.; Jennings, G. T.; Willers, J.; Rohner, F.; Lindman, Y.; Roubicek, K.; Renner, W. A.; Müller, P.; Bachmann, M. F., A therapeutic vaccine for nicotine dependence: preclinical efficacy, and phase I safety and immunogenicity. *Eur. J. Immunol.* **2005,** *35* (7), 2031-2040.

177. Stephanopoulos, N.; Francis, M. B., Choosing an effective protein bioconjugation strategy. *Nat. Chem. Biol.* **2011,** *7*, 876-884.

178. Rybicki, E. P., Plant-based vaccines against viruses. *Virol. J.* **2014,** *11* (1), 205.

179. Banik, S.; Mansour, A. A.; Suresh, R. V.; Wykoff-Clary, S.; Malik, M.; McCormick, A. A.; Bakshi, C. S., Development of a multivalent subunit vaccine against tularemia using tobacco mosaic virus (TMV) based delivery system. *PLoS One* **2015,** *10* (6), e0130858.

180. Gasanova, T. V.; Petukhova, N. V.; Ivanov, P. A., Chimeric particles of tobacco mosaic virus as a platform for the development of next-generation nanovaccines. *Nanotechnol. Russ.* **2016,** *11* (3), 227-236.

181. Masarapu, H.; Patel, B. K.; Chariou, P. L.; Hu, H.; Gulati, N. M.; Carpenter, B. L.; Ghiladi, R. A.; Shukla, S.; Steinmetz, N. F., Physalis mottle virus-like particles as nanocarriers for imaging reagents and drugs. *Biomacromolecules* **2017,** *18* (12), 4141-4153.

182. Dharmarwardana, M.; Martins, A. F.; Chen, Z.; Palacios, P.; Nowak, C. M.; Welch, R. P.; Li, S.; Luzuriaga, M. A.; Bleris, L.; Pierce, B. S.; Sherry, A. D.; Gassensmith, J. J., Nitroxyl Modified Tobacco Mosaic Virus as a Metal-Free High-Relaxivity MRI and EPR Active Superoxide Sensor. *Mol. Pharm.* **2018,** *15*, 2973–2983.

183. Bäcker, M.; Koch, C.; Eiben, S.; Geiger, F.; Eber, F.; Gliemann, H.; Poghossian, A.; Wege, C.; Schöning, M. J., Tobacco mosaic virus as enzyme nanocarrier for electrochemical biosensors. *Sens. Actuators, B* **2017,** *238*, 716-722.

184. Anderson, C. E.; Donnola, S. B.; Jiang, Y.; Batesole, J.; Darrah, R.; Drumm, M. L.; Brady-Kalnay, S. M.; Steinmetz, N. F.; Yu, X.; Griswold, M. A.; Flask, C. A., Dual Contrast-Magnetic Resonance Fingerprinting (DC-MRF): A Platform for Simultaneous Quantification of Multiple MRI Contrast Agents. *Sci. Rep.* **2017,** *7* (1), 8431.

185. Pitek, A. S.; Wang, Y.; Gulati, S.; Gao, H.; Stewart, P. L.; Simon, D. I.; Steinmetz, N. F., Elongated Plant Virus-Based Nanoparticles for Enhanced Delivery of Thrombolytic Therapies. *Mol. Pharm.* **2017,** *14* (11), 3815-3823.

186. Finbloom, J. A.; Han, K.; Aanei, I. L.; Hartman, E. C.; Finley, D. T.; Dedeo, M. T.; Fishman, M.; Downing, K. H.; Francis, M. B., Stable disk assemblies of a tobacco mosaic virus mutant as nanoscale scaffolds for applications in drug delivery. *Bioconjugate Chem.* **2016,** *27* (10), 2480-2485.

187. Cossé, A.; König, C.; Lamprecht, A.; Wagner, K. G., Hot Melt Extrusion for Sustained Protein Release: Matrix Erosion and In Vitro Release of PLGA-Based Implants. *AAPS PharmSciTech* **2017,** *18* (1), 15-26.

188. Ren, Y.; Shi, X.; Sun, Q.; Sun, L., Dual-controlled oral colon-targeted delivery of bovine insulin based on mesoporous phosphonate. *Mater. Res. Bull.* **2013,** *48* (11), 4850-4855.

189. Majewski, M.; Noh, H.; Islamoglu, T.; Farha, O. K., NanoMOFs: little crystallites for substantial applications. *J. Mater. Chem. A* **2018,** *6* (17), 7338-7350.

190. Chen, T.-T.; Yi, J.-T.; Zhao, Y.-Y.; Chu, X., Biomineralized Metal-Organic Framework Nanoparticles Enable Intracellular Delivery and Endo-Lysosomal Release of Native Active Proteins. *J. Am. Chem. Soc.* **2018,** *140*, 9912–9920.

191. Jha, S. K.; Marqusee, S., Kinetic evidence for a two-stage mechanism of protein denaturation by guanidinium chloride. *Proc. Natl. Acad. Sci. U. S. A.* **2014,** *111* (13), 4856-4861.

192. Zhang, H.; Chen, W.; Gong, K.; Chen, J., Nanoscale Zeolitic Imidazolate Framework-8 as Efficient Vehicles for Enhanced Delivery of CpG Oligodeoxynucleotides. *ACS Appl. Mater. Interfaces* **2017,** *9* (37), 31519-31525.

193. Schade, D. S., THE TIMING OF MEAL INSULIN ADMINISTRATION. *Endocr. Pract.* **2017,** *23* (12), 1482-1484.

194. Tadepalli, S.; Yim, J.; Cao, S.; Wang, Z.; Naik, R. R.; Singamaneni, S., Metal–Organic Framework Encapsulation for the Preservation and Photothermal Enhancement of Enzyme Activity. *Small* **2018,** *14* (7), 1702382.

195. Luzuriaga, M. A.; Welch, R. P.; Dharmarwardana, M.; Benjamin, C. E.; Li, S.; Shahrivarkevishahi, A.; Popal, S.; Tuong, L. H.; Creswell, C. T.; Gassensmith, J. J., Enhanced Stability and Controlled Delivery of MOF-Encapsulated Vaccines and Their Immunogenic Response In Vivo. *ACS Appl. Mater. Interfaces* **2019,** *11* (10), 9740-9746.

196. Liang, W.; Ricco, R.; Maddigan, N. K.; Dickinson, R. P.; Xu, H.; Li, Q.; Sumby, C. J.; Bell, S. G.; Falcaro, P.; Doonan, C. J., Control of Structure Topology and Spatial Distribution of Biomacromolecules in Protein@ZIF-8 Biocomposites. *Chem. Mater.* **2018,** *30* (3), 1069-1077.

197. Wang, C.; Sudlow, G.; Wang, Z.; Cao, S.; Jiang, Q.; Neiner, A.; Morrissey, J. J.; Kharasch, E. D.; Achilefu, S.; Singamaneni, S., Metal-Organic Framework Encapsulation Preserves the Bioactivity of Protein Therapeutics. *Adv. Healthcare Mater.* **2018,** *7* (22), 1800950.

198. Liang, W.; Xu, H.; Carraro, F.; Maddigan, N. K.; Li, Q.; Bell, S. G.; Huang, D. M.; Tarzia, A.; Solomon, M. B.; Amenitsch, H.; Vaccari, L.; Sumby, C. J.; Falcaro, P.; Doonan, C. J., Enhanced Activity of Enzymes Encapsulated in Hydrophilic Metal–Organic Frameworks. *J. Am. Chem. Soc.* **2019,** *141* (6), 2348-2355.

199. Pu, S.; Zhang, X.; Yang, C.; Naseer, S.; Zhang, X.; Ouyang, J.; Li, D.; Yang, J., The effects of NaCl on enzyme encapsulation by zeolitic imidazolate frameworks-8. *Enzyme Microb. Technol.* **2019,** *122*, 1-6.

200. Song, J.; He, W.; Shen, H.; Zhou, Z.; Li, M.; Su, P.; Yang, Y., Construction of multiple enzyme metal–organic frameworks biocatalyst via DNA scaffold: A promising strategy for enzyme encapsulation. *Chem. Eng. J. (Lausanne)* **2019,** *363*, 174-182.

201. Otero, T. F.; Sansieña, J. M., Soft and Wet Conducting Polymers for Artificial Muscles. *Adv. Mater.* **1998,** *10* (6), 491-494.

202. Okuzaki, H.; Osada, Y., Electro-driven chemomechanical polymer gel as an intelligent soft material. *J. Biomater. Sci., Polym. Ed.* **1994,** *5* (5), 485-496.

203. Peterson, G. I.; Dobrynin, A. V.; Becker, M. L., Biodegradable Shape Memory Polymers in Medicine. *Adv. Healthcare Mater.* **2017,** *6* (21), 1700694.

204. Ge, F.; Zhao, Y., A new function for thermal phase transition-based polymer actuators: autonomous motion on a surface of constant temperature. *Chem. Sci.* **2017,** *8* (9), 6307-6312.

205. Zhao, Q.; Zou, W.; Luo, Y.; Xie, T., Shape memory polymer network with thermally distinct elasticity and plasticity. *Sci. Adv.* **2016,** *2* (1), e1501297.

206. Wang, J.; Zhao, Q.; Cui, H.; Wang, Y.; Chen, H.; Du, X., Tunable shape memory polymer mold for multiple microarray replications. *J. Mater. Chem. A* **2018,** *6* (48), 24748-24755.

207. Zhao, Q.; Wang, Y.; Cui, H.; Du, X., Bio-inspired sensing and actuating materials. *J. Mater. Chem. C* **2019**.

208. Panda, M. K.; Runčevski, T.; Chandra Sahoo, S.; Belik, A. A.; Nath, N. K.; Dinnebier, R. E.; Naumov, P., Colossal positive and negative thermal expansion and thermosalient effect in a pentamorphic organometallic martensite. *Nat. Commun.* **2014,** *5*, 4811.

209. Panda, M. K.; Centore, R.; Causà, M.; Tuzi, A.; Borbone, F.; Naumov, P., Strong and Anomalous Thermal Expansion Precedes the Thermosalient Effect in Dynamic Molecular Crystals. *Sci. Rep.* **2016,** *6*, 29610.

210. Dharmarwardana, M.; Arimilli, B. S.; Luzuriaga, M. A.; Kwon, S.; Lee, H.; Appuhamillage, G. A.; McCandless, G. T.; Smaldone, R. A.; Gassensmith, J. J., The thermo-responsive behavior in molecular crystals of naphthalene diimides and their 3D printed thermochromic composites. *CrystEngComm* **2018,** *20* (39), 6054-6060.

211. Bruckman, M. A.; Steinmetz, N. F., Chemical Modification of the Inner and Outer Surfaces of Tobacco Mosaic Virus (TMV). *Methods Mol Biol (N. J.)* **2014,** *1108*, 173-185.

212. Wang, T.; Wu, Y.; Kuan, S. L.; Dumele, O.; Lamla, M.; Ng, D. Y. W.; Arzt, M.; Thomas, J.; Mueller , J. O.; Barner-Kowollik , C.; Weil, T., A Disulfide Intercalator Toolbox for the Site-Directed Modification of Polypeptides. *Chem. – Eur. J.* **2015,** *21* (1), 228-238.

213. Gnaccarini, C.; Ben-Tahar, W.; Mulani, A.; Roy, I.; Lubell, W. D.; Pelletier, J. N.; Keillor, J. W., Site-specific protein propargylation using tissue transglutaminase. *Org. Biomol. Chem.* **2012,** *10* (27), 5258-5265.

214. Park, J. W.; Kim, Y.; Lee, K.-J.; Kim, D. J., Novel Cyanine Dyes with Vinylsulfone Group for Labeling Biomolecules. *Bioconjugate Chem.* **2012,** *23* (3), 350-362.

215. Kurganov, B. I.; Rafikova, E. R.; Dobrov, E. N., Kinetics of Thermal Aggregation of Tobacco Mosaic Virus Coat Protein. *Biochemistry (Moscow)* **2002,** *67* (5), 525-533.

216. Fomine, S.; Fomina, L.; Arreola, R.; Alonso, J., Bisimide-lactamimide ring contraction in six-membered polyimides. *Polymer* **1999,** *40* (8), 2051-2058.

BIOGRAPHICAL SKETCH

Raymond Patrick Welch was born in 1985 at Wright-Patterson Air Force Base in Fairborn, Ohio. He moved to Aledo, Texas in 1988, and to Weatherford, Texas in 1998. After graduating from Weatherford High School in 2003, Raymond enrolled at The University of Texas at Dallas in Richardson, Texas for a year. In 2006, he transferred to The University of North Texas in Denton, Texas and in December 2013 received a Bachelor of Science with a major in Electrical Engineering and a Bachelor of Science with a major in Chemistry and a minor in Mathematics. In August 2014, he entered the Chemistry graduate program at The University of Texas at Dallas.

CURRICULUM VITAE

Raymond P. Welch

Education

Doctor of Philosophy in Chemistry (May 2019)
University of Texas at Dallas, Richardson, TX, USA
"Controlling Thermal Effects on Chemical Systems"
Advisor: Professor Jeremiah. J. Gassensmith

Bachelor of Science in Chemistry (2013)
Bachelor of Science in Electrical Engineering (2013)
Minor in Mathematics
University of North Texas, Denton, TX, USA

Research Experience

University of Texas at Dallas, Aug 2014 – May 2019
Department of Chemistry and Biochemistry;
Research Advisor: Dr. Jeremiah. J. Gassensmith
Synthesis of small molecules; small molecule bioconjugation to virus-like particles (VLPs) and proteins; VLP isolation and purification from plant material; biomaterials preparation and analysis; metal-organic framework synthesis on biomaterials, biomaterials and protein antigen surface analysis; *extensive* electron microscopy (TEM and SEM) characterization and analysis of VLP-based materials; Lab Safety Officer and Safety Liaison; Inventory and Waste Manager

University of Texas at Dallas, Jun 2014 – Aug 2014
Department of Chemistry and Biochemistry; Research Supervisor: Dr. Yves J. Chabal
Silicon surface cleaning, etching, and functionalization; quantum dot synthesis

University of North Texas, May 2012 – December 2013
Department of Chemistry, Denton, TX, USA; Research Advisor: Dr. Jeffry A. Kelber
Deposition of boron carbide thin films; plasma etching and deposition; building and maintenance of ultra-high vacuum chambers; magnetron sputtering

Teaching Experience

Teaching Assistant for CHEM 4473 Advanced Physical Measurements
Dr. Warren Goux, Dr. Yu Huang
January 2019 – May 2019, University of Texas at Dallas

Teaching Assistant for CHEM 3471 Advanced Synthesis
Dr. Jeremiah Gassensmith, Dr. John Ferraris, Dr. Ronald Smaldone
June 2017 – May 2018, University of Texas at Dallas

Teaching Assistant for CHEM 1111 General Chemistry Laboratory I, Safety TA
Dr. Sandhya Gavva, Dr. Yanping Qin, Dr. Amandeep Sra
June 2016 – May 2017, University of Texas at Dallas

Teaching Assistant for CHEM 1312 General Chemistry II Lecture
Dr. Jason McAfee, Dr. Stephanie Taylor
January 2016 – May 2016, University of Texas at Dallas

Teaching Assistant for CHEM 1311 General Chemistry I Lecture
Dr. Jason McAfee, Dr. John Sibert
August 2015 – December 2015, University of Texas at Dallas

Teaching Assistant for CHEM 1112 General Chemistry II Laboratory
Dr. Jason McAfee, Dr. Amandeep Sra
January 2015 – July 2015, University of Texas at Dallas

Teaching Assistant for CHEM 1111 General Chemistry I Laboratory
Dr. Jason McAfee
August 2014 – December 2014, University of Texas at Dallas

Proficiencies

Chemical Methods

ELISA, Protein assays (Lowry, Bradford), Small molecule synthesis, Plant virus isolations, Bacterial protein expression and purification, MOF synthesis

Instrumentation Methods

TEM (Biological, CryoTEM, tomography, negative stain), Plunge freezing, SEM, UV-Vis spectroscopy, Circular dichroism spectroscopy, NMR spectroscopy, HPLC, ESI-MS, FT-IR spectroscopy, Fluorescence spectroscopy, XPS, DLS

Management

Team management, Lab management (Inventory, Waste, Instrument upkeep and maintenance, Scheduling), System and protocol organization

Software and Programming

Microsoft Office (Word, Excel, PowerPoint, OneNote), Adobe CS6 (Illustrator, Premiere, Photoshop), Chemdraw, Origin, TopSpin, C#, C++, VHDL, LabView, MATLAB

Other

UHV chamber construction and maintenance, Blacksmithing

Publications

ORCID: 0000-0003-3114-8801

1. **Welch, R. P.**‡; Dharmarwardana, M.‡; Caicedo-Narvaez, C.; Luzuriaga, M. A.; Arimilli, B. S.; McCandless, G. T.; Fahimi, B.; Gassensmith, J. J., Reversibly Thermosalient NDI Crystal Switch, *Manuscript in Preparation* ‡Denotes co-first authorship and equal contribution
2. Luzuriaga, M. A.‡; **Welch, R. P.**‡; Dharmarwardana, M.; Benjamin, C. E.; Li, S.; Shahrivarkevishai, A.; Popal, S; Tuong, L. H.; Creswell, C. T.; Gassensmith, J. J., Enhanced Stability and Controlled Delivery of MOF Encapsulated Vaccines and Their Immunogenic Response In Vivo. *ACS Appl. Mater. Interfaces*, **2019**, 11 (10), 9740-9746 ‡Denotes co-first authorship and equal contribution
3. **Welch, R. P.**; Lee, H.; Luzuriaga, M. A.; Brohlin, O. R.; Gassensmith, J. J., Protein-Polymer Delivery: Chemistry from the Cold Chain to the Clinic. *Bioconjugate Chem.* **2018**, 29 (9), 2867-2883.
4. Lee, H.; Benjamin, C. E.; Nowak, C. M.; Tuong, L. H.; **Welch, R. P.**; Chen, Z.; Dharmarwardana, M.; Murray, K. W.; Bleris, L.; D'Arcy, S.; Gassensmith, J. J., Regulating the Uptake of Viral Nanoparticles in Macrophage and Cancer Cells via a pH Switch. *Mol. Pharm.* **2018**, 15 (8), 2984-2990
5. Li, S.; Dharmarwardana, M.; **Welch, R. P.**; Benjamin, C. E.; Shamir, A. M.; Nielsen, S. O.; Gassensmith, J. J., Investigation of Controlled Growth of Metal–Organic Frameworks on Anisotropic Virus Particles. *ACS Appl. Mater. Interfaces* **2018**, 10 (21), 18161-18169.
6. Chen, Z.; Boyd, S. D.; Calvo, J. S.; Murray, K. W.; Mejia, G. L.; Benjamin, C. E.; **Welch, R. P.**; Winkler, D. D.; Meloni, G.; D'Arcy, S.; Gassensmith, J. J., Fluorescent Functionalization across Quaternary Structure in a Virus-like Particle. *Bioconjugate Chem.* **2017**, 28 (9), 2277-2283.
7. Dharmarwardana, M.; **Welch, R. P.**; Kwon, S.; Nguyen, V. K.; McCandless, G. T.; Omary, M. A.; Gassensmith, J. J., Thermo-mechanically responsive crystalline organic cantilever. *Chem. Commun.* **2017**, *53* (71), 9890-9893.
8. Li, S.; Dharmarwardana, M.; **Welch, R. P.**; Ren, Y.; Thompson, C. M.; Smaldone, R. A.; Gassensmith, J. J., Template-Directed Synthesis of Porous and Protective Core–Shell Bionanoparticles. *Angew. Chem., Int. Ed.* **2016**, *55* (36), 10691-10696.
9. Chen, X.; Kazi, H.; Cao, Y.; Dong, B.; Pasquale, F. L.; Colón Santana, J. A.; Cao, S.; Street, M.; **Welch, R.**; Binek, C.; Enders, A.; Kelber, J. A.; Dowben, P. A., Ultrathin chromia films grown with preferential texture on metallic, semimetallic and insulating substrates. *Mater. Chem. Phys.* **2015**, 149–150 (0), 113-123.

10. Pasquale, F. L.; James, R.; **Welch, R.**; Echeverria, E.; Dowben, P. A.; Kelber, J. A., Novel Cross-Linked Ortho-Carborane and Ortho-Carborane:Y (Y=1,4-Diaminobenzene, Pyridine, Benzene) Polymer Films: A New Class of Carborane-Based Materials with Tunable Electronic Structure. *ECS Trans.* **2013**, *53* (1), 303-310.

Presentations

1. Welch, R P.; Luzuriaga, M. A.; Li, S.; Gassensmith, J. J., Contributed talk on "Immunoassay Investigation of Vaccine Carrier Stability Within ZIF-8 Encapsulation", 256th ACS National Meeting, Boston, MA, USA. August 19, **2018**
2. Welch, R P.; Luzuriaga, M. A.; Li, S.; Gassensmith, J. J., Contributed talk on "Immunoassay Investigation of Vaccine Carrier Stability Within ZIF-8 Encapsulation", 51st Annual Meeting-in-Miniature (DFW ACS), Dallas, TX, USA. April 21, **2018**
3. Welch, R P.; Luzuriaga, M. A.; Li, S.; Gassensmith, J. J., Contributed talk on "Immunoassay Investigation of Vaccine Carrier Stability Within ZIF-8 Encapsulation", UT Dallas/Texas A&M Agrilife Research Extension Joint Symposium, Richardson, TX, USA. March 16, **2018**
4. Welch, R P.; Li, S.; Gassensmith, J. J., Contributed talk on "Template Directed Synthesis of Porous and Protective Core-Shell Bionanoparticles", Texas Soft Matter Meeting, Richardson, TX, USA. August 12, **2016**
5. Welch, R P.; Li, S.; Gassensmith, J. J., Poster presentation on "Tobacco Mosaic Virus Stabilized By Coordination Polymers", 251st ACS National Meeting, San Diego, CA, USA. March 13, **2016**
6. Welch, R P.; Li, S.; Dharmarwardana, M.; Gassensmith, J. J., Contributed talk on "Novel Synthesis of 3D Ordered Microporous Structures", Texas Soft Matter Meeting, August 21, **2015**

Professional Memberships

American Chemical Society: 2015 – Present

Awards and Honors

Nominated for the 2019 President's Award for Teaching Excellence for Teaching Assistants